AERODYNAMIC MODELS FOR INSECT FLIGHT

A thesis submitted to The University of Manchester for the degree of Doctor of Philosophy in the Faculty of Engineering and Physical Sciences

2016

Mohd Faisal Abdul Hamid

School of Mechanical, Aerospace and Civil Engineering

CONTENTS

WORD COUNT: 37,481

LIST OF FIGURES

LIST OF TABLES

ABSTRACT

Aerodynamics Models for Insect Flight

Mohd Faisal Abdul Hamid · The University of Manchester · Doctor of Philosophy · 20/05/2016

Numerical models of insect flapping flight have previously been developed and used to simulate the performance of insect flight. These models were commonly developed via Blade Element Theory, offering efficient computation, thus allowing them to be coupled with optimisation procedures for predicting optimal flight. However, the models have only been used for simulating hover flight, and often neglect the presence of the induced flow effect. Although some models account for the induced flow effect, the rapid changes of this effect on each local wing element have not been modelled. Crucially, this effect appears in both axial and radial directions, which influences the direction and magnitude of the incoming air, and hence the resulting aerodynamic forces.

This thesis describes the development of flapping wing models aimed at advancing theoretical tools for simulating the optimum performance of insect flight. Two models are presented: single and tandem wing configurations for hawk moth and dragonfly, respectively. These models are designed by integrating a numerical design procedure to account for the induced flow effects. This approach facilitates the determination of the instantaneous relative velocity at any given spanwise location on the wing, following the changes of the axial and radial induced flow effects on the wing. For the dragonfly, both wings are coupled to account for the interaction of the flow, particularly the fact that the hindwing operates in the slipstream of the forewing.

A heuristic optimisation procedure (particle swarming) is used to optimise the stroke or the wing kinematics at all flight conditions (hover, level, and accelerating flight). The cost function is the propulsive efficiency coupled with constraints for flight stability. The vector of the kinematic variables consists of up to 28 independent parameters (14 per wing for a dragonfly), each with a constrained range derived from the maximum available power, the flight muscle ratio, and the kinematics of real insects; this will prevent physically-unrealistic solutions of the wing motion.

The model developed in this thesis accounts for the induced flow, and eliminates the dependency on the empirical translation lift coefficient. Validations are shown with numerical simulations for the hover case, and with experimental results for the forward flight case. From the results obtained, the effect of the induced velocity is found to be greatest in the middle of the stroke. The use of an optimisation process is shown to greatly improve the flapping kinematics, resulting in low power consumption in all flight conditions. In addition, a study on dragonfly flight has shown that the maximum acceleration is dependent on the size of the flight muscle.

DECLARATION

No portion of the work referred to in the thesis has been submitted in support of an application for another degree or qualification of this or any other university or other institute of learning.

COPYRIGHT STATEMENT

ACKNOWLEDGEMENTS

I would like to express my sincere gratitude to Dr. Antonio Filippone, my teacher and dissertation advisor, for his patience, encouragement and support throughout the research period. His delightful personality and detailed knowledge of this research topic has guided me until the very end - I would not be here without all that he has done.

I would also like to thank Prof. Hector Iacovides and Dr. Alistair Revell - members of my thesis committee - for their thorough review of the thesis and for their valuable comments. I am especially appreciative to Dr. Ben Parslew, Dr. Nicholas Bojdo, Dr. Mostafa Ramadan, and Dr. Richard Hughes for their valuable input in the numerical modelling and aerodynamics of insect flight. Also, to my close friends in the George Begg, Pariser, and Sackville buildings; Dr. Rashdan, Dr. Azam, Hazrul Jalil, Shahrul Azmi, Firdaus Hassan, Shahrizal Sobri, Afifi, Dr. Mahmud, Dr. Imran, Dr. Iskandar, Dr. Hafiz, Imad, Sharlini, Mengying, Izzati, William Harley, Juan Manuel, and others.

I would also like to thank the medical staff of the Christie Hospital for providing good care on each visit, and especially, to Dr. Omar Aziz (consultant colorectal and laparoscopic surgeon), who has examined and monitored my health conditions.

In the abyss of my heart, to those who are very helpful and supportive in any way, form or shape but shall not be named here; you all are true gems, which I will always remember, cherish and treasure for years and years to come. Without any of you, my work will not be as good as it is now - for that thank you very much.

Finally, I would like to thank my parents for their continued support throughout my education at The University of Manchester. I would also like to acknowledge the warm support and care of my dear wife, Nazia, and my kids Daniel, Marissa, Haikal and Luqman; without their encouragement and enthusiasm, this work could not have been completed.

This work was made possible by the Ministry of Higher Education Malaysia and the University Putra Malaysia, who paid the tuition fees and all related allowances from the beginning to the end of my studies.

THESIS PUBLICATIONS

The paper published for journal publication by the time of the thesis submission:

- Faisal, A. H. M. & Filippone, A. Aerodynamic model for insect flapping wings with induced flow effect. Journal of Aircraft, Vol. 53, No. 3, 2016, pp. 701-712. doi:10.2514/1.C033382

The paper accepted for journal publication by the time of the thesis submission:

- Faisal, A. H. M. & Filippone, A. Aerodynamic model for tandem flapping wings. AIAA Journal, accepted for publication on 12 May 2016.

NOMENCLATURE

List of Abbreviations

MAVs	Micro Air Vehicles
NAVs	Nano Air Vehicles
DFM	Direct Flight Muscle
iDFM	Indirect Flight Muscle
PIV	Particle Image Velocimetry
DPIV	Digital Particle Image Velocimetry
LE	Leading Edge
TE	Trailing Edge
fps	Frames Per Second
PIV	Particle Image Velocimetry
CFD	Computational Fluid Dynamic
BEM	Blade Element Method
BEMT	Blade Element Momentum Theory
TV	Tip Vortex
TEV	Trailing Edge Vortex
LEV	Leading Edge Vortex
T/W	Thrust To Weight Ratio
P/W	Power To Weight Ratio
PSO	Particle Swarm Optimization

List of Symbols

a	Axial induction factor
a'	Radial induction factor
a_u	Wing relative acceleration, y-axis
a_v	Wing relative acceleration, z-axis
AR	Wing aspect ratio
b_t	Wing thickness
$c(r)$	Wing chord length
$c(\hat{r})$	Normalised wing chord length
$\bar{c}$	Wing mean chord length
C_D	Wing drag coefficient
$C_D(0)$	Drag coefficient at 0 degrees angle of attack
$C_D(\pi/2)$	Drag coefficient at 90 degrees angle of attack
C_L	Wing lift coefficient
C_r	Wing rotational lift coefficient
C_t	Wing translational lift coefficient
C_y	Horizontal force coefficient

C_z	Vertical force coefficient
C_η	Rate of the wing rotation
d	Particle dimension
dr	Wing section
dt	Time step
D	Aerodynamic drag force
f	Frequency (motion frequency)
$\boldsymbol{F}$	Total force
$\boldsymbol{F}_{AM}$	Force due to added mass
$\boldsymbol{F}_{C}$	Force due to circulation
$\boldsymbol{F}_{iner}$	Force due to inertial forces
$\boldsymbol{F}_{Vis}$	Force due to viscous dissipation
F_m	Momentum loss factor
F_x	Force vector component on the wing, x-axis
F_y	Force vector component on the wing, y-axis
F_z	Force vector component on the wing, z-axis
g	Acceleration of gravity
I_a	Wing inertia added-mass term
j	Particle index
k	Reduced frequency
K	Rate of the wing reverse direction
L	Aerodynamic lift force
m_{insect}	Insect mass
m_{wing}	Insect wing mass
m_{11}	Added mass term
m_{22}	Added mass term
M_{ADV}	Wing moment due to added mass and viscosity
$M_{\langle\eta,\phi,\theta\rangle}$	Wing moment
N	Multiplier period in the vertical plane
N_{wing}	Number of wing
p_j	Best position found so far by particle j
p_{wing}	Wing position
P_{aero}	Power due to aerodynamic forces
P_{iner}	Power due to inertial forces
P	Total power, $P_{aero} + P_{iner}$
q	Index of j's best neighbour
r	Distance measured from wing root to wing tip
$\hat{r}$	Normalised wing span
R	Wing span
$R_{\langle\beta,\eta,\phi,\theta\rangle}$	Rotation matrix

S	Wing area
St	Strouhal number, $2f\bar{c}h_0/V$
t	Time
T	Thrust force
u	Wing relative velocity, y-axis
U	Uniform random number generator
U_{ref}	Reference velocity
v	Wing relative velocity, z-axis
v_j	Particle velocity
v_y	Wing motion velocity, y-axis
v_z	Wing motion velocity, z-axis
$V\ or\ V_\infty$	Flight speed or free-stream velocity
w_{rel}	Wing relative velocity, m/s
W	Total insect weight, $m_{insect}g$
x_j	Particle position
α	Angle of attack
α_m	Mean angle of attack
α_{pso}	Inertia weight or constriction coefficient
β	Stroke plane angle
β_{pso}	Acceleration constant
γ	Body inclination angle
Γ_T	Translational circulation
Γ_R	Rotational circulation
ϕ	Weaving angle
θ	Flapping angle
η	Pitching angle
μ	Non-dimensional viscous torque (0.2)
ν	Fluid kinematic viscosity
ρ	Fluid density
σ	Local solidity
τ	Torque
ϕ_m, θ_m, η_m	Amplitude
ϕ_0, θ_0, η_0	Phase difference
$\Phi_{\langle\Phi,\theta,\eta\rangle}$	Offset angle
ψ	Local inflow angle
ψ_{pso}	Random positive numbers
ψ_t	Local inflow angle at the tip
ω	Angular frequency, $2\pi f$
$\Omega_{\langle\Phi,\theta,\eta\rangle}$	Wing angular velocity

List of Subscripts

i, j	Variable number
e, η, θ, ϕ	Wing reference frame
f	Forewing
h	Hindwing

CHAPTER 1. INTRODUCTION

This chapter defines scope, aim, objectives and outline of this thesis.

For millions of years, natural flyers have evolved to use flapping-wing systems for propulsion and survivability; due to their prodigious existence, they have attracted a lot of interest from researchers due to their unique flight physics. Many enquiries have been made to explore the potential for utilising flapping wing systems in certain key applications, especially for the development of the next generation of small autonomous aerial vehicles[1–5].

In the early years of the development of small flying vehicle platforms, it has been shown that conventional aerodynamic machines (fixed- and rotary wing) have denominated their design[6,7]. Following the study by Ellington[8], it has been reported that the energy required to achieve hover with flapping wings scales favourably with the size and mass of the vehicle; at this scale, it was estimated that the lift force could be increased by up to three times compared with conventional aerodynamics.

Unlike conventional aerodynamic machines which mainly rely on airflow over the wings, flapping offers greater control over the rapid changes in the forces generated by the wing, which is useful for manoeuvring[9]. Also, the flapping wing may offer a much less noisy environment when compared to the rotary wing flight, with broadband noise rather than tonal noise[10]. Additionally, according to Ref.[11–13], the flight performance can be enhanced by optimising the kinematics of the wing.

Aerodynamic models for flapping wings are somewhat limited by the computational times required. Since the flapping wing can be regarded as a moving boundary problem, the body-fitted or unstructured-grid methods are commonly employed; however, these are mostly complicated and computationally expensive[14].

The scope of the work presented in this thesis requires models that offer a compromise between physics and rapidity of calculation; the ultimate goal is to explore a multi-dimensional search space to optimise the wing kinematic parameters for optimum flight performance. A numerical optimisation procedure[15] is included to estimate the optimum kinematic parameters of the wing.

A critical aerodynamic aspect of flapping-wing flight is the self-induced flow created by rapidly-developing wakes; on the wing, these effects appear in both axial and radial directions. A reasonable hypothesis is that the induced flow may influence the direction and magnitude of the incoming air, and hence the resulting aerodynamic forces. Here, this hypothesis is examined along with the wider perspective of developing aerodynamic models that can be used for the analysis of the performance of insect flight.

In order to take account of the induced flow effect, the design procedure of Adkins & Liebeck[16] is adapted and extended by modifying some of the numerical design steps. This design procedure was designed to analyse the performance of arbitrary propellers, which eliminates the small angle approximation and some of the light loading approximations prevalent in classical design theory. The starting point of the present model is based on that published by Berman & Wang[17]. The lift and drag forces are determined following the extended lifting line theory, as adapted by Taha *et al.*[18] and Wang *et al.*[19], respectively. Two aerodynamic models of a flapping wing are developed, which attempt to represent insects such as the hawk moth and dragonfly, with single and tandem wing configurations, respectively.

1.1 SCOPE

The scope of this research work will be limited to modelling of flapping wing insect flight for predicting the optimum performance, given the types of wing configurations, flight characteristics, availability of power, and physical constraints of the wing kinematics. Two configurations are considered - single and tandem - based on hawk moth and dragonfly wing arrangements, respectively.

1.2 AIM

The aim of this research is to advance theoretical tools that widen the perspective of nature-inspired flight research methods; flapping wing insect models with two different wing configurations suitable for several types of flight mode (e.g. hover, forward, and accelerating flight).

1.3 OBJECTIVES & THESIS OUTLINE

The thesis work presented deals with the modelling of flapping wing flight that could offer a low-order model, in the sense of accommodating the complexity of the wing kinematics, flow physics and flight characteristics of an insect. A BEMT method is adopted to execute the preliminary work of developing a new aerodynamic model. The review of various topics related to the insect flapping flight is described in Chapter 2. Chapter 3 presents the methods for developing the aerodynamic model of the insects. Chapter 4 discusses the results of the study, while concluding remarks are presented in Chapter 5. The specific objectives are listed below:

1. To give an overview of the field of small air vehicle design (Chapter 2)
2. To present matters concerning the proposed scheme for constructing a predictive simulation tool (Chapter 2)
3. To provide a comprehensive review of the existing aerodynamic methods (Chapter 2)
4. To discuss factors influencing the performance of insect flight (Chapter 2)
5. To formulate an extensible aerodynamic method for predicting the optimum flight envelope or performance of a flapping wing (Chapter 3)
6. To verify that the method is robust by demonstrating its numerical accuracy, stability and convergence (Chapter 3)
7. To validate simulated kinematics against established data from literature (Chapter 3)
8. To compare the results with other aerodynamic models of insect flight (Chapter 4)
9. To evaluate the influence of induced flow effects on the flight performance (Chapter 4)
10. To analyse the flight performances of different wing shapes on different wing configurations (Chapter 4)
11. To predict the optimum performance of an insect in flight (Chapter 4)
12. To conclude the implications of the research outcomes to the fields of insect flapping flight (Chapter 5)

CHAPTER 2. LITERATURE REVIEW

This chapter provides a comprehensive review of various topics related to the insect flapping flight. The aim is to provide a meticulous assessment of the existing aerodynamic models, and to ascertain spaces in which advancement is required. This chapter is comprised of eight sections covering various aspects pertaining to the development of the modelling of insect flight. The first section provides an overview of the involvement, classification, application, and challenges of small air vehicle design. The second section gives a brief review of the main body parts of an insect responsible for flying, and their respective functions. The third section discusses some of the aerodynamic modelling techniques and setups that exist in the study of insect flight. The fourth section provides a detailed review of existing blade element aerodynamic models of insect flapping flight. The fifth section highlights the mathematical optimisation studies of flapping insect aerodynamic models. The sixth section discusses some factors, which influence the aerodynamic performance of insect flight. The seventh section includes some prediction of the induced flow effect via blade element momentum theory. Section eight describes the characterisation, quantification, and derivation associated with the aerodynamic coefficients of insect flapping flight.

2.1 OVERVIEW OF SMALL AIR VEHICLE

In the last decade, many research institutions have been active in the field of developing small air vehicles; i.e. Micro Air Vehicles (MAVs) and Nano Air Vehicles (NAVs). These institutions include the Harvard Micro-robotics Laboratory in the USA[4]; the Department of Aeromechanics and Flying Engineering from Central AeroHydrodynamical Institute (TsAGI), and Moscow Institute of Physics and Technology (MIPT) in Russia[20]; the Aircraft Aerodynamics and Design Group at Stanford University (USA)[21]; the Swiss Federal Institute of Technology (EPFL)[22]; the Kasetsart University in Thailand[23]; the University of Toulouse in France[23]; the Cranfield University in UK[24]; the University Putra in Malaysia[25]; the Delft University of Technology in The Netherlands[26]; and the Seoul National University in Korea[27]. Some companies and agencies have also been involved, such as DARPA from the USA[28]; Advanced Subsonics Inc. in Canada[29]; Air Force Research Laboratory Wright-Patterson in the USA[30]; and many others. Their research covers various scopes, commonly including the system size optimisation along with weight reduction, flight performance, and function enhancement as well as the robustness of the flight control systems.

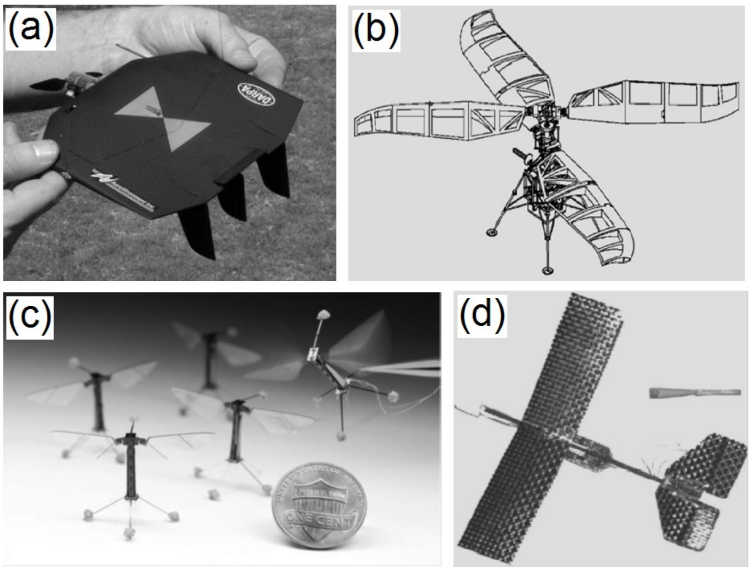

Figure 2-1 Classification of MAVs/NAVs; (a) Fixed wing (Black Widow MAV, image taken from Ref.[31]), (b) Rotary wing (MARV, image taken from Ref.[32]), (c) Flapping wing (RoboBees, image taken from Ref.[4]), (d) Passive wing (Palm-size micro glider, image taken from Ref.[33]).

The MAVs/NAVs can be classified into four main types, depending on their method of propulsion and lift[34]. As shown in Figure 2-1, these are fixed wings[21,31,35–37], rotary wings[23,32,38], flapping wings[4,7,29,39–44], and a fourth class of passive wings (e.g. airship, glider)[33,45]. The Micro and Nano Air Vehicles (MAVs and NAVs) are defined in Table 2-1, based on the data and definitions from Ref.[12,34,46–48].

Table 2-1 Definitions of the MAVs and NAVs; input from Ref.[12,34,46–48].

Description	**NAV**	**MAV**
Flying Duration	10 min	30 min
Maximum Dimension	10 cm	15 cm
Operating Range	1 km	10 km
Typical Flight Speeds	5 m/s	10 m/s
Maximum Take-Off Weight (MTOW)	20 g	100 g

The forecast applications for small-sized air vehicles span a wide range, from delivering sensors, transmitting information, sensing pollution, performing measurements, and reconnaissance missions in areas otherwise inaccessible, thus offering potential for widening and revolutionising sensing and information gathering capabilities[49]. With their special advantages in small size, high agility and manoeuvrability, performing indoor or outdoor missions (or both) in very hazardous environments (toxic) or dangerous spaces (burning and collapsing structures) could be extremely strategic.

Figure 2-2 Aerial UAV footage shows 200-year-old pub destroyed as River Irwell floods in December 2015 (image taken from Ref.[50]).

Moreover, these systems (e.g. bio-inspired flapping wing robots developed at University of Illinois[51]) could provide an instantaneous rapid overview in the area around the personnel, thus reducing the possibility of injury and fatality during rescue missions[52–54]. In addition, since

NAVs can be deployed in a few seconds, they are the best choice to be used in disaster cases (as shown in Figure 2-2) by decreasing the time necessary to explore a given area[55]; in particular those areas affected by earthquakes, hurricanes, or in collapsed mines or buildings[35].

Over the years, the complexity and challenges of MAV/NAV designs has increased, due to the fact that the MAVs/NAVs designed were often focused on reducing the size while maintaining similar capabilities as larger aircraft[56]. This presents problems, for instance when dealing with the complex airframe design in maintaining a high intensity to structural weight ratio. This includes the energy storage capacity to fulfil a long mission requirement, control needs and sizing corresponding to the aerodynamic requirements, and communications systems for increasing the data processing, transmitting and receiving capabilities[36,37,57–61].

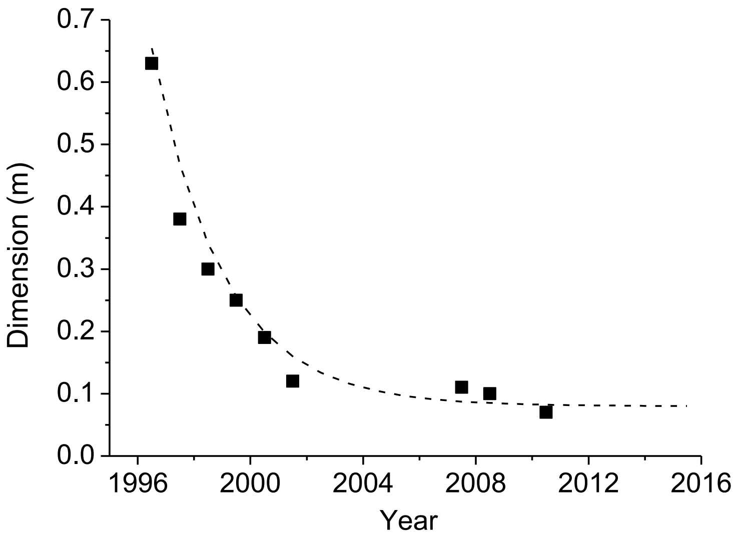

Figure 2-3 The miniaturisation progress of small air vehicles (adapted from Ref.[34]).

In spite of various technology forecasts in the literature, the field struggles to make advances, because of the poorly-understood physics related to the challenges of manoeuvrability at low speed[49]. The physical and technological challenges in the last few years have slowed down any further miniaturisation of small air vehicles[62] (See Figure 2-3).

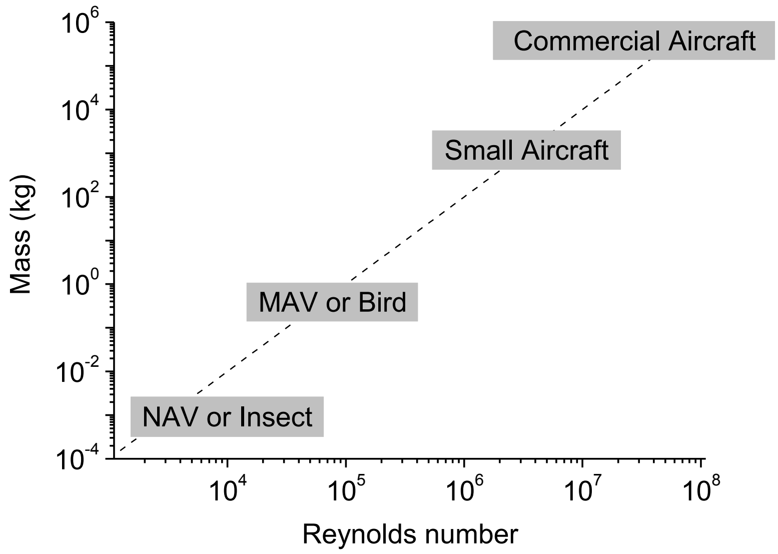

Figure 2-4 Reynolds number range for man-made flying vehicles and natural flyers (the Reynolds number are based on the flight speeds; adapted from Ref.[63]).

With a lower speed and smaller size than conventional aircraft, the Reynolds number[I] for NAVs commonly lies in the region of less than one-hundred thousand, which is less than one-tenth of that of a full-sized commercial aircraft (Figure 2-4). This, therefore, affects the flight domain, since the aerodynamic efficiency rapidly decreases[63,65] , and also opens up a new segment in aerodynamic-related problems, ranging from the determination of aerodynamic forces with complex wing flapping, kinematic motions, and the aerodynamics at low Reynolds numbers of compliant surfaces[66,67].

[I] The Reynolds number (for flapping insect flight) is defined as $Re = U_{ref}\bar{c}/\nu$ following Shyy *et al.*[64]; the reference velocity U_{ref} is based on the mean wingtip velocity ωR and forward velocity V for hover and forward flight, respectively.

2.2 ANATOMY OF FLYING INSECTS

This section is intended to give a brief review of the main body parts of an insect that are responsible for flying, and their respective functions. The following roles within this subdivision will provide some brief information, particularly on the muscles and wings that are responsible for their flight.

2.2.1 Flying Insect Flight Muscles

For insects, the driving mechanism in propelling the wing beating movements can be envisaged as a box (later called the thoracic box). The sides of the thoracic box are called the pleura and the base of the sternum. The wings are attached to the pleura by flexible membranes, providing a form of elastic energy storage inside the thoracic box. There are two kinds of insect flight muscle arrangement inside the thoracic box powering the kinematic motion of the wing during flight, known as direct flight muscle (DFM) and indirect flight muscle (iDFM). The direct flight muscles are directly linked to the wing root, whereas the indirect flight muscles are connected to the thorax and the muscle action deforms the thoracic box to give wing movement via the wing root.

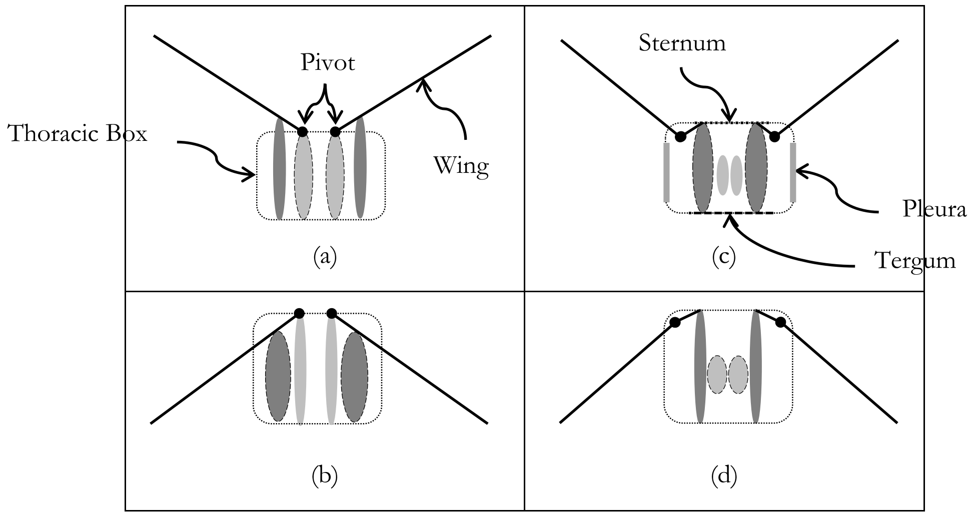

Figure 2-5 Direct ((a), (b)) and indirect ((c), (d)) flight mechanisms. Thorax during upstroke ((a), (c)) and downstroke ((b), (d)) of the wings (a pair of oval shapes with a dotted line inside the thoracic box represent the current contraction of the flight muscles). Adapted from [68].

Insects with a kind of DFM are categorised as primitive insects, such as dragonflies and cockroaches. During the flight of DFM insects, the wing upstroke kinematic motion is brought about by the contraction of the DFM, which is attached to the wing base inside the pivotal point at the wing muscle joint. The downstroke kinematic motion is induced through the contraction of the wing DFM that extends from the sternum to the wing base (tergum) outside the pivotal point; however for the iDFM insect, the flight muscles are attached to the tergum and sternum. During the upstroke of the iDFM insect, the tergum is pulled down and levers the outer main part of the wing as a result of the flight muscle contraction, which causes the wing to elevate. During the downstroke, the contraction of iDFM causes the thoracic box to deform, thus lifting the tergum and forcing the wing to move downwards[69].

2.2.2 Flying Insect Wings

During flight, an insect normally makes constant adjustments through the kinematic motion of their wings, to maintain their flight trajectory or to maintain their altitude when hovering. In which, to stabilise and prolong the attachment of vortices on the leading edge of the wing, thus, helps in preventing the occurrence of flow detachment that would causes wing stall[70–72]. Typically, the functional insect wings may be a type of membrane or non-membrane (as given in Table 2-2); these are flapping-like cuticular projections supported by tubular sclerotized veins for the membranous wing, and all major veins are found to have a longitudinal arrangement measured from the wing root to the tip - they are also denser at the anterior margin. Some cross veins function as transverse struts, which join and support the longitudinal veins. For the non-membranous wing, structures may consist of rather tough forewings known as elytra (i.e. beetles), which function to protect the hindwing while not flying. For some insects which have two pairs of wings, their fore- and hindwings are coupled together by a mechanism such as a small hook known as hamuli[69].

Table 2-2 Types of membranous wing insect (data source from[73])

Description	Insect
One pair of wings	Ground-hoppers Mayflies (some families) Scale insects (males) Stylopids (males) True flies
Two pairs of wings	Thrips
Wing membrane clothed with minute scales or hairs	Butterflies and moths Caddis and white flies Web-spinners and Lacewings
Wing membrane without a noticeable clothing of hairs or scales, although veins may be hairy: usually colourless and transparent, but may be coloured	Termites Scorpion Stoneflies
Wings with many cross-veins forming a dense network	Mayflies (some families) Dragonflies and Ant-lions Alder flies
Wings with few cross-veins	Psocids, aphids, cicadas Bees, wasps, ants, ichneumons

2.3 AERODYNAMIC MODELS OF FLAPPING INSECT

For decades, extensive research in predicting the aerodynamics of flying machines has led to a wide range of modelling methods for fixed and rotary wing aircraft as well as for the flapping flying insect. These can be seen through the existence of various modelling methods such as those from experimental measurements[30–36]; numerical simulations[37–65]; and flapping insect prototype developments[4,40–42,106–109].

Nevertheless, and particularly for the present problem, finding the most appropriate methods that will work effectively within the specified scopes and limitations is a challenge; it involves finding a model that is appropriate for use as part of the preliminary design and optimisation of flapping wings. This section is intended to address the issue, and to identify the appropriate aerodynamic modelling methods for flapping insect flight models.

2.3.1 Experimental Models

In order to get a clear picture of the techniques and setup that have been used, some experimental models are reviewed. This includes flow visualization techniques such as high-speed photography, slow motion film, Particle Image Velocimetry (PIV), and kinematic motion response techniques using force transducers.

From a set of selected photographs taken from a stills camera, Norberg[110] analysed the hovering kinematic flight of the dragonfly on two types of flapping wing model in a large Lucite container (filled with water or glycerine). This was carried out to observe the production and motion of the leading edge (LE) and the separation vortex that is responsible for generating circulation during the initial phase of the so- called 'fling' process[110]. When the wing stroke plane was tilted at 60 degrees to the horizontal plane, the average forces were obtained via steady-state aerodynamic theory. The wing was then given some input to move, mimicking the kinematics of the flapping insect wing. At the same instant, photographs were taken by focussing on the wing surface markers to capture the flow field around the flapping wing. Finally, the net lift and thrust averaged over one complete cycle were determined, using the unsteady potential flow theory from the instantaneous forces generated at various stages on the full wing flapping cycles. However, using the experimental process by Maxworthy[74], it was found to be rather difficult to keep the wing motion acting independently of the body orientations. As commented by Savage *et al.*[75], the calculated lift was over-predicted, given at about four times that of the total weight of the insect.

In 1997, Van Den Berg & Ellington[77] studied the flow patterns of hovering hawk moths to identify the aerodynamic mechanisms responsible for forming vortices on the wing surface. This was analysed using a scaled-up robotic insect model, known as a flapper, which was placed in a confined space. The analysis began by sending an electrical input to the flapper causing it to flap. In order to capture the flow field around the wing, a quantity of smoke was released from a smoke rake built into the leading edge of the right wing. A video camera was used to film the disturbed flow field interacting with the flapping wing motion. The results clearly showed that the dynamic stall was mainly responsible for generating the leading-edge vortex (LEV), and not the rotational wing model mechanisms. The LEV lift due to the instability of the vortex, however, was lower than estimated[111,112].

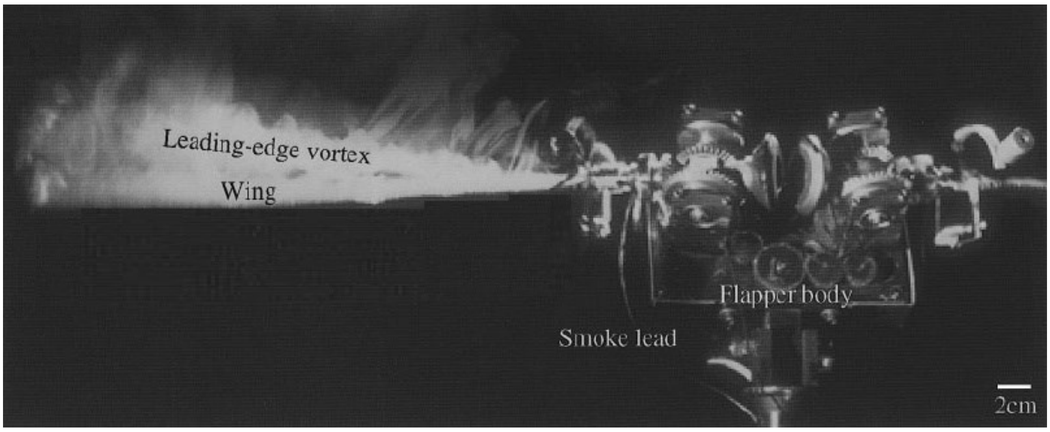

Figure 2-6 Flow visualization of the leading-edge vortex during the downstroke (image taken from Ref.[111]).

Using a high-speed camera with a sample rate of 1500 frames per second (fps) and a resolution of 512×1024 pixels, Wang & Russell[78] traced the effects of forewing and hindwing interactions on aerodynamic forces and power in the hovering flight of a tethered dragonfly. From the captured images, the deflection of the abdomen relative to the thorax was used as a cue to select the flight sequences, and three-dimensional wing motions were reconstructed by tracking three painted points on each wing. In parallel with this, a two-dimensional numerical model was developed to compute the aerodynamic force and power of the insect flight. It was found that the insect's out-of-phase motion allows it to use minimal power in maintaining hovering flight. Based on the image from the high-speed camera, however, it was difficult to acquire the momentum generated from the vortices.

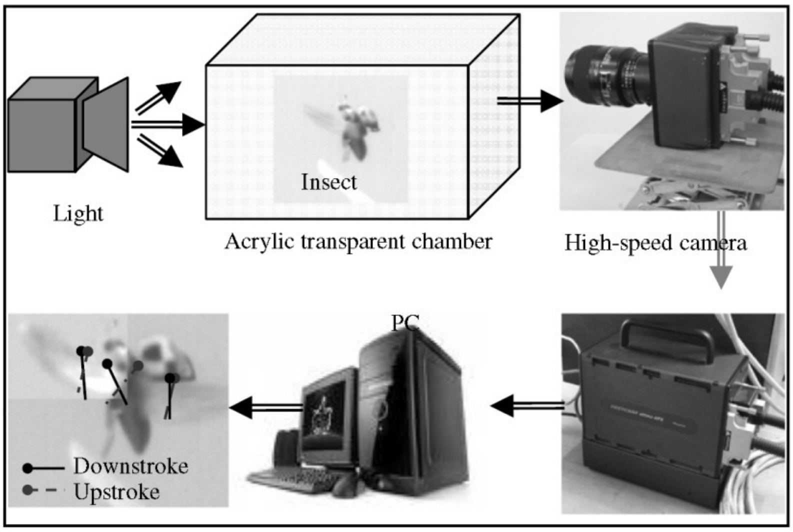

Figure 2-7 Schematic of the experimental apparatus setup for capturing the images of the Coleopteran insect wing motion (image taken from Ref.[79]).

Le *et al.*[79] investigated the aerodynamic performance of the hindwing and elytron (stiff forewing) interaction of Coleopteran insects (beetle) in hovering flight. The experiment measured the insect model kinematics using a digital high-speed camera with a sample rate of 2000 fps and a resolution of 1024×1024 pixels in an enclosed cubic chamber made of transparent acrylic. The acquired data was then used in a two-dimensional numerical simulation to compute the aerodynamic forces. From the analysis, it was found that the flexibility of the hindwing played a significant role in generating the lift forces. Although the elytron flapped along an inclined stroke producing vertical and horizontal forces, no significant contribution to aerodynamic force was observed when considering the total average forces.

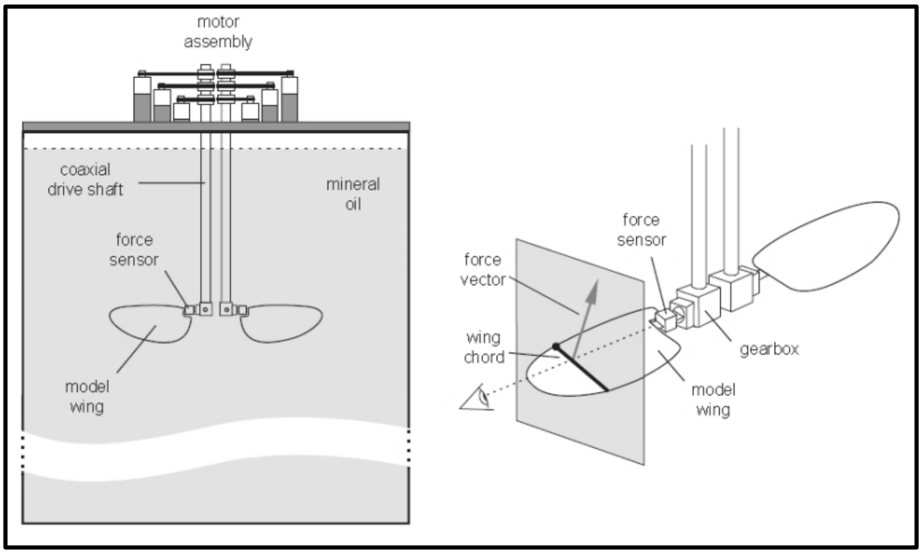

Figure 2-8 Robotic fly apparatus (image taken from Ref.[113])

As mentioned in some earlier studies[113,114], a dynamically-scaled robotic fly (with a back-and-forth wing beat pattern and no stroke plane deviation) was used to obtain the unsteady forces and flows in low-Reynolds-number hovering flight[76]. The experiment was carried out by placing the wing and arm apparatus into a Plexiglas tank filled with mineral oil, with a two-dimensional force sensor attached to measure the parallel and perpendicular forces to the wing surface. Digital Particle Image Velocimetry (DPIV) was used to measure the flow structure around the wing, by capturing images of small air bubbles created by forcing air through a ceramic water filter stone. Three different rotational cases were investigated; the advanced, symmetrical, and delayed. From the three cases, it was found that, in both the advanced and symmetrical rotational cases, the two-dimensional forces could yield good approximations of three-dimensional experiments. However, the measured two-dimensional lift force in the delayed case was found to be lower than that obtained in the three-dimensional experiments.

The aerodynamic characteristics of a flapping insect wing in hovering and forward flight - mimicking the kinematics of a bumblebee - were experimentally investigated with trapezoidal and sinusoidal types of motion, on a dynamically-scaled flapping wing mechanical model in a water tunnel[13]. The flapping (up and down) and the feathering (back and forth) motions were driven independently by two stepping motors and a controller. The forces and bending moments were measured using two sets of strain gauges and a one-dimensional force or torque transducer, respectively. It was found that the feathering rotation during the flapping translation caused an increase in aerodynamic power, rather than in lift and thrust. It was also found that in hovering or moving at a lower forward flight speed, the sinusoidal flapping motion and trapezoidal feathering motion with a shorter period of rotation generated greater lift. The overall findings on the flapping motion and the feathering motion agree well with other research[5,84,115–117]. Thus, the use of sinusoidal and trapezoidal motion demonstrated useful ways of mimicking the insect flapping wing kinematics, and could provide some relevant information for improving the overall performance when selecting the appropriate types of kinematic motion.

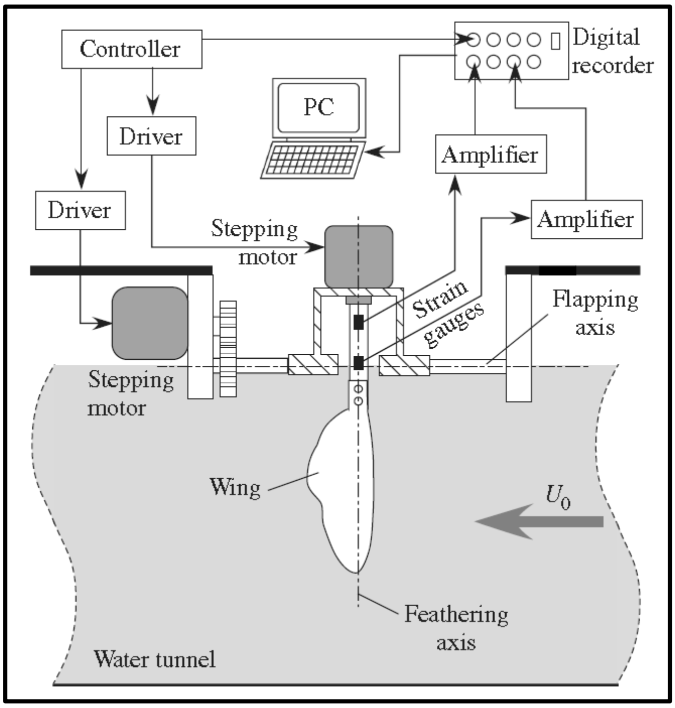

Figure 2-9 Dynamically scaled mechanical model for force measurement (image taken from Ref.[13])

In visualising and characterising the near-wake flow fields from the flapping-wing of a micro air vehicle in an open circuit wind tunnel, the PIV method was used[80]. A seeding of olive oil particles for PIV measurements was maintained in a steady flow, flowing throughout the wind tunnel test section, and illuminated through a transparent glass ceiling by a thick laser sheet generated by the PIV lasers. The result showed that a large-scale vortex ring was shed into the near-wake region during the fling motion of the side wings. However, the instantaneous flow measurements showed that, for various flapping cycles, some differences in the vortex occurred close to the wing tip, due to inaccurate predictions of the instantaneous shape changes of the flexible wings.

Mazaheri & Ebrahimi[118] have developed a mechanical flapping system which they analysed in a large low-speed wind tunnel, adopted from the design and analysis of a remotely-controlled ornithopter called Cybird P1 by Kim & Shim[119]. The intention of the analysis was to provide further insight into the aerodynamic performance of flapping wing flight vehicles, by carrying out measurements on the unsteady aerodynamic forces of the flapping wing motion. The lift and thrust of the mechanism were measured using a one-dimensional load cell, and filtered using a third-order low-pass digital Butterworth filter for different flapping frequencies, angles of attack and velocities. From the analysis, it was indicated that the thrust increased when the flapping frequency increased, but decreased as the free-stream flow velocity and angle of attack increased. The reported aerodynamic information, however, was limited to cases with the same aeroelastic parameters.

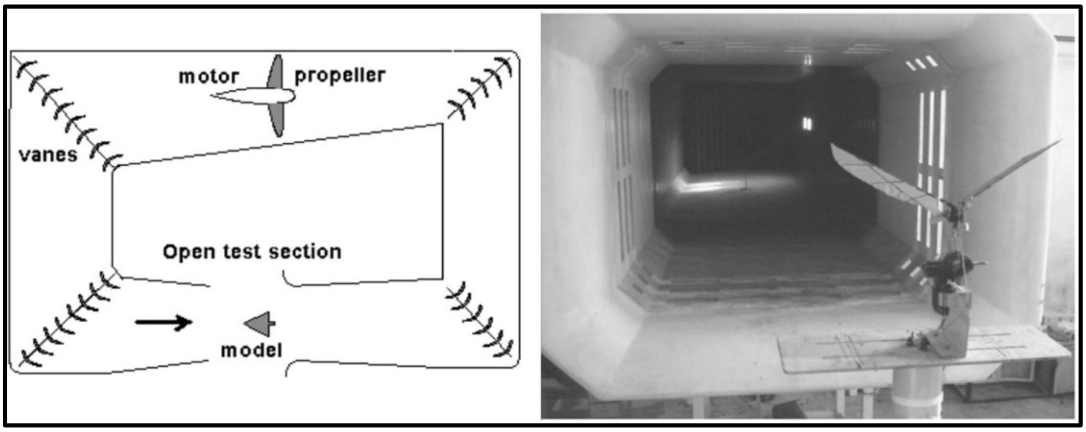

Figure 2-10 Flapping wing system in open test section wind tunnel (image taken from Ref.[118])

In the interests of developing a flapping wing micro air vehicle, an experimental robotic wing model (flapper), similar to the model used by Van Den Berg & Ellington[77], was developed to analyse the flight mechanics and aerodynamics of an insect flapping wing[52]. Using a force-torque sensor mounted near to the wing base, the flapping forces and moments were measured, and the data was filtered using a Butterworth filter. Four different experimental analyses were carried out on the following parameters: optimal stroke amplitude; optimal flip motion; optimal angle of attack; and optimal stroke-plane inclination. From these, it was realised that some unforeseen motion from the experimental model occurred, which is presumed to have influenced the results to some degree. The analysis, however, explained the contributions to aerodynamic performance of the optimal wing inertia and stiffness.

Due to the physical size of the insect, together with the unsteady flow field, the dependence of wing motion on the body orientation, and also the flow produced by high flapping frequencies, measuring and analysing the data from the physical experimental model was found to be rather difficult[13,74]. It was reported that, in dynamically-scaled fluid mechanics models, measuring the flight muscle-thorax-wing system dynamics, and the torque biases from manufacturing inconsistencies, was found to be difficult due to the small scale of the robot and the limitations of commercially available sensors[4]. The use of fluid in a flow visualisation experimental approach meant that the wing inertia could not be addressed accurately, because the hydrodynamic pressure of the liquid was much higher than the inertial force of the wing[81].

2.3.2 Flying Insect Prototypes

This section is intended to highlight some other related projects that have been carried out by numerous research institutions and agencies around the world in the last decade. This provides an insight into some of the present MAV/NAV performances, and the systems and mechanisms involved.

Table 2-3 Robotic flapping wing design systems and mechanisms.

Institution	System and Mechanism						Flight Performance		
	Wing Actuation	Weight (gram)	Wingspan (meter)	Stroke Amplitude (degrees)	Insect	Frequency (Hz)	Flying Durations (seconds)	Power to Weight Ratio (W/kg)	Flying Capabilities (m/s)
Naval Postgraduate School, USA[120]	DC motor (Bi-plane wing)	11	0.230	-	-	20	1200	-	Forward flight (2-5)
Delft University of Technology, Netherland[121]	DC motor	14	0.280	30	Dragonfly	14	-	~100	Hover, Forward (7) & Backward Flight (1)
Cornell University, USA[43]	DC motor	24	0.420	-	Hawk moth	20	33	289.8	Hover
Georgia Institute of Technology, USA[122]	Solenoid	30	-	90	Dragonfly	-	-	-	-
Konkuk University, Korea[123]	DC motor (off-board power)	6.21	0.125	145	Beetle	39	0.95	-	Take-off (0.1)
Harvard University, USA[4]	Piezo-electric (off-board power)	0.08	0.030	110	Hoverfly	120	20	237.5	Hover

Since the year 2000, numerous robotic flapping wing designs and systems have been developed, based on several types of energy source, and using various wing actuation mechanisms, using either passive or active controllers, or a combination of both. A brief summary of the robotic flapping wing design systems and mechanisms involved, along with their flight performances, are summarised in Table 2-3.

On a real insect, the wing pitch motion for fine-tuning of rotation dynamics is achieved actively with additional musculature[68]. However, to control wing pitch, current flying robotic insects remain reliant on passive wing rotation resulting from the flexibility of the wing[4,43,107,124]. Further review of flying insect prototypes, the reader is referred to Ref.[125].

2.3.3 Numerical Models

A vast range of numerical models exists for the predictive simulation of aerial locomotion. These models have been providing numerous solutions to a variety of problems with varying degrees of success, including the aerodynamic modelling of insect flight. Therefore, in identifying the best-suited model, one may prefer a model that offers a compromise between physics and rapidity of calculation.

Unlike in modelling the flight of a fixed or rotary wing, the construction of an aerodynamic model of insect flight may encompass kinematic movements that are more complex, requiring the aerodynamic model to be incorporated together with a mathematical optimisation, to resolve the complexity of the wing motion and to obtain the corresponding aerodynamic loads at the same time.

The used of a method that is able to track those changes in the flow field offers the best solution in terms of accuracy. This includes the methods that can be classified as Eulerian and Lagrangian; the first is based on a computational grid or mesh that can be solved using Navier-Stokes equations[86,89,126], while the second is a grid-free method that uses a set of particles to track the flow properties in the flow field, such as the Unsteady Vortex Lattice Method[94,127,128] and the Unsteady Discrete Vortex Method[95]. The amount of computation required by the Eulerian and Lagrangian methods is high compared to other aerodynamic methods. Although this method is able to produce comprehensive histories of the forces and flow structure of the fluid, the role of each individual fluid dynamic mechanism on force generation is generally difficult to disintegrate and analyse[12]. Furthermore, these approaches tend to be reliant on the surface geometry of the wing, which requires the detailed information to reconstruct the geometries of real wings, therefore formulating an extended model that is generic and scalable would be difficult.

As mentioned earlier, the wing motions of an insect during flight are complex, hence the use of any grid-based methods would suffer extra computational cost, since they have to adapt the unremitting changes of the grid at each time-step due to the positional changes of the wing[129]. In addition, maintaining numerical stability and achieving a converged solution may be difficult without a great deal of user intervention, due to the deformation of the grids. Therefore, considering the problems that need to be addressed on the present subject, the Eulerian and Lagrangian methods are not deemed to be feasible.

Among other advanced numerical predictive methods, panel methods are one of the most widely used in the aerodynamic modelling of fluid flow. Unlike the Eulerian and Lagrangian methods, this method can predict aerodynamic loads from analysis of fluidic singularities modelled on the body surface, without the need to resolve the flow properties across a domain. Due to its lower computational expense compared to that of the two methods discussed earlier[129], it has attracted many researchers in the field of flapping wings[130,131].

Along with their advantages, however, panel methods have the limitation of being unable to account for the shape of the wake. Using this method, the geometry of the wake can be prescribed, based on experimental evidence; alternatively it can be solved explicitly, but this approach tends to diverge owing to intrinsic singularities of the vortex panels in the developing wake, leading to substantial computational cost[132]. In addition, this method is generally only relevant for cases within the limits of attached flows[133]. Moreover, under certain flow conditions, this method is not able to capture the effects of stall, which leads to erroneous prediction of aerodynamic forces (over-prediction of lift and under-prediction of drag). Nevertheless, this method perhaps offsets its deficiencies with its moderate computational cost.

The classical lifting line theory developed by Prandtl a century ago has endured the developing knowledge of the aerodynamics of flight, in particular for the assessment of the aerodynamics of a finite wing. This method predicts the reduction of lift along the whole wingspan, due to the change of the local flow direction induced by the free vortices in the wake, formed by the wing movement. The review by Smith *et al.*[130], noted that the applicability of the classical lifting line theory for modelling the flapping flight of organisms is limited in assessing low amplitude wing kinematics.

The study by Mostafa & Crowther[12] shows that the use of lifting line theory is applicable for the analysis of a flapping wing; this approach was developed by adapting an equivalent angle of attack to the existing lifting line theory, and has shown good agreement with several different insects in hovering flight. Despite its ability to account for the induced effects, this approach does not address some other important flow physics components, such as the rotational and added mass effects.

W Froude initiated the blade element theory in a rather crude form in 1878, while S Drzewiecki further refined the theory in his book entitled "Theorie generale de l'helice"[134]. The principle of the theory is to consider the forces acting on the propeller blades or wings while interacting with the fluid. It offers a robust method that is suitable for the preliminary design of rotary wing vehicles, to predict the aerodynamic forces and torques on the wing with a low computational cost[132].

Similar to the lifting line theory, this method is able to account for the geometrical shape of the wing. However, on its own, it is unable to account for the induced flow effect on the wing. Therefore, integration with the momentum theory is often the preferable solution to reconcile the absence of the induced flow effects. The integration between the blade element and momentum theory is known as blade-element-momentum theory (BEMT). As shown by Berman & Wang[17], the blade element method has turned out to be sufficiently accurate for predictive simulation of insects in hovering flight, with regard to the complexity of the insect wing motions. In addition, this method is also practical for integration with a mathematical optimisation model, due to the rapid solution times. Furthermore, with its simplicity, no modifications would be needed for the model when simulating different flight conditions[129]; therefore, due to its greater robustness than others, this method will be employed in the present work.

2.4 BLADE ELEMENT AERODYNAMIC MODELS

The blade element theory is based on an analysis involving dividing the propeller or wing into a large number of elements[132]; it is solved by modelling each of the elements as a series of quasi-two-dimensional aerofoil elements, with known aerodynamic properties. The properties are usually obtained empirically from experimental measurement, or via a theoretical model (e.g. thin aerofoil theory). The corresponding aerodynamic forces are calculated at an aerodynamic control point on each wing element. The movement trajectory of the wing and alignment of the local wind velocity vector will be utilised in calculating the aerodynamic loads on each local wing element (the details of this theory are given in Appendix C).

In order to have an acceptably accurate estimate of small insect-size flapping wing flight performance, some blade element aerodynamic models were chosen to be reviewed. Listed in chronological order below are twelve models; the flight modes and the physical aspects of flow effects captured by each model are summarised in Table 2-4.

Blade element aerodynamic insect flight model	Flight modes	Wing inertia	Added mass	Viscous friction	Translational lift	Rotational lift	Rotational drag	Axial induced flow	Radial induced flow
Willmott & Ellington[135]	h,f	x	-	-	x	-	-	x	-
Wakeling & Ellington[136]	ff	x	-	-	x	-	-	x	-
Dickinson *et al.*[113]	h	x	x	-	x	x	-	-	-
Berman & Wang[17]	h	x	x	x	x	x	-	-	-
Faruque & Humbert[101]	h	x	x	-	x	x	-	-	-
Khan & Agrawal[52]	h	x	x	-	x	x	-	-	-
Truong *et al.*[137]	h	x	x	-	x	x	-	x	-
Orlowski & Girard[138]	h	x	x	x	x	x	-	-	-
Stanford *et al.*[139]	h	x	x	x	x	x	-	-	-
Taha *et al.*[18]	h	x	x	-	x	x	-	-	-
Nabawy & Crowther[140]	h	x	x	-	x	x	-	x	-
Nakata *et al.*[141]	h	x	x	x	x	x	x	-	-
Present model	h,f,a	x	x	x	x	x	-	x	x

Table 2-4 The flight modes ('h' – hover, 'f' – forward, 'a' – accelerating, 'ff' free flight) and the physical aspects of flow effects captured ('x' – captured, '-' not captured) by the corresponding model.

Willmott & Ellington[135] proposed an aerodynamic model to investigate the aerodynamic significance of the kinematic variation, with regard to the power requirements and the nature of the constraints for an insect at different flight speeds. The analysis is based on the free flight of the hawk moth[142] (Manduca sexta). The model includes the drag of the body, and the induced flow effect, following the formulation derived by Stepniewski & Keys[143] for the analysis of helicopters in forward flight. In their analysis, Willmott & Ellington identified that the mean lift coefficient would vary considerably with changes in wing kinematics, due to the unsteady aerodynamics. In addition, they have also identified the need to incorporate new methods, so that the instantaneous forces can be accurately simulated.

A quasi-steady model was developed by Wakeling & Ellington[136] to analyse the free flight of the dragonfly (Sympetrum sanguineum) and the damselfly (Calopteryx splendens) - lift force and power requirements are the focus of the study. The contributions of yaw and acceleration were included in the analysis. Similarly to the aerodynamic model of Willmott & Ellington[135], this model also accounts for the induced flow effect[143]. Prediction of the maximum muscle-mass-specific power for dragonfly and damselfly was given at 156 and $166\, W/kg$, respectively. From the measurements of heat production on the thorax, the flight muscle efficiency of dragonfly and damselfly was estimated at 13% and 9%, respectively. The model provides reasonable estimates of the aerodynamic and inertial power; however, similar to the model of Willmott & Ellington[135], the contribution from other physical aspects of flow effects is not included (e.g. rotational lift, added mass).

The aerodynamic model by Dickinson *et al.*[113] was formulated in accordance with experimental work on a submerged rotating wing model (assumed to act as a rigid flat plate) in a liquid filled container. The wing model was driven by a set of motors and gears mimicking the kinematic motions of the flapping insect wing. A set of sensors was linked to the wing model assembly, extracting the instantaneous reaction force data. The aerodynamic forces were calculated via a blade element method. The model also includes the force components of the wing translation, rotation, and the added mass effect[144]. Nevertheless, this model was found to be deficient in some other important elements, such as the effect of viscous forces and induced flow effects.

The aerodynamic model of an insect flapping wing by Berman & Wang[17] was developed with the intention of creating a model with the ability to predict the minimum energy consumed by a specified kinematic motion of a flapping wing insect during hovering flight. It was based on the two-dimensional Navier-Stokes numerical analysis by Pesavento & Wang[145] and Andersen & Pesavento[146], and also the experiment by Andersen & Pesavento[147] of a free fall tumbling flat plate in an oil-filled container with a Reynolds number of $\sim 10^3$. Three different insects were used as the test subject, each with approximately one order of magnitude greater mass than the previous, namely the fruit fly, bumblebee, and hawk moth. The wing was modelled as a thin rigid flat plate, and pinned in space, with the wing kinematic motion realised by rotations about a fixed joint (the wing root), which was allowed to move in three rotational degrees of freedom, similar to the aircraft yaw, roll, and pitch motions. In particular, the kinematic motions of the insect wing model were established from a combination of triangular, sinusoidal and trapezoidal waveforms. The wing cross-section was assumed to vary in a half-elliptical form along the wing span, following an earlier assumption by Weis-Fogh[96]. The aerodynamic forces were calculated via blade elements, and the aerodynamic force constants were taken from models of insect flapping wing experiments[113,148,149]. The model was developed based on quasi-steady aerodynamic assumptions, and able to capture the force components resulting from the wing translation, wing inertia, fluid flow circulation, viscosity effect, and added mass effect. A hybrid optimization algorithm[150] was then used in searching for the optimum wing kinematic motion. The added mass effect was derived from the analysis by Sedov[144] of the motion of an infinitesimally-thin two-dimensional plate in an inviscid fluid. This model, however, was only presented for hovering flight, and was still unable to incorporate the induced velocity effects.

In creating a nonlinear simulation of a Drosophila-like insect (Fruitfly), an extended quasi-steady wing aerodynamics model was developed by Faruque & Humbert[101]. The model was developed by coupling the perturbation states with the six degrees of freedom of rigid body flapping wing kinematics. The instantaneous forces generated from the sinusoidal wing kinematics motion was computed via the blade element aerodynamics model by Sane[151], and the aerodynamic force constants from Sane & Dickinson[100]. From the analysis, the passive aerodynamic mechanism revealed the important contributions to the stable manoeuvrability of insect flight, along with their minimal neural processing requirements. Throughout the analysis, the wing was assumed to act as a rigid flat plate, yet the function describing the half-ellipse shape of the wing along the span was not specified. Furthermore, the angle of attack was calculated as a summation of the wing geometrical angle of attack (also referred to as the pitching angle), and the inverse tangent of the vertical to horizontal velocity component. In a similar way to the model by Sane & Dickinson[100], this model does not consider the influences of the induced flow effects.

Khan & Agrawal[52] used a numerical and experimental approach to optimise and analyse the hovering kinematics of insect-sized flapping wings for MAV applications. In their numerical model, a simplified dynamic model of a Diptera thorax was developed to ascertain the optimal wing kinematics that would maximise the hovering flight aerodynamic performance. The insect body was assumed to be fixed in place, while the wing was allowed to move or rotate freely. The wing movement was identified by three successive rotations with respect to the model inertial reference frame. The quasi-steady aerodynamic model, based on a blade element, was applied in modelling the wing-thorax model to predict the instantaneous aerodynamic load distributions along the wing of the specified kinematics; this also includes the passive wing rotation at the end of each stroke. From the analysis, it was found that advanced rotation with carefully-controlled flip duration near the end of the wing stroke could offer advantages.

A compromise was needed in attaining the maximum average lift to drag ratio and the average lift, since they were both reaching their optimum at different times during the cycle. However, as pointed out by Parslew[152], the aerodynamic model by Khan & Agrawal[52] was reasonably unconvincing because the aerodynamic force coefficients used were obtained by calibrating their computed theoretical model against the measured experimental results. Further difficulties may also be encountered, such as when judging the substantial contributions from the force components for added mass and rotational lift. Moreover, since the work of Khan & Agrawal[52] was only performed for a single case study using undefined thorax spring stiffness values, their main contributions in predicting the optimised wing kinematics that maximise the mean lift and mean lift to drag ratio were considered rather vague.

A blade element model for the estimation of forces generated by a beetle mimicking flapping wing system was developed by Truong *et al.*[137] to estimate the aerodynamic forces produced by a freely-flying beetle. The aerodynamic model and the morphological data including the wing shape was based on the blade element model of Sane & Dickinson[100], using the aerodynamic force constants obtained by Dickinson *et al.*[113]. The effects of added mass, and the wing rotational and inertial forces were also incorporated into the model. This model was validated prior to the work by Dickinson *et al.*[113]. Using a high-speed camera, the wing kinematic motion of a freely-flying beetle was captured, and was then used to calculate the estimated force produced via the aerodynamic model. The measured and the calculated results were then compared, and it was found that they were in good agreement. The model accounts for the axial component of the induced velocity effects; however, the exact method was not explicitly specified.

For the purpose of providing a basis for the analysis of the system response due to aerodynamic inputs, stability, and control strategies, Orlowski & Girard[138] developed a numerical model to simulate the non-linear dynamics of a flapping wing, which includes the inertial coupling effects of the wings on the central body due to the continuous motion of the wings. A true insect flight with three degrees of freedom (rotation angles) relative to a stroke plane was used to replicate the differences in the position and orientation of the body, due to differing wing masses and the aerodynamic forces and moments during flight. The flapping wing-body system was modelled as a rigid body and comprised a body (thorax) and a pair of wings (rigid rectangular flat plates, with aspect ratio 5.65), mimicking the kinematics of a hawk moth established from the morphological data by Willmott & Ellington[135]. Along with the availability of aerodynamic force constants by Usherwood & Ellington[148], and the blade element aerodynamic model by Berman & Wang[17], the instantaneous forces generated by the wing kinematic motions were analysed in 12 degrees of freedom. The analysis indicated that the influence of the wing mass on the central system of the body (thorax) was crucial, and cannot be considered negligible, particularly for future control studies[138]. The model included linear and circulation terms as well as the added mass effect, yet excluded the induced velocity effects.

Following the aerodynamic model by Berman & Wang[17], Stanford *et al.*[139] extended the model to look into the non-linear dynamics of a vehicle with two flexible flapping wings with eight degrees of freedom. The modelling was performed by grouping the respective equations, with the body dynamics computed via a quasi-steady blade element method, and the wing deformations via a periodic shooting method and Floquet multipliers. The wing shape varied in thickness, and was assumed to act as a flexible flat plate, allowed to deflect in the span-wise direction. The study concluded that the kinematic variables have greater potential for improving the stability; the closed-loop control was particularly necessary in the presence of a disturbance, and the chord and thickness variables were more adept at minimising the energy needed. Nevertheless, the model does not include the induced velocity effects, and the number of elements (i.e. 10) as well as the time steps (i.e. 100) seems inadequate in avoiding the influences caused by the discretisation errors.

A state-space formulation for the aerodynamics of flapping flight was presented by Taha *et al.*[18] to capture the leading edge vortex (LEV) contribution to the wing; this model was developed to predict the static lift due to a stabilized LEV via Duhamel's principle. The unsteady lift due to arbitrary wing motion is determined by embedding the effects of aspect ratio in the empirical formulae to predict the static lift due to a stabilized LEV. In addition, they have also introduced a reduced-order model that is more suitable for flight dynamics and control analyses of flapping flight. In this model, some physical aspects such the LEV, unsteadiness, and rotations have been accounted for in determining the lift force. The model was able to predict the temporal lift build up due to stabilized LEV, including the lag and phase shift associated with unsteady flows, with a good agreement of the modelled lift time-histories compared to the Navier–Stokes solutions of Sun & Du[126] for several different insects. Even so, the model was unable to include the viscosity effect, as well as addressing the contribution of the induced flow effect.

An analytical method for modelling the aerodynamic performance of insect-like flapping wings in normal hover is presented by Nabawy & Crowther[140,153]. The model was developed by integrating the axial momentum theory with the lifting line theories to quantify the losses captured in the induced power factor. Validations are performed for eight insect cases, through comparison of the results of lift force and power with the CFD simulations of Sun & Du[126]. This approach has shown an alternative method to account for the induced power factor (axial induced flow effect) analytically, without the need for experimental data. It should be noted that the drag component due to skin friction (or viscous drag) is not modelled, therefore, the model will tend to under-estimate the drag when the angles of attack are low; this is found in the case of high-speed forward flight (as illustrated by Willmott & Ellington[154], in their work on the changes in the pattern of rotation angle variation of the wing with increasing flight speed).

Nakata *et al.*[141] have proposed an aerodynamic flapping wing model based on the blade element theory, called the CFD-informed quasi-steady model (CIQSM). The assumptions of the model are mainly based on the work of Sane & Dickinson[100] and Berman & Wang[17]. The model also includes the drag force due to wing rotation around the span-wise axis of the wing (i.e. rotational drag). In order to account for this effect, the wing is divided both in the chord-wise and span-wise directions. The model is validated using the example case of a hovering hawk moth, by comparing the aerodynamic forces to the CFD results obtained earlier[89,155]. The value of the rotational drag coefficient is based on the maximum value of the drag coefficient (at $\alpha = 90°$) measured by Usherwood & Ellington[148]. Results have indicated that the rotational drag gave a notable effect during stroke reversal, due to the high acceleration and rapid rotation of the wing. Nevertheless, the model is unable to account for the contribution of the induced flow effect.

Of the twelve blade-element aerodynamic models reviewed above, most are found to share similar basic components in formulating the aerodynamic model of insect flight. The aerodynamic models by Sane & Dickinson[100] and Berman & Wang[17] are among the most popular options; comparing these two models, the model by Berman & Wang[17] is more applicable to the present problem, since it is able to capture more fluid flow effects compared to the model by Sane & Dickinson[100]. Nevertheless, the model by Berman & Wang[17] is still unproven in predictions related to forward flight, and does not include some other important elements, such as the induced flow effect. Therefore, this model will be reconstructed with the momentum theory to accommodate the induced flow effect for the present analysis. Further details on the aerodynamic modelling of flapping flight can be referred to in work by Mueller[156], Shyy *et al.*[64], Wang[157], Ansari[12], and Taha *et al.*[158].

2.5 OPTIMISATION OF FLAPPING INSECT MODELS

Over the past decade, numerous studies have been conducted to optimise the flight performance of the flapping wing. These mathematical optimisation studies have been directed to a wide range of analysis, focussing on various aspects of optimisation such as the wing kinematics[2,17,52,82,104,152,159,160], wing shape[127,161], wing structural aeroelasticity[162], flight stability[139], and wing-body dynamics[163].

A numerical gradient-based optimisation method was used by Tuncer & Kaya[82] to optimise the thrust and propulsive efficiency of an flapping airfoils undergoing a combined plunge and pitch motion. The amplitudes of the plunge and pitching motions and the phase shift between them at a fixed flapping frequency are taken to be the optimisation variables. The problem was computed numerically using a Navier–Stokes solver on moving overset grids. From the study, Tuncer & Kaya[82] show that a high thrust value is possible to attain, however this is at the expense of propulsive efficiency.

In the study of optimal wing kinematics in hovering insect flight, Berman & Wang[17] used a hybrid optimisation algorithm by combining aspects of a genetic algorithm[150] and a gradient-based optimizer[164]. This allowed them to explore the kinematics that minimises the required power while maintaining sufficient lift to perform hovering flight. The optimisation process proceeds in two steps, with a population of 200 parameter sets. Firstly, a genetic algorithm evolves and narrows the population in a globally-minimal basin. Then, the gradient-based simplex algorithm relaxes each of the parameter sets for final local optimisation. The results of the optimisation indicate that the wing kinematics is similar to the observed data in the literature.

Conforming to the study by Ghommem *et al.*[161], a gradient-based optimizer was combined with the unsteady vortex lattice method to optimize the shape of flapping wings. The study was conducted to provide guidance for shape design of engineered flying systems, by classifying a set of optimized shapes that maximise the propulsive efficiency (i.e. propulsive power over the aerodynamic power), with constraints on the lift, thrust, and area of the wing in forward flight. The study indicated that the optimal shapes are reliant on the reduced frequency, and with the camber line, the leading- and trailing edges are the key wing shape parameters.

A gradient-based optimiser developed by Svanberg[165], known as the moving asymptotes method, is used by Stanford *et al.*[139] to study the nonlinear dynamics of a vehicle with two flexible flapping wings; it is modelled by combining the body dynamics and wing deformation into a single system of equations to represent the flapping wing vehicle system. The model was optimised for six different test cases of power-per-weight ratio in a full wing-flapping-cycle criterion, and was coupled with a quasi-steady blade element method[17] to allow the quantification of the role of multiple wing variables - this includes the planform, wing structure, and kinematic actuation variables. From the optimisation results, it was shown that the kinematic variables have a greater effect on improving the stability, whilst the wing geometrical variables (i.e. wing chord and thickness) have greater influence on reducing the energy required.

Following assessment of some of the optimisation techniques as above, the genetic algorithms and gradient-based optimiser are among those regularly used in the study of flapping insect flight, while some studies[17,161] opt to combine multiple optimisation techniques in the search of the optimal solution. Nevertheless, as noted by Chen *et al.*[166], when compared with other optimisation methods, the particle swarm optimisation is reported to be much simpler to implement and more efficient for computation. In addition, this method is unrestricted by assumptions, and offers a reduced number of function evaluations; it has become one of the most popular techniques for solving continuous optimisation problems[167].

2.6 AERODYNAMICS OF FLAPPING INSECTS

From various analyses of flapping insect wings (via experimental measurements, numerical calculations, or prototype developments), numerous factors, effects, and mechanisms for lift enhancement beyond traditional aerodynamic theory have been established; these could be readily applied to enhancing the performance of flapping wing flight. Hence, a brief review of the topic is important in order to highlight the enormous possibilities of parameterising the kinematics of the wing motion of certain types and conditions of flight.

In this section, some important factors that would have a major influence on the aerodynamic flight performance of an insect will be discussed. As found in the literature, these include factors such as the tip vortex (TV); trailing edge vortex (TEV); leading edge vortex (LEV); wake capture; wing flexibility effects; wing rotation; tandem wings; and wing shape.

2.6.1 Vortices (LEV, TEV, TV)

As shown in the work of Brodsky[168], by observing the flapping wing of a peacock butterfly in a wind tunnel using slow motion film, the result showed the production of coupled vortex rings on the wing. Similarly, another study on vortex formation using an alternative dust flow visualisation technique during tethered flight further revealed specific differences in the vortex ring formation[70]. However, only a single vortex ring was observed on each stroke, in contrast to that reported earlier by Brodsky[168]; this happened because there was no place near to the wings for a new ring to form during an upstroke. Both studies, however, were unable to draw a conclusion on the flow characteristics near to the wings, due to the limited capabilities of their techniques in detecting the small LEV bubbles.

Due to the limitations of their techniques, as discussed above, better techniques are necessary to more accurately measure and explain the flow characteristics near to the wings. Research using three-dimensional models has shown that the LEV forms and increases in size at the beginning of the down-stroke, as the wing progresses to the end of the down-stroke, forming a conical spiral shape which is swept by the radial flow towards the wing-tip[77,111,169]. To investigate the wake structure, smoke visualization studies on tethered moths were carried out to look into the details of the flow field around the wings[112]. The study indicated that the down-stroke plays a more important role in generating the lift forces than the up-stroke, and the radial flow swept towards the wing tip provides the stabilisation during the full-stroke of the flap sequence. This is in agreement with the flow measurement conducted by Bomphrey *et al.*[71], where LEV was observed above the wings, grew continuously along the span of the wing, and then transformed into tip vortex (TV) as it reached the wingtip.

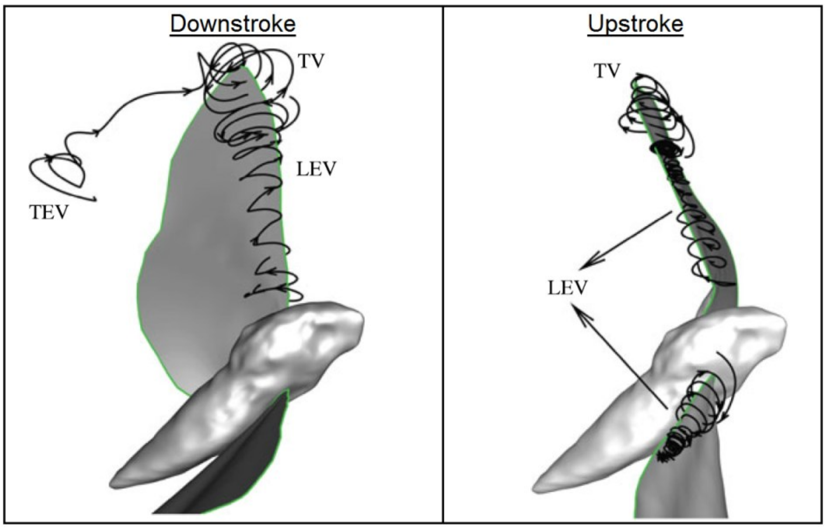

Figure 2-11 The three-dimensional vortex topology plots of tip vortex (TV), trailing edge vortex (TEV), leading edge vortex (LEV) during downstroke (left) and upstroke (right). Image taken from Ref.[104].

From a study of the span-wise flow (radial flow) and the attachment of the LEV on a robotic insect wing model, measured using digital particle image velocimetry (DPIV)[72], it was found that the attachment of the LEV on the wing could be prolonged by systematically mapping and limiting the span-wise flow with fences (teardrop-shapes) and edge baffles. Moreover, the study also reported that the flapping wings did not generate a spiral vortex, and the growth of the LEV was limited by the downward flow induced by TV[72]. On the other hand, a study on the flapping hawk moth using propeller-like rotation models demonstrated that a LEV was created by the dynamic stall, and was retained by the span-wise flow during flight[148].

Interestingly, as noted by Mostafa & Crowther[170] in their reviews following the experimental studies on model insect wings, for three different modes of motion (i.e. parallel translating[148], revolving[107], and flapping[171]) the wing lift is almost the same at small angles of attack. As the angle of attack increases to the higher region, it was shown that the parallel translating wing loses its lift due to the stall condition, but for the revolving and flapping wings, the lift will continue increasing to its maximum at an angle of attack 45 degrees. This may be due to the continuously-attached and stable formation of a LEV on the top surface of the wing[72,148,169].

Phillips *et al.*[172] investigated the effect of aspect ratio on the LEV over an insect-like flapping wing in a high spatial resolution flow field measurement. The flow field around a flapping wing (a mechanical robotic device) was measured via particle image velocimetry. The wing was rigid and rectangular, with an aspect ratio ranging from 1.5 to 7.5, and the simulation was performed at a constant Reynolds number of 1400; the comportment of a high-lift wing was confirmed, and the primary LEV was captured and observed to grow with increasing aspect ratio. The results also revealed that the LEV is initiated from a focus-sink singularity on the wing surface close to the tip, and formed an arch-shape. For a wing with aspect ratio of $1.5 < AR < 3.0$, the detachment of the LEV occurs around the mid-down-stroke at $\sim 70\%$ span. For a wing with an aspect ratio of over three, bigger and stronger vortices continued to form beneath the wing. On the second half of the stroke, however, the lift was shown to decrease, because the leading edge vortices from the preceding half-stroke slip into the succeeding half-stroke. The lift ascribable to the LEV increased with aspect ratio values of up to six, while wings with higher aspect ratios exhibited less lift distally; this is because of the disintegration and the prolongation of the preceding LEV's under the wing, on the outer and the inner part of the wing, respectively.

Along with the recent development of high-speed computational facilities, the advancement in numerical modelling has allowed researchers to make rapid progress in advancing the understanding of insect flight. A three-dimensional computational fluid dynamics model was constructed by Liu *et al.*[83] to study the unsteady aerodynamics of the flapping wing using the geometry and kinematics of a hovering hawk moth. The simulation of the translational motion during the up-stroke and down-stroke detected a coherent LEV, which was found to cause a negative pressure region on the upper surface of the wing. This analysis agrees well with Van Den Berg and Ellington[111], where the lift forces were mostly generated during the down-stroke, and the vortex was shed before the subsequent translational motion[83,104]. Elsewhere, Wang[173] conducted a two-dimensional analysis, focusing on the frequency selection in forward flapping flight to investigate the time scales associated with the shedding of the TEV and LEV. It was observed that the optimal frequency was inversely proportional to the dimension of the wing, particularly at a Strouhal number of 0.7; this is consistent with earlier research findings as reported by Hall *et al.*[174].

2.6.2 Wake Capture

During flight, insects rapidly change their wing flapping direction at the end of each stroke, thus increasing the effective fluid velocity at the start of the next stroke[113]. This movement continuously allows the wing to capture the shed vortices from the previous stroke, and hence greatly improve the overall efficiency of the force produced. Therefore, with the ability to extract energy from its own wake that develops immediately after the wing changes direction at the start of each half stroke, this could explain how the wake capture mechanism works[49]. In a study by Dickinson *et al.*[113], the wake capture mechanism was analysed by examining the time history of the generated forces over several hundred milliseconds at the end of the upstroke (Figure 2-12). The study[113] indicates that when the wing rotated before reaching the end of the stroke (advanced rotation), it is able to generate higher peak lift force compared to when the wing rotated at the end or after the stroke.

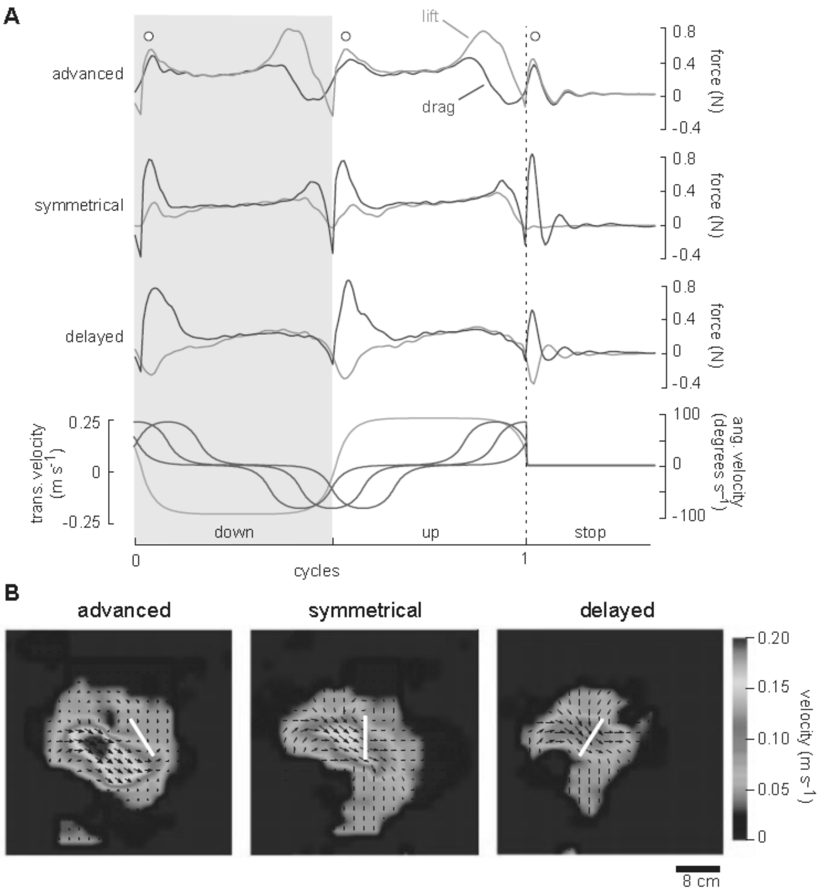

Figure 2-12 The transient forces on each half-stroke during continuous flapping (A), and the flow visualizations several hundred milliseconds following the end of translation (B). Image taken from Ref.[113]

In a study by Sane & Dickinson[100,175] it was shown that the rotational circulation and the wake capture effect could be isolated by changing the wing motion patterns near the end of the stroke. They observed that the peak force due to the rotational circulation occurs when the wing rotates before reaching the end of the stroke, whereas the peak force due to the wake capture effect occurs when the wing rotates at the end of - or after - the stroke reversal; this was due to the force being promoted through the shedding of the vortices from the previous stroke, induced by an increase in flow velocity towards the wing[176,177]. Sane & Dickinson[175] also suggest that the control of flip timing and duration could be used in controlling the forces on both left and right wings, as required for the regulation of force-moments in flight control. Using two-dimensional numerical simulations, Wang[157] and Shyy *et al.*[178] also observed similar conditions to those reported earlier by Sane & Dickinson[100,175], Dickinson *et al.*[113], and Dickinson[177]; these included findings on the wake capture mechanism and lift augmentation of the instantaneous peak lift produced near to the end of the stroke.

Conversely, numerical studies (CFD) by Wu & Sun[179] showed that the wing wake interaction will decrease the lift and increase the drag in the remaining part of the half-stroke. , due to the wing moving in a downwash field induced by previous half-strokes' starting vortices, tip vortices, and attached leading-edge vortices – the wake is therefore detrimental to the aerodynamic performance of the flapping wing. This shows an inconsistency in the findings on wing wake interaction with those observed by Sane & Dickinson[100,175]. Nevertheless, this issue may still require some more work, due to the fact that such comparisons need to account for some other factors, such as the wing geometry (i.e. wing thickness, shape of the wing edges); the transient flow effect (more flapping cycles needed to eliminate the initial flow effect); and the medium of the fluid being used as the inertial force may dominating the measured forces[81].

In addition, the capacity (or limitation) of the model being used in order to capture the unsteady flow properties around the wing has never been discussed. This is because the model may over predict (or under predict) the size of the wake, hence the simulated result[179] may show the wing being drawn into the wake, rather than capturing the wake as observed from the experiment[100,175].

Until recently, it had been assumed that the wing captures the wake, however, following the flow measurement study by Horstmann *et al.*[180], the wake is observed to consist of two pairs of counter-rotating vortices, and deforms with time. An earlier flow visualization study of insects conducted by Bomphrey *et al.*[181] discovered a complex wake topology that may potentially lead to unreliable calculations of the efficacy of the flight performance. This is because of the location and rotating direction of the vortices, which are close and opposed to one another. Therefore, adaptation of this phenomena must be incorporated into the aerodynamic models, in order to account for the transient wake effects; the former frozen flow assumptions are no longer valid, which will prevent such erroneous prediction on the transient force vector[169,171].

2.6.3 Wing Flexibility

Flexible structures or wings are not rare in nature, and may provide some favourable advantages for survival, such as the increased drag properties of some organisms that help them fall to the ground more slowly[183–185]. From an experimental study to investigate the effect of the span-wise flexibility of the flapping wing, the flexible wing appears to be able to produce more thrust than rigid wings, although the opposite is true for lift[186]. A numerical study of the fluid-structure interactions of a hovering hawk moth has shown that the flexibility of their wings could offer a potential delay in the shedding of the LEV (as shown in Figure 2-13), hence enhancing the flapping wing's aerodynamic performance at low Reynolds numbers[187]. It was reported that the influence of wing flexibility was found to be a crucial factor in determining flight performance, and further attention is needed in order to utilise this to improve the performance of dynamic multi-body models of an ornithopter[188].

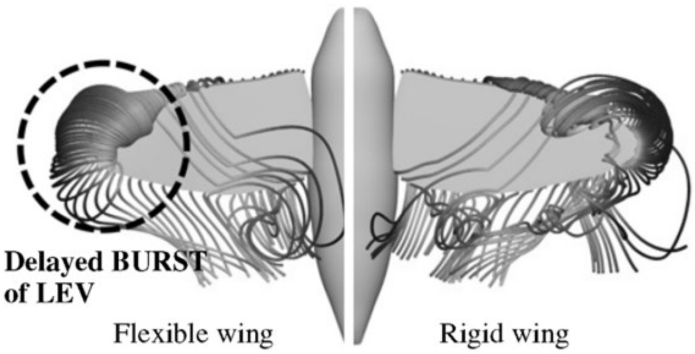

Figure 2-13 Visualisation of the delayed LEV shedding on the upper surface of hawk moth wings (downstroke, $t/T \sim 0.2$). Image taken from Ref.[92].

It has been shown that a flexible wing can generate a much stronger downstroke vortex ring than a rigid wing does[92]; this is because a flexible wing allows the wing shape to be adaptively changed in response to the unsteady aerodynamics, thus enabling improved stability and control of the LEV. It has also been observed that the flexible wing benefited from the wake capture phenomenon[189]; this occurs because the wing tends to curve into its own wake, interacting with the wing vortices that result from the previous stroke, creating a suction effect that enhances lift. The wake capture effect was observed by using the same platform of flapping wing model as the DelFly II wings model; the method involved varying the thickness of the polyester film, with the wing model being placed in a water container and analysed using time-resolved tomographic PIV.

Shin & Lee[115] carried out a computational study based on the lattice Boltzmann method to investigate the effect of wing flexibility on the generation of propulsion. It was revealed that, by carefully controlling wing rotation during flapping near to the end of the translational stroke, the wing flexibility could provide efficient flapping wing propulsion and a reduction in flow resistance. Alternatively, based on the flapping wing propulsion research utilising the Euler-Bernoulli torsion beam and the quasi-steady aerodynamics of the aeroelastic model, optimum flapping wing propulsion efficiency could also be attained by appropriately adjusting the wing-stiffness parameter[54]. Likewise, from a fluid–structure interaction study of a flapping flexible plate in quiescent fluid at low Reynolds numbers, based on the lattice Boltzmann method, it was found that the flexibility of the plate could improve the propulsive efficiency, by assisting with the production of a strong vortex at the trailing edge (TEV)[5]. Similarly, it was observed that both chord-wise and span-wise flexibility undergoing plunging motion could also enhance the thrust force produced[49].

The integration of wing flexibility on a low fidelity model (e.g. BEM) could offer a much complete model to represent the aero-structure physical nature of the flapping wing system. This is possible through the advancement of the unsteady aerodynamic theory by incorporating the effect of wake on the lift of flexible wing. However, at present, this theory is limited since it does not able to consider the instantaneous changes of the shape, density and thickness of the wing that could be constant or vary along the chord and span[190].

A further review on the effects of flexibility on the aerodynamic performance of flapping wings can be found in Ref.[191].

2.6.4 Wing Rotation

A three-dimensional computational study of the aerodynamic mechanisms of insect flight (Drosophila melanogaster) was carried out by Ramamurti & Sandberg[116]. This was based on the finite element computational method to analyse the phasing differences between the translational and rotational motions, achieved by varying the rotational motion prior to the stroke reversal. It was found that, when the wing was in advanced rotation, the peak in the thrust forces was higher than when the wing rotation was in-phase with the stroke reversal; however, the peak thrust was reduced further when the wing rotation was delayed[116]. Another computational study based on Navier Stokes equations by Sun & Tang[117] also agreed with the advance wing rotational effect observed by Ramamurti & Sandberg[116].

With advanced rotation, greater lift can be produced than that possible with symmetrical rotation, but with a higher energy demand[84]. Based on the calculated results for power expenditure, symmetrical rotation should be used for balanced long-duration flight, and advanced rotation and delayed rotation should be used for flight control and manoeuvring. A study by Lee & Shin[115] looking into the effect of wing flexibility indicated that the advance rotation could also enhance the flapping wing propulsion. Conversely, in the case of faster cruise velocity, symmetrical rotation seems to become more efficient than the advanced rotation, even with a reduced amount of driving force[5].

To achieve controllability of flight during hovers or manoeuvres in forward, backward or sideways flight, the use of advanced, symmetrical, and delayed rotation may be able to provide the required forces to improve manoeuvrability during flight. Advanced rotation is preferable when considering sustained hovering flight, symmetrical rotation for cruise flight, and a combination of advanced and delayed rotation for manoeuvres[5,84,115–117].

2.6.5 Tandem Wings

A study of the unusual phase relationship between the forewing and the hindwing of the dragonfly, using slow-motion film in a wind tunnel, indicated that the dragonfly commonly flaps with a higher stroke angle when the fore- and hindwing are in- phase[192]. It was also observed that the two wings could generate higher propulsive forces with a flapping in-phase pattern, which is normally used during take-off, yaw-turn, reverse direction, and to overcome inertia[192]. Osborne[193] indicated a technique to minimise the mechanical power required for flapping wing flight, which involves a slowing of the downbeat in a figure-of-eight flapping flight motion. This study was based on the dimensions and performance data of 25 insect types, to analyse the aerodynamics and mechanisms of insect flapping flight.

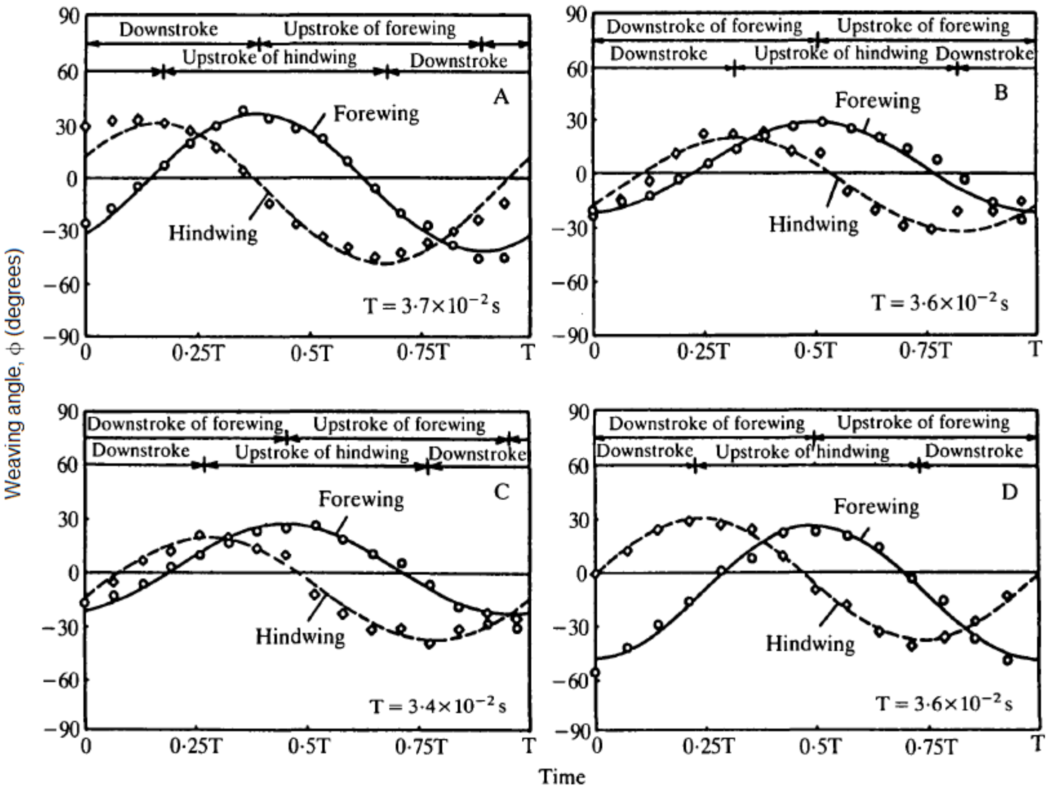

Figure 2-14 Typical time history of weaving angle of dragonfly in level flight (image taken from Ref.[194]).

Similarly, Rüppell[195] conducted a kinematic symmetrical flight manoeuvre analysis on 20 species of Odonata via slow-motion film. This revealed that there were relatively large variations in the upstroke to downstroke ratio; the variation could also be found when their wings were beating in the direction of the flight, where the total airflow over the wings was greater, as the airstream due to the wing movement was in the same direction as that due to forward movement. Conversely, when beating their wings against the direction of flight, the total airflow over the wings was reduced, since the airstream due to wing movement was in the opposite direction to that due to forward movement. In other words, the total airflow over the wings was produced by the vector addition of the airstream associated with wing movement and the velocity of the body[195]. During the down-stroke, their wings were beating against the direction of the flight. At this point, LEV forms above the wings and grew continuously along the span of the wing. It was then swept by the radial flow, transformed into tip vortex (TV) as it reached the wingtip[71]. The radial flow provides stabilisation of the vortices, enhancing the circulation, and consequently generating more lift for the wing (i.e. downstroke).

A separate analysis of the slow-motion films of Odonata in free-flapping flight has shown that the advance ratio of the forewing and the hindwing were 0.98 and 0.93, respectively. The reason for the differences in forewing and hindwing advance ratios was due to the differences in the stroke amplitude. The hindwing shows greater stroke amplitude than the forewing, because the hindwing reaches a lower position (extending 6 degrees lower on average) than the forewing. Also, the forewing motion lags behind that of the hindwing in all sequences by approximately 26 percent of the forewing period (i.e. a 94 degree phase lag, Ref.[196]). In addition, either by enlarging the wing beat amplitude or by raising the wing beat frequency, Park & Yoon[197] found a way to effectively control the advance ratio of the insect's flapping wings.

2.6.6 Wing Shape

A study on the effect of wing shape, structure, and kinematics in flapping wing flight was conducted by Stanford *et al.* [103]. The study focuses on developing a tool for minimising the peak input power required during the stroke, subject to other requirements such as sufficient lift force to sustain hover, and the generated forces not exceeding the maximum mechanical stress of the wing structure. The authors developed an aeroelastic model to account for the aerodynamic and the structural flexibility interaction of the wing during the flapping motions. This aeroelastic model was constructed by coupling a nonlinear three-dimensional beam model to a quasi-steady blade element aerodynamic model of Berman & Wang[17].

From the study[103], the authors concluded that the model was able to predict the optimum power required for compliance with the structural integrity as a result of the lift force required to sustain hover flight. In addition, it was found that flexible wing motion can differ substantially from the commanded kinematics enforced at the root, given the wider weaving and flapping angles and higher velocity of wing motions. However, the authors indicated an issue with the optimisation schemes required to achieve optimal configuration of the wing, which led them to study the wing with and without the inclusion of aeroelastic coupling. This issue is due to the unsteady nature of the problem, in which no structure may exist that is capable of continuously changing form into the optimal shape with the shifting of the flow around the wing.

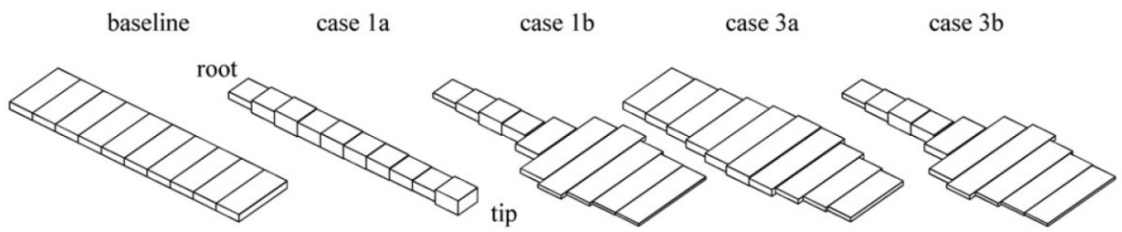

Figure 2-15 Different types of wing shapes for the study of optimum stability and power (image taken from Ref. [139]).

Continuing from their previous study[103], Stanford *et al.*[139] investigated the nonlinear dynamics of a vehicle with two flexible flapping wings. This study was designed such that the wing-body interaction can be included in quantifying the stability of the system. Similar to the previously-described study[103], the model was developed based on the blade element method to capture the aerodynamic effect, and coupled with the periodic shooting and Floquet multipliers to account for the structural effect on the wing (Figure 2-15). A gradient-based optimisation was performed via the method of moving asymptotes, to obtain the optimum design variables. The study indicated that the stability and the power were prominently influenced by the kinematic and geometrical shape (wing chord and thickness) of the wing, respectively.

The study by Stanford *et al.*[139] indicated that the optimum flapping angle of the flexible wing is wider than that of the rigid wing; this implies that the rigid wings would require a larger flapping amplitude in flight, and thus use more power. In addition, the study concluded that the chord and thickness variables controlling the shape of the wing are more proficient in reducing power requirements. Nevertheless, the study was unable to prescribe the passive deformation of the wings, or the body nonlinear motion, due to the inertial and aerodynamic forces encountered by the wing.

Following the numerical analysis on the aerodynamic consequences of wing deformation in locust flight, Young *et al.*[198] discovered an important feature that would enhanced the aerodynamic function and flight efficiency of an insect. The simulation of the flow field was performed with unsteady incompressible Navier-Stokes equations, by assuming laminar flow via a commercial CFD platform; the triangular grid and thin boundary-layer grid were used to mesh the wings and body of the insect. The model was validated with real locusts via smoke visualizations and digital particle image velocimetry (DPIV). The study indicates that the wing model with a chambered design provided greater power economy than the un-cambered model.

Recently, a new approach was taken by Ray *et al.*[199] to study the contribution of specific morphological features of wing shape to the performance characteristics of an insect in flight. They used genetic manipulation (known as targeted RNA interference) to modify the wing shape in the fruit fly (Drosophila); the results show that the aerial agility performance can be significantly enhanced by adapting this technique; it also indicates that the agility of the fruit fly is limited by its wings.

A study on the shape optimisation of rigid flapping wings in forward flight was performed by Ghommem *et al.*[161]. The purpose of the study was to identify a set of optimised shapes that maximise the propulsive efficiency by combining a gradient-based optimizer with the unsteady vortex lattice method (UVLM). This was done by examining several parameters such as the wing aspect ratio, camber line, and curvature of the leading and trailing edges, which could affect the flight performance.

Ghommem *et al.*[161] suggested that changing the wing-shape yields a significant improvement in the flapping wing's performance, i.e. lift, thrust, and aerodynamic power. The optimisation study shows that the camber line and the leading and trailing edges are the key parameters in controlling the flight performance. In addition, the optimal shapes show significant dependence on the reduced frequency, in which a significant increase in the propulsive efficiency and the time-averaged thrust are indicated at a reduced frequency. Throughout the study, however, the authors employed a small flapping amplitude and frequency, which resulted in a lower frequency ($k \approx 0.16$) than most low-Reynolds-number natural flyers. Furthermore, the angle of attack was set to ten degrees, which is relatively low in insect flapping flight.

In the study of Berman & Wang[17], the wing shape was formed by an elliptical function with the chord length of the wing, to vary like a half-ellipse along the wing radius; this shape was close to a half-tear-drop, similar to the assumption made earlier by Weis-Fogh[96]. To validate their model[17], the authors compared their results for three different insects to the direct numerical simulation results of Sun & Du[200] in hovering flight. Unlike the tear-drop wing shape of Berman & Wang[17], the wing shape of Sun & Du[200] was modelled closer to the real wing shape of the corresponding insects. The results of Berman & Wang[17] and Sun & Du[200] on three different insects are comparable, except for the lift force of hawk moth, which was been overestimated by $\sim 15\%$.

2.7 INDUCED FLOW EFFECT VIA BEMT

Generally, the induced flow can be described as the airflow that is forced through a rotor or actuator disk[132,143]. As the airflow is forced through the disk, the relative airflow (velocity vector) will be altered, which correspondingly influences the angle of attack (α), due to the presence of inflow angle[134] (ψ). This affects the overall performance characteristics in relation to the changes in the prescribed airflow resulting from the induced flow effect[16] (as given in Figure 2-16).

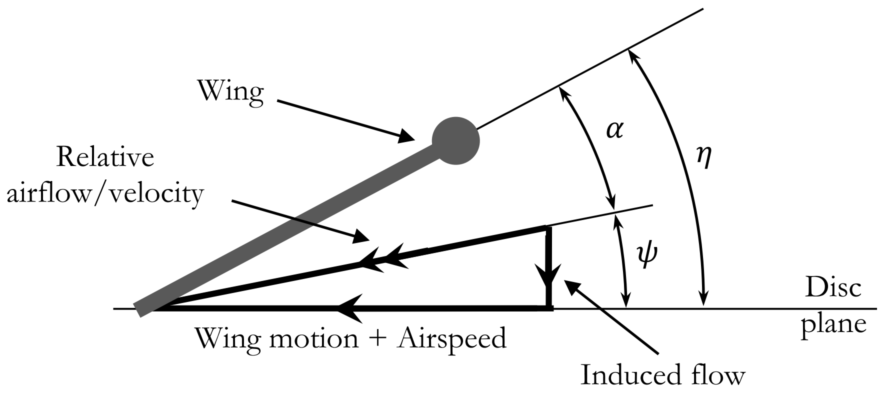

Figure 2-16 Flow geometry with induced flow effect. Wing travels in the same direction of the flight path.

The integration of the induced flow effect in insect flight (via quasi-steady blade element momentum theory - BEMT) can be found in the model of Willmott & Ellington[135] and Wakeling & Ellington[136], following the expression derived by Stepniewski & Keys[143] for helicopters in forward flight. This approach allows the determination of the instantaneous relative velocity at any given span-wise location on the wing. However, the induced velocity was assumed at a constant value, acting vertically along the wingspan and throughout the flapping cycle.

Another successful approach on insertion of the induced flow effect on insect flight can be found in the analytical models of avian flight by Parslew[129]. Here, the combination of actuator disc theory and blade element model have been used to predict uniform induced flow velocity normal and tangential to the stroke plane. In this model, the local induced flow effects were resolved in the stroke plane axes, by assuming that the induced flow effects are the same as on the wing axes.

The axial momentum theory can also be used to calculate the induced flow effect; however, this approach is distinctly independent of the wing geometry. As noted by Adkins & Liebeck[16], those approaches that are prevalent in classical design theory are only applicable for a small angle of inflow and light loading conditions, whilst in insect flight the inflow angle is relatively high[76].

The analysis of Willmott & Ellington[135] predicted that the influence of the induced flow effect on the aerodynamic power would reach over 10%, depending upon the selected profile drag coefficient. In addition, a study of avian flight by Parslew[129] has shown that the induced velocity plays a much bigger role than the added mass effect in influencing the normal force.

2.8 AERODYNAMIC COEFFICIENTS

In aerodynamic analysis, the force acting on a body moving in a fluid can be divided into two components, known as the lift L and drag D forces. For a wing, these forces were characterised based on the direction of the relative airflow, in which the drag is always parallel to the flow direction, and the lift is always perpendicular to the drag (as illustrated in Figure 2-17).

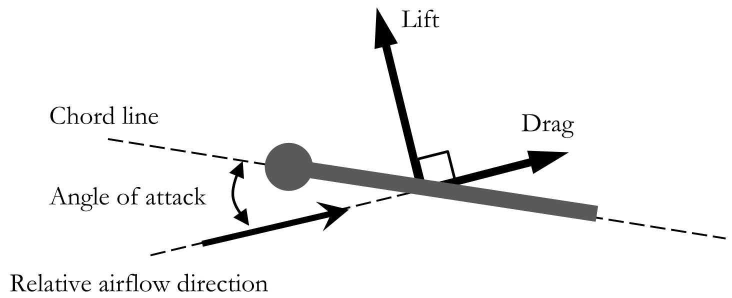

Figure 2-17 Lift, drag and angle of attack characterised based on the direction of the relative airflow.

To provide quantification of the aerodynamic properties of wings of different scales, these forces are often expressed as two dimensionless quantities, the lift and drag coefficients C_L and C_D. In a general form, the lift and drag coefficients can be expressed as

$$C_L = \frac{L}{\frac{1}{2}\rho V^2 S} \quad \text{and} \quad C_D = \frac{D}{\frac{1}{2}\rho V^2 S} \tag{2-1}$$

where ρ is the air density, V is the flow velocity magnitude and S is a reference area of the wing surface.

Under steady flow conditions, these coefficients will depend on not only the angle of attack and the geometric shape of the wing, but also on the Reynolds number (i.e. ratio of inertia to viscous forces in a flow) and the Mach number (i.e. ratio of the flow velocity to the local speed of sound). Since the flow velocity in animal flight is low, which contributes to a low Mach number, the effects of flow compressibility (i.e. Mach number) can be neglected[152].

Conventional aerodynamic theory is based on the analysis of the wing (or airfoil) moving at a constant speed. Unlike the fixed- and rotary wings that move continuously through the air, the flapping wing moves in two translational phases (down- and up-stroke), and experiences reversible motions in each phase (supination and pronation), as shown in Figure 2-18

.

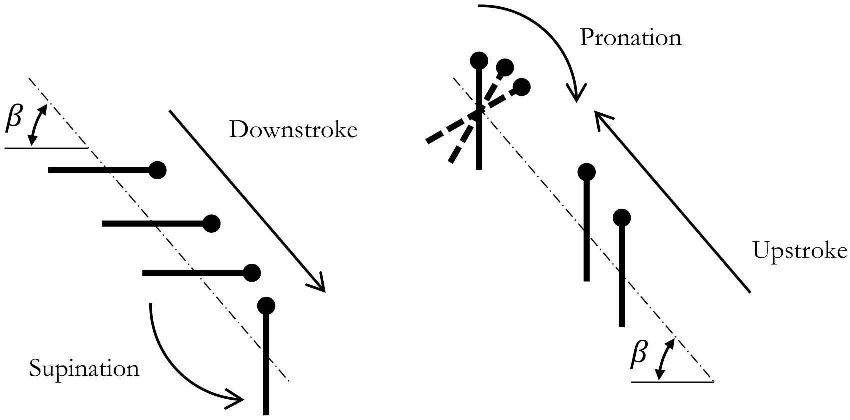

Figure 2-18 Schematic diagram of the idealised wing path during flapping motion at the end of each stroke. Adapted from Ref. [75].

For flapping wing insect flight, the lift is assumed to be a continuous function of the angle of attack, and satisfies the Kutta condition[140]. Although flapping wing (insect) operates in such higher angle of attack beyond the conventional fixed- or rotary wing that could easily violates the Kutta conditions, due to the flow separation. The presence of radial flow on the wing prevents the occurrence of this flow separation, stabilise and prolong the attachment of LEV on the wing, helps preventing the occurrence of wing stall[70–72].

Following Dickinson *et al.*[176], the coefficients of lift and drag for insect flight can be expressed as a function of the instantaneous angle of attack, which can be stated in algebraic expressions as

$$C_L = 0.225 + 1.58\sin(2.13\alpha - 7.20) \qquad 2\text{-}2$$

$$C_D = 1.92 - 1.55\cos(2.04\alpha - 9.82) \qquad 2\text{-}3$$

In a similar way, Wang *et al.*[76] fitted their experimental data and proposed much simpler expressions,

$$C_L = A\sin 2\alpha \qquad 2\text{-}4$$

$$C_D = B - C\cos 2\alpha \qquad 2\text{-}5$$

where the coefficients A, B, and C were determined experimentally.

In these approaches[76,176], however, several fundamental deficiencies were identified. For instance, they require *a-priori* knowledge of the lift and drag, and they do not account for the unsteady aspects associated with flapping flight. Moreover, the coefficients describing the aerodynamic terms in those models are determined empirically, and typically do not account for any variations in the wing shape. This latter concern would not be valid for any arbitrary wing, as those coefficients could change considerably with variations in the wing aspect ratio[201].

Since flapping flight is associated with low aspect ratio wings, one can use the Extended Lifting Line Theory (Schlichting & Truckenbrodt[202]) to obtain the dependence of $C_{L\alpha}$ on the wing aspect ratio AR, which is given by

$$C_{L\alpha} = \frac{\pi AR}{1 + \sqrt{(\pi AR/\mathrm{a}_0)^2 + 1}} \qquad \text{2-6}$$

As shown by Taha *et al.*[18], in his study on developing an aerodynamic model of a flapping wing, $C_{L\alpha}$ can be referred to as the translational lift constant C_t. Increasing the value of AR towards ∞ influences the $C_{L\alpha}$, with output equal to the a_0. Following Ref.[203–205], the relation between the $C_{L\alpha}$ and C_t can be given as

$$C_t = \frac{1}{2} C_{L\alpha} \qquad \text{2-7}$$

Hence, by replacing A with C_t in Eqn. 2-4, the lift coefficient can be formulated to account for the variations in the AR of the wing, expressed as

$$C_L = \frac{1}{2}\left[\frac{\pi AR}{1 + \sqrt{(\pi AR/\mathrm{a}_0)^2 + 1}}\right] \sin 2\alpha \qquad \text{2-8}$$

With the AR being based on one wing; i.e., $AR = R^2/S$, and a_0 is the lift curve slope of the two-dimensional airfoil section; i.e. it is equal to 2π for a flat plate or a very thin cambered shape. Unlike in Berman & Wang[17], this approach allows the determination of the wing lift coefficient to be based on the wing aspect ratio AR, independent of the empirical value of C_t and suitable to be applied for the analysis of insect flight[140] ($10^3 < Re < 10^4$).

For the drag coefficient C_D, it is determined following the expression given below

$$C_D = C_D(0)\cos^2\alpha + C_D(\pi/2)\sin^2\alpha \tag{2-9}$$

where the coefficients of $C_D(0)$ and $C_D(\pi/2)$ are obtained from an analysis of a revolving wing conducted by Usherwood & Ellington[148,201].

CHAPTER 3. METHODOLOGY

In this chapter, a mathematical formulation of the flapping-wing model is presented, to facilitate the quasi-steady aerodynamic prediction of insect flight. This method provides a new approach for improving the predictive simulation of aerodynamic forces on the relative contribution of induced flow effects associated with flapping wing insect flight. The aim is to develop aerodynamic models that account for the wake-induced effects for two different wing configurations (single and tandem).

This chapter is comprised of five main sections detailing the construction of the aerodynamic model for predicting the optimal performance of insect flapping flight. The first section provides the modelling platform of the present aerodynamic model; this includes the formulation for wing geometries' construction, wing kinematics parameterisation, coordinate definitions and transformation of the wing elements, and the evaluation of aerodynamic forces (and power) on each element of the wing. The second section details the method used to assess the instantaneous changes of the induced flow effect (axial and radial induction factors) on each local wing element, for single and tandem wing configurations. The third section provides a verifying and validating procedure for the model. The fourth section specifies a systematic iterative process of optimisation for estimating the optimum wing kinematics of insect flight; this includes the cost function, constraints, working procedure, and sensitivity analyses for the optimised model. Finally, the fifth section specifies the quantification of the flight performance for flapping wing insect flight.

3.1 WING AERODYNAMIC MODEL

The modelling platform of the present aerodynamic model is based on that published Berman & Wang[17] (see Section 2.3.3 for the details). The model is developed and augmented with a design procedure[16] to include the induced flow effects.

3.1.1 Wing Geometry

An elliptical function (tear-drop-shape) is used for the wing shape, following Ref.[96].

$$c(r) = \frac{4\bar{c}}{\pi}\sqrt{1 - \frac{r^2}{R^2}} \qquad \text{3-1}$$

where $\bar{c}$ is the mean chord length of the wing, and r is the distance measured from wing root to wing tip.

In order to achieve the closest analogue to an insect wing, a set of polynomials is used to approximate and represent the outer edge of the real insect wing shapes[206]. This is done by digitizing the digital picture of the real insect wing shape using open- source software called Plot Digitizer, allowing the wing to be presented by a discrete set of points. The data points were used as reference coordinates in identifying the length of each section of the wing chord, at every local position on the wing along the span.

Table 3-1 Mean chord $\bar{c}$ and wing length R of hawk moth and dragonfly wings.

	Hawk moth	Dragonfly	
		Forewing	Hindwing
$\bar{c}\ (mm)$	18.26	5.88	7.68
$R\ (mm)$	51.90	27.85	26.90

For the real wing-shape of hawk moth, a new equation is derived from the analysis of the digital photograph, as shown in Figure 3-1.

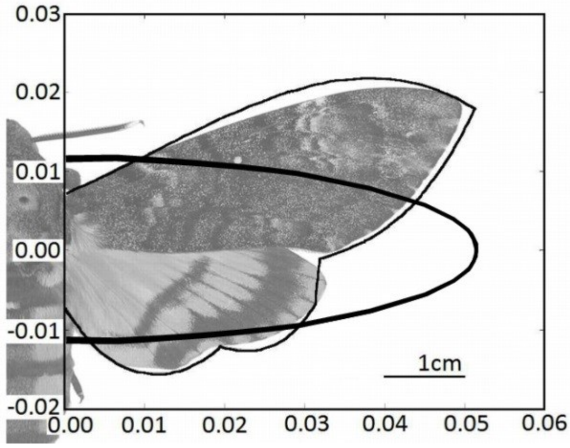

Figure 3-1 Hawk moth wing. The thick solid line represents the wing derived from Eq. 3-1, and the thin solid line represents the wing derived from Eq. 3-2.

$$c(\hat{r}) = a + b\hat{r} + c\hat{r}^2 + d\hat{r}^3 + e\hat{r}^4 \qquad \text{3-2}$$

where $c(\hat{r})$ is the normalized chord, and $\hat{r}$ is the normalized wing span. For the lower part, the polynomial coefficients are grouped into three sections, with coefficients given in Table 3-2. For the upper part, we use constant polynomial coefficients.

Table 3-2 Coefficients of the polynomial Eq. 3-2.

Coefficients	Lower wing			Upper wing
	$0.01 \leq \hat{r} \leq 0.37$	$0.37 \leq \hat{r} \leq 0.61$	$0.61 \leq \hat{r} \leq 1.00$	$0.01 \leq \hat{r} \leq 1.00$
a	-0.2001	-0.6591	-0.7647	0.0558
b	-1.9499	3.4988	3.1200	0.4099
c	7.5672	-10.5598	-5.2961	0.4396
d	-14.2696	9.8870	3.2217	-0.6422
e	15.2123	0.0000	0.0000	0.0000

Similarly, for the real wing-shape of dragonfly, a new set of equation is derived from the analysis of the digital photograph shown in Figure 3-2.

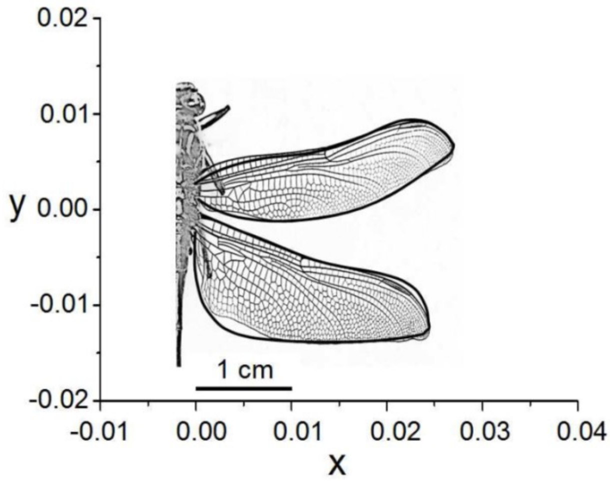

Figure 3-2 Dragonfly wing. The thick solid line represents the wing derived from Eq. 3-3.

$$c(\hat{r}) = a + b\hat{r} + c\hat{r}^2 + d\hat{r}^3 + e\hat{r}^4 + f\hat{r}^5 \quad 3\text{-}3$$

where $c(\hat{r})$ is the normalized chord, and $\hat{r}$ is the normalized wing span. For each of the wings, the polynomial coefficients are divided into two sections, with coefficients given in Table 3-3, representing the upper and lower parts of the fore- and hindwing, respectively.

Table 3-3 Coefficients of the polynomial Eq. 3-3.

Coefficients	Forewing		Hindwing	
	Upper	Lower	Upper	Lower
a	0.0154	-0.0273	0.0321	-0.0144
b	0.4146	-1.0711	-0.0206	-2.6763
c	-0.4984	3.1849	0.9173	7.6848
d	-2.6774	-5.5107	-4.0000	-8.9040
e	6.7850	5.2309	6.8385	4.5981
f	-4.0250	-1.8304	-3.7509	-0.7086

3.1.2 Wing Kinematics

A parameterised kinematics model is used, based upon the availability of kinematic data from prior empirical studies[142,196]. This is used to observe the effects of the wing rotational speed corresponding to the frequency and amplitude of the wing motion in three angular movements (as depicted in Figure 3-3): weaving ϕ (back and forth) in the horizontal plane; flapping θ (up and down) in the vertical plane; pitching η (rotation) about a spanwise axis (axis lies at mid-section of the chord).

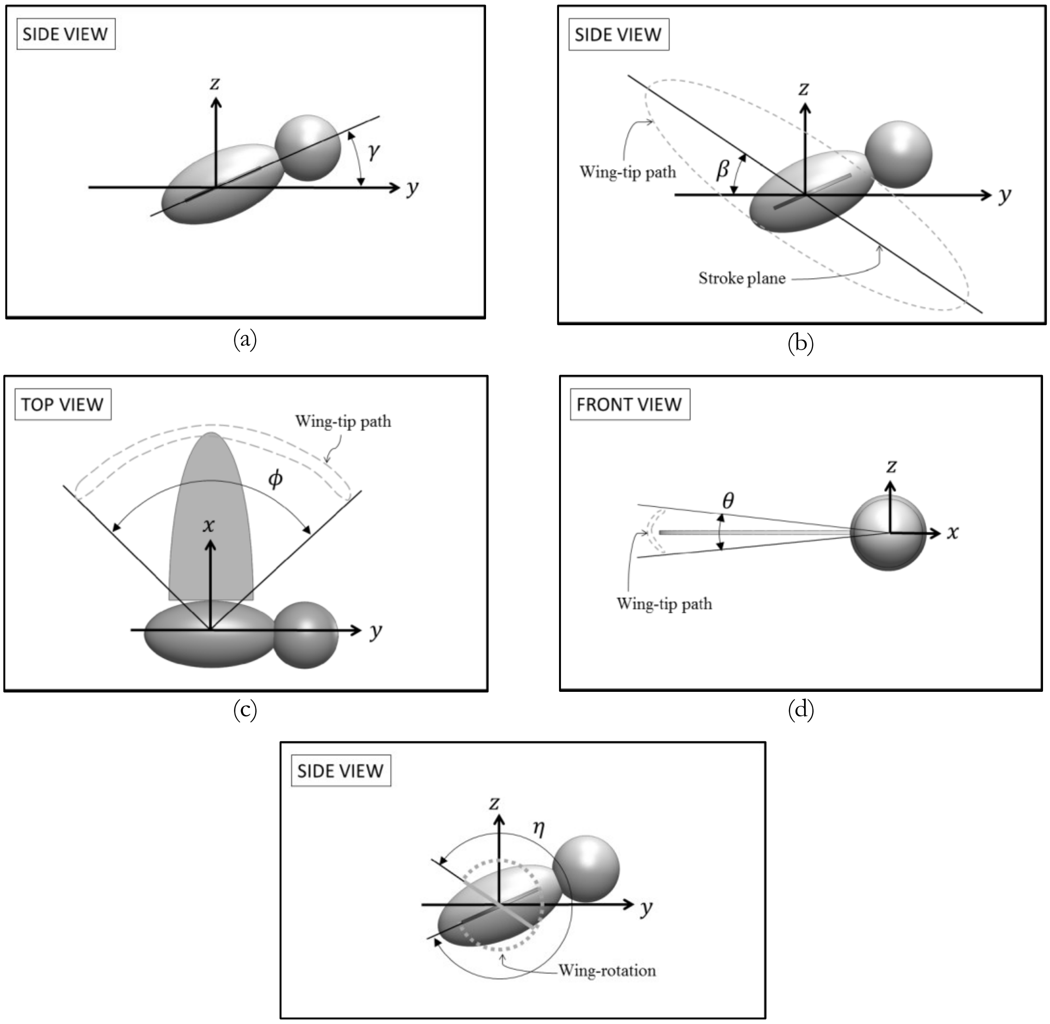

Figure 3-3 Angles for the wing kinematic motion: (a) Wing depicted with the body inclined by an angle, γ, with respect to the earth axes; (b) Wing depicted with the stroke plane inclined by an angle, β, with respect to the earth axes; (c) Wing rotated by the weaving angle, ϕ, with zero body and stroke plane inclination angles; (d) Wing rotated by the flapping angle, θ, with zero body and stroke plane inclination angles; (e) Wing rotated by the pitching angle, η, with the body inclined.

The weaving motion $\phi(t)$ is defined by the equation

$$\phi(t) = \frac{\phi_m}{\sin^{-1}(K)} \sin^{-1}\left[K \sin\left(2\pi f t + \Phi_\phi\right)\right] + \phi_0 \qquad 3\text{-}4$$

The value of K can be viewed as a measure of how rapidly the wing reverses direction; the shape of the function progresses from a sinusoidal to triangular waveform as K increases from $0 < K < 1$, as depicted in Figure 3-4(a). The flapping motion $\theta(t)$ is defined by a sinusoidal equation:

$$\eta(t) = \frac{\eta_m}{\tanh\left(C_\eta\right)} \tanh\left[C_\eta \sin\left(2\pi f t + \Phi_\eta\right)\right] + \eta_0 \qquad 3\text{-}5$$

with $N = 1,2$; $N = 1$ generates an inline vertical motion; $N = 2$ generates a figure-of-eight motion. The pitching motion $\eta(t)$ is defined by the equation

$$\theta(t) = \theta_m \cos(2\pi N f t + \Phi_\theta) + \theta_0 \qquad 3\text{-}6$$

Increasing the value of C_η from 0 to ∞ influences the pitching motion function $\eta(t)$, with output progressing from a sinusoidal function shape to a step function (as depicted in Figure 3-4(b)).

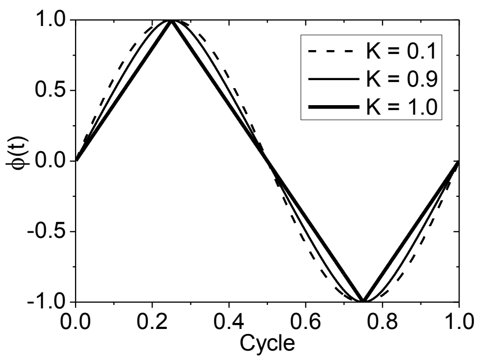

(a) Weaving angle, $\phi(t)$

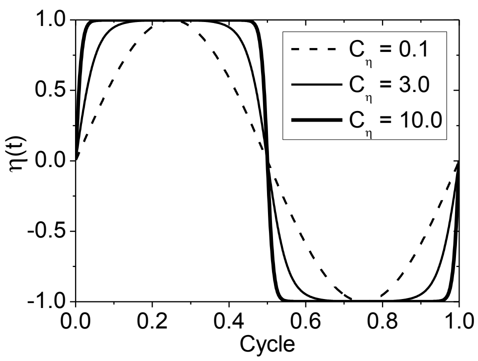

(b) Pitching angle, $\eta(t)$

Figure 3-4 Dependence of $\phi(t)$ and $\eta(t)$ on K and C_η. Angles are shown in radians.

3.1.3 Coordinate Definitions & Transformation

The wing is assumed to move freely as a thin rigid flat plate pinned in space at the root, with the flapping kinematics realized by rotations about a fixed joint. The horizontal plane is assumed to be parallel to the ground, with the z-axis pointing upward, perpendicular to the horizontal plane (free-stream axes). Due to the inclination of the stroke plane and the rotation of the wing, the local wing position from the free-stream or earth axes (subscript $\boldsymbol{e}$) to the blade element axes (subscript η, as shown in Figure 3-5) can be transformed via rotation matrix, given as

$$\boldsymbol{p}_\eta = \boldsymbol{R}_\beta \boldsymbol{R}_\theta \boldsymbol{R}_\phi \boldsymbol{R}_\eta \boldsymbol{p}_e \tag{3-7}$$

where

$$\boldsymbol{R}_\beta = \begin{pmatrix} 1 & 0 & 0 \\ 0 & \cos\beta & \sin\beta \\ 0 & -\sin\beta & \cos\beta \end{pmatrix}, \quad \boldsymbol{R}_\theta = \begin{pmatrix} \cos\theta & 0 & -\sin\theta \\ 0 & 1 & 0 \\ \sin\theta & 0 & \cos\theta \end{pmatrix}$$
$$\boldsymbol{R}_\phi = \begin{pmatrix} \cos\phi & \sin\phi & 0 \\ -\sin\phi & \cos\phi & 0 \\ 0 & 0 & 1 \end{pmatrix}, \quad \boldsymbol{R}_\eta = \begin{pmatrix} 1 & 0 & 0 \\ 0 & \cos\eta & -\sin\eta \\ 0 & \sin\eta & \cos\eta \end{pmatrix} \tag{3-8}$$

The local velocity of the wing element can be evaluated numerically using a finite difference approximation, by evaluating equation Eq. 3-7 at times t and $t + \Delta t$ over a period of a full down- and up-stroke wing motion cycle; via first order forward, Eq. 3-9, central, Eq. 3-10, backward, Eq. 3-11, differencing methods, respectively

$$\mathbf{v}(0) = \frac{\boldsymbol{p}(\Delta t) - \boldsymbol{p}(0)}{\Delta t} \tag{3-9}$$

$$\mathbf{v}(t) = \frac{\boldsymbol{p}(t + \Delta t) - \boldsymbol{p}(t - \Delta t)}{2\Delta t} \tag{3-10}$$

$$\mathbf{v}(T) = \frac{\boldsymbol{p}(\mathrm{T}) - \boldsymbol{p}(T - \Delta t)}{\Delta t} \tag{3-11}$$

The flapping velocity vector of the local wing elements in the free-stream axes, $\boldsymbol{V}_{e,flap}$, is then summed, with the free-stream wind velocity vector, $\boldsymbol{V}$, to obtain the resultant wind velocity vector, $\boldsymbol{V}_e$, at local wing elements in the earth axes:

$$\boldsymbol{V}_e = \boldsymbol{V}_{e,flap} + \boldsymbol{V} \tag{3-12}$$

3.1.4 Aerodynamic Forces & Power

Along with the translation, rotation, viscous, and added mass effects as developed by Berman & Wang[17], the aerodynamic flapping insect flight model presented in this thesis has been expanded to include the induced flow effect (details in Section 3.2).

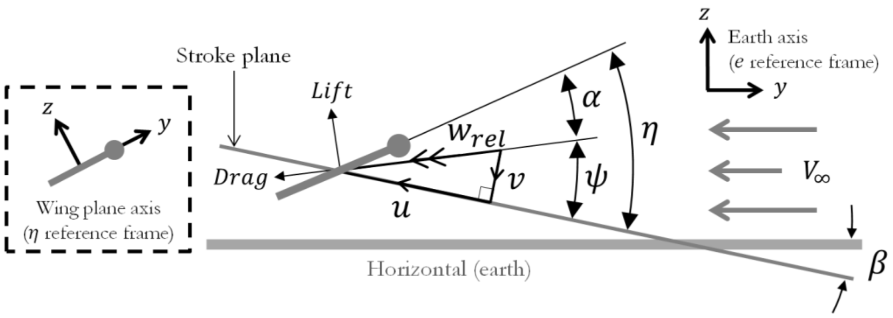

Figure 3-5 Flow geometry for blade element at radial station r

The forces on each element of the wing, with respect to the η reference frame (Figure 3-5), are calculated at 1,000 evenly-spaced time steps over a cycle via numerical integration (details in Section 3.4.3)

$$\boldsymbol{F}_{\eta,aero} = \boldsymbol{F}_C + \boldsymbol{F}_{AM} + \boldsymbol{F}_{Vis} \quad \text{and} \quad \boldsymbol{F}_{\eta,iner} = \boldsymbol{F}_{iner} \tag{3-13}$$

This is a summation of four force components: the wing force due to circulation $\boldsymbol{F}_C$; the wing inertia $\boldsymbol{F}_{iner}$; the added mass $\boldsymbol{F}_{AM}$; and the viscous dissipation $\boldsymbol{F}_{Vis}$. The sub-components for each force are

$$\begin{cases} F_{C,y} = \int_0^R (-\rho v \Gamma)\, dr \\ F_{C,z} = \int_0^R (\rho u \Gamma)\, dr \end{cases} \tag{3-14}$$

$$\begin{cases} F_{iner,y} = \int_0^R \left(\frac{c(r)}{\bar{c}R} m_{wing} \right) v \dot{\eta}\, dr \\ F_{iner,z} = -\int_0^R \left(\frac{c(r)}{\bar{c}R} m_{wing} \right) u \dot{\eta}\, dr \end{cases} \tag{3-15}$$

$$\begin{cases} F_{AM,y} = \int_0^R (m_{22} v\dot{\eta} - m_{11} a_u)\, dr \\ F_{AM,z} = \int_0^R (m_{11} u\dot{\eta} - m_{22} a_v)\, dr \end{cases} \tag{3-16}$$

$$\begin{cases} F_{Vis,y} = -\int_0^R \frac{1}{2}\rho c(r)[C_D(0)\, cos^2\, \alpha + C_D(\pi/2)\, sin^2\, \alpha]\left(\sqrt{u^2+v^2}\right) u\ dr \\ F_{Vis,z} = -\int_0^R \frac{1}{2}\rho c(r)[C_D(0)\, cos^2\, \alpha + C_D(\pi/2)\, sin^2\, \alpha]\left(\sqrt{u^2+v^2}\right) v\ dr \end{cases} \tag{3-17}$$

with the circulation Γ, and the added mass terms m_{11}, m_{22} and I_a defined by

$$\Gamma = -\frac{1}{2}C_t\left(\sqrt{u^2+v^2}\right) sin\, 2\alpha\, c(r) + \frac{1}{2}C_r\dot{\eta}c^2(r) \tag{3-18}$$

$$m_{11} = \tfrac{1}{4}\pi\rho {b_t}^2 \quad \text{and} \quad m_{22} = \tfrac{1}{4}\pi\rho c^2(r) \quad \text{and} \quad I_a = \tfrac{1}{128}\pi\rho\left[c^2(r) + {b_t}^2\right]^2 \tag{3-19}$$

where u and a_u and v and a_v are the y-axis and z-axis local velocity and acceleration components of $\boldsymbol{V}_\eta = \boldsymbol{R}_\eta \boldsymbol{V}_\phi$ and $\boldsymbol{a}_\eta = \boldsymbol{R}_\eta \boldsymbol{a}_\phi$ on the η reference frame, respectively; these all include the induced velocity effect (as in Section 0), except the u and v for the wing inertia in Eq. 3-15. The density of the surrounding fluid is $1.225\ kg/m^3$, and m_{insect} is the mass of the insect. The aerodynamic coefficients of the hawk moth and dragonfly are taken from Berman & Wang[17] and Usherwood & Ellington[201], respectively. The morphological data of hawk moth and dragonfly are given in Appendix A.

Table 3-4 Aerodynamic coefficients of hawk moth and dragonfly

	Hawk moth	Dragonfly	
		Forewing	Hindwing
$C_D(0)$	0.07	0.12	0.14
$C_D(\pi/2)$	3.06	2.71	2.85
C_r	π	π	π

The translational lift constant due to the wing translation C_t is calculated via the Extended Lifting Line Theory as introduced by Schlichting & Truckenbrodt[202], which was adapted by Taha *et al.*[18] for the case of a flapping wing,

$$C_t = \frac{\pi AR}{2\left\{1 + \sqrt{[(\pi AR/2\pi)^2 + 1]}\right\}} \qquad 3\text{-}20$$

The force in the η reference frame, Eqn. 3-13, is transformed back into the e reference frame by multiplying with the inverse matrix of $\boldsymbol{R} = \boldsymbol{R}_\beta \boldsymbol{R}_\theta \boldsymbol{R}_\phi \boldsymbol{R}_\eta$

$$\boldsymbol{F}_{e,aero} = \boldsymbol{R}^{-1}\boldsymbol{F}_{\eta,aero} \quad \text{and} \quad \boldsymbol{F}_{e,iner} = \boldsymbol{R}^{-1}\boldsymbol{F}_{\eta,iner} \qquad 3\text{-}21$$

Thus, the lift to weight ratio L/W can be determined from the z-axis component of $\boldsymbol{F}_e = \boldsymbol{F}_{e,aero} + \boldsymbol{F}_{e,iner}$:

$$\frac{L}{W} = \frac{\mathrm{N}_{wing}\left(F_{e,z}\right)}{m_{insect}g} \qquad 3\text{-}22$$

where N_{wing} is the number of wings, and $g = 9.81\ m/s^2$ is the acceleration due to gravity.

The moments about the wing root due to the aerodynamic and inertia effects are obtained by multiplying the respective forces, Eq. 3-20, with their moment-arms:

$$\begin{cases} M_{x,aero} = \int_0^R \left[F_{e,z}\, r\cos\theta\sin\phi - F_{e,y}\, r\sin\theta\right]_{aero} dr - dM_{ADV} \\ M_{y,aero} = \int_0^R \left[-F_{e,z}\, r\cos\theta\cos\phi + F_{e,x}\, r\sin\theta\right]_{aero} dr \\ M_{z,aero} = \int_0^R \left[-F_{e,x}\, r\cos\theta\sin\phi + F_{e,y}\, r\cos\theta\cos\phi\right]_{aero} dr \end{cases} \qquad 3\text{-}23$$

$$\begin{cases} M_{x,iner} = \int_0^R \left[F_{e,z}\, r\cos\theta\sin\phi - F_{e,y}\, r\sin\theta\right]_{iner} dr \\ M_{y,iner} = \int_0^R \left[-F_{e,z}\, r\cos\theta\cos\phi + F_{e,x}\, r\sin\theta\right]_{iner} dr \\ M_{z,iner} = \int_0^R \left[-F_{e,x}\, r\cos\theta\sin\phi + F_{e,y}\, r\cos\theta\cos\phi\right]_{iner} dr \end{cases} \qquad 3\text{-}24$$

where the wing moment due to added mass and viscosity dM_{ADV} is calculated from

$$dM_{ADV} = \int_0^R \left[(m_{11} - m_{22})uv - I_a\ddot{\eta} - \frac{1}{16}\pi\rho c^4(r)\,(\mu_1 f + \mu_2|\eta|)\,\dot{\eta}\right] dr \qquad 3\text{-}25$$

where μ is the non-dimensional viscous torque[147] ($\mu_1 = \mu_2 = 0.2$). The dM_{ADV} is a function of η, thus it corresponds to the aerodynamic moment in the x direction $M_{x,aero}$.

The power from both wings due to aerodynamic and inertia effects is therefore

$$\begin{cases} P_{aero} = N_{wing} \oint \left| M_x \Omega_\eta + M_y \Omega_\theta + M_z \Omega_\phi \right|_{aero} \\ P_{iner} = N_{wing} \oint \left| M_x \Omega_\eta + M_y \Omega_\theta + M_z \Omega_\phi \right|_{iner} \end{cases} \tag{3-26}$$

where Ω_η, Ω_θ and Ω_ϕ are the angular rotations of the wing in the η, θ and ϕ directions, respectively.

Finally, the total wing power can be calculated as

$$P = P_{aero} + P_{iner} \tag{3-27}$$

3.2 INDUCED FLOW EFFECT

Propellers and flapping wings have been found to operate in similar flow conditions, except for the plunging motion. Following the work by Adkins & Liebeck[16] who proposed a method to correct the momentum loss due to radial flow, the wake-induced effects were modelled with axial and radial induction factors, a and a', respectively.

3.2.1 Induced Velocity for Single Wing

The induction effect along the wing-span is calculated numerically at each time step dt, at each chord-wise local position dr. As shown in Figure 3-5, the effective angle of attack is given by

$$\alpha = \eta - \psi \tag{3-28}$$

The local induced flow angle is given as

$$\psi = \arctan\left(\frac{v}{u}\right) = \arctan\frac{v_z(1+a)}{v_y(1-a')} \tag{3-29}$$

where v_y and v_z are the local velocity components on the ϕ reference frame, calculated from $\boldsymbol{V}_\phi = \boldsymbol{R}_\phi \boldsymbol{R}_\theta \boldsymbol{R}_\beta \boldsymbol{V}_e$. The thrust and the torque-per-unit radius on the wing elements are given as

$$dF = \frac{1}{2}\,\rho\,\mathrm{w}_{rel}{}^2\,c(r)\,C_z\,dr \tag{3-30}$$

$$d\tau = \frac{1}{2}\,\rho\,\mathrm{w}_{rel}{}^2\,c(r)\,C_y\,r\,dr \tag{3-31}$$

where $\mathrm{w}_{rel} = v/\sin\psi = (1+a)\,v_z/\sin\psi$. The horizontal C_y and vertical C_z wing-segment force coefficients are expressed as

$$\begin{cases} C_y = C_L\sin\psi + C_D\cos\psi \\ C_z = C_L\cos\psi - C_D\sin\psi \end{cases} \tag{3-32}$$

As shown by Adkins & Liebeck[16], the airfoil lift and drag coefficients can be determined from the experimental analysis of the two-dimensional airfoil section data. Nevertheless, following the experimental study by Sant[207] on improving BEMT aerodynamic models, it has been concluded that the two-dimensional airfoil data is permissible for the case of low angles of attack. However, for higher angles of attack, the three-dimensional data suited better; this is due to the presence of stall delay, especially at the inboard sections of the propeller blades[207]. Therefore, considering the high angle of attack in insect flight, the corresponding lift and drag coefficients are

$$C_L = \frac{\pi AR}{2\left\{1+\sqrt{[(\pi AR/2\pi)^2+1]}\right\}}\sin 2\alpha \qquad \text{3-33}$$

$$C_D = C_D(0)\cos^2\alpha + C_D(\pi/2)\sin^2\alpha \qquad \text{3-34}$$

From Adkins & Liebeck[16], we get the elements of thrust and torque, respectively:

$$dF = 2\pi r\rho\, v_{sp,z}(1+a)(2v_{sp,z}\, a\, F_m)\, dr \qquad \text{3-35}$$

$$d\tau = 2\pi r\rho\, v_{sp,z}(1+a)(2v_{sp,y}\, a'\, F_m)\, r\, dr \qquad \text{3-36}$$

with

$$F_m = \frac{2}{\pi}\arccos\left\{\exp\left[-\frac{N_{wing}}{2}\frac{(1-r/R)}{\sin\psi_t}\right]\right\} \qquad \text{3-37}$$

$$\psi_t = \arctan\left[\left(\frac{r}{R}\right)\tan\psi\right] \qquad \text{3-38}$$

where F_m is the momentum loss factor for radial fluid flow, ranging from one at the hub to zero at the tip, and ψ_t is the local flow angle at the tip. Combining Eq. 3-30 with Eq. 3-35, and Eq. 3-31 with Eq. 3-36, we get

$$a = \frac{\sigma K_a}{F_m - \sigma K_a} \qquad \text{3-39}$$

$$a' = \frac{\sigma K_{a'}}{F_m + \sigma K_{a'}} \qquad \text{3-40}$$

where the Goldstein momentum loss factors[16] are

$$K_a = \frac{C_z}{4\sin^2\psi} \quad and \quad K_{a'} = \frac{C_y}{4\cos\psi\sin\psi} \tag{3-41}$$

and the local solidity σ is given by

$$\sigma = \frac{N_{wing}c(r)}{2\pi r} \tag{3-42}$$

3.2.2 Induced Velocity for Tandem Wings

With regard to the flow interaction due to the slipstream (induced flow, see Figure 3-6) of the forewing on the hindwing, the aerodynamic model of a single wing is updated.

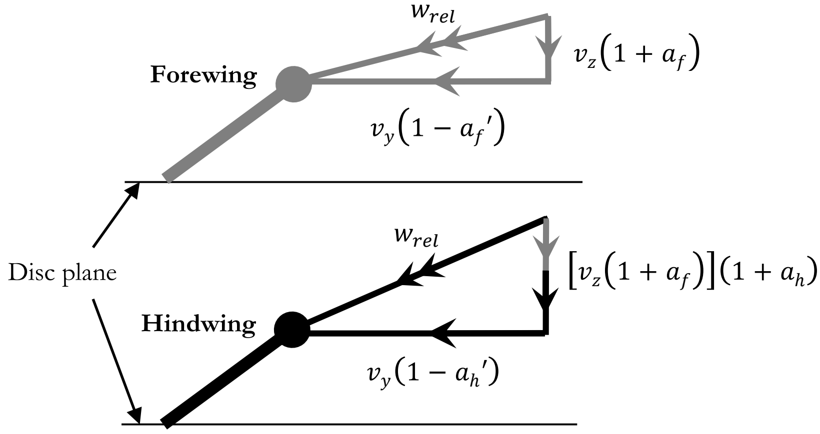

Figure 3-6 Representation of the flow interaction due to the slipstream (induced flow) of the forewing on the hindwing

Two approaches on estimating the local induced flow angle of each wing are given below. For the forewing,

$$\psi = \arctan\left(\frac{v_f}{u_f}\right) = \arctan\frac{v_z(1 + a_f)}{v_y(1 - a'_f)} \tag{3-43}$$

For the hindwing, to account for the streamlined flow of the forewing on the hindwing, the v_z of the hindwing is multiplied by the axial induced flow factor of the forewing

$$\psi = \arctan\left(\frac{v_h}{u_h}\right) = \arctan\frac{[v_z(1 + a_f)](1 + a_h)}{v_y(1 - a'_h)} \tag{3-44}$$

where u and v (of the fore- and hindwing) are the local velocity components on the ϕ reference frame, calculated from $\boldsymbol{V}_\phi = \boldsymbol{R}_\phi \boldsymbol{R}_\theta \boldsymbol{R}_\beta \boldsymbol{V}_e$.

This approach is used in representing the physical concept of the fluid flow interaction in mutual wing interference; in this scenario, the effects of the flow tube of the forewing will extend downstream, entering the sphere of influence (actuator disk) of the hindwing. Therefore, it is assumed that the air approaching the hindwing already has a vertical portion of the forewing velocity in the z direction, normal to the disk plane (or stroke plane). This assumption is analogous to the experimental results of Gravish *et al.*[208], in which the resultant airflow from a pair of wings (in tandem arrangement) working constructively together is higher than the sum of the airflow from the individual contributions of each wing.

3.2.3 Design Procedure

The design procedure is outlined here to provide a clear picture of the sequence of steps involved in determining the induction factors (the flow structure of the integration of this design procedure is given in Appendix B). Here, following the formulations as described in Section 3.2.1 and Section 3.2.2, an iterative process is used to determine the axial- and radial-induced flow factors for each blade element. At the start, it is assumed that $a = a' = 0.01$. The numerical procedure involves a loop with the following sequence of steps:

1. The local induced flow angle ψ is calculated; for single wing (hawk moth), Eq. 3-29; for tandem wings (dragonfly), Eq. 3-43 and Eq. 3-44 for fore- and hindwing, respectively.
2. The local angle of attack α is calculated, Eq. 3-28.
3. The lift coefficient C_L is calculated, Eq. 3-33.
4. The drag coefficient C_D is calculated, Eq. 3-34.
5. The Prandtl momentum loss factor F_m is calculated, Eq. 3-37.
6. The new values of a and a' are calculated using Eq. 3-39 and Eq. 3-40, respectively.
7. Limiters are set to avoid overflow errors, where the new values of a and a' are maintained within bounds between 0.0 to 0.7 (Ref.[16,209]).
8. Tolerance values for a and a' are calculated, $tol_a = |1 - (a_{new}/a)|$ and $tol_{a'} = |1 - (a'_{new}/a')|$, respectively. The tolerance tol is set ≤ 0.001.
9. If the mean tolerance $mean_{tol}$ value for a or a' is ≤ 0.95 and the iterations are $j \leq j_{max}$, continue at step 1 using the new a and a'.
10. If the specified looping condition in the previous step is meet, the loop stops.

The iteration of the induced flow factors is found to be independent of the selection of the initial guest value of a and a'. In summary, the numerical procedure is revealed to be a robust method, which rapidly converges with a minimal number of iterations (< 20).

3.3 MODEL VERIFICATION & VALIDATION

3.3.1 Verification

In order to produce a reliable aerodynamic model, a verification process is needed, so that the accuracy and the consistency of the numerical model and the solution to the model can be measured and retained. For a verification process, there are two important things that need to be addressed, known as the numerical uncertainty and the numerical error[210]. The numerical uncertainty describes the lack of potential that may or may not occur due to a lack of knowledge, and in this case can be determined via a sensitivity analysis that compares different aerodynamic models. The numerical error implies that the deficiency is identifiable upon examination, and can be categorised as acknowledged or un-acknowledged errors (as given in Table 3-5). Unlike the un-acknowledged errors, the acknowledged errors (e.g. discretisation errors) can be identified and have the possibility to be removed or minimised using specific procedures.

Table 3-5 Classification or Taxonomy of Error

Acknowledged Error	Unacknowledged Error
Physical approximation error	Computer programming error
Computer round-off error	Usage error
Iterative convergence error	
Discretization error	

In numerical methods (e.g. via finite-difference, finite-volume or finite-element), one may note that the large number of computations on different sizes of elements commonly yields different results, indicating the existence of discretisation errors. However, these can be resolved by applying the grid convergence studies along with considering the grid refinement factor of the evaluated asymptotic range of convergence[210], since this method is able to address and minimise the discretisation errors. Correspondingly, this gives a guideline in choosing the optimum grid size and time step without sacrificing the amount of computational time in obtaining the desired result.

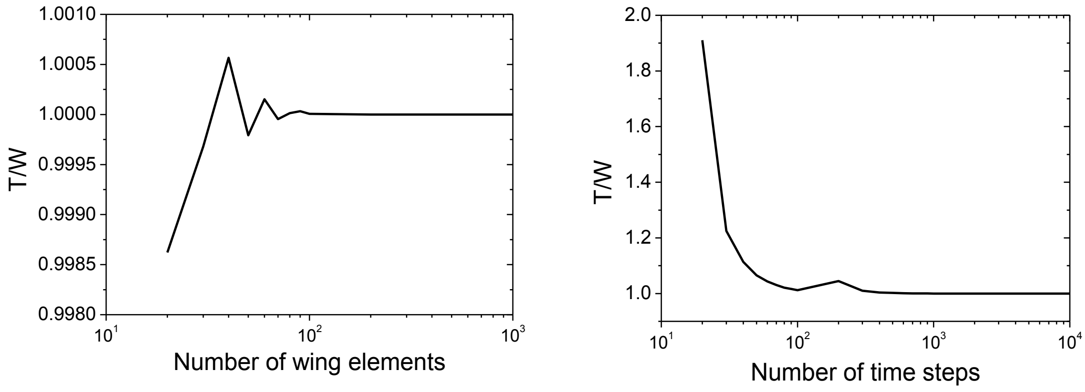

(a) (b)

Figure 3-7 Normalization of $\mathrm{L/W}$ with the number of wing elements (a), and time steps (b) along the span ($\log 10$).

The grid sizes and the number of time steps are varied, as shown in Figure 3-7. It was shown that thrust ratio L/W converges as the number of elements and time steps increase, starting from 100 for the number of wing elements, and $1{,}000$ for the number of time steps. Since the normalized values in both cases converges to one, this is a justification of the appropriateness of the use of the selected grid size and time step[211].

3.3.2 Validation

The results are validated with the numerical studies by Sun & Du[200] for hover flight, and with the experimental results by Ol *et al.*[212] for level flight. The validation is used to determine the degree to which a model is an accurate representation of nature, from the perspective of the intended use of the model[213]. Berman & Wang[17] have shown a good agreement for L/W and P/W in hover flight[163], but made no consideration of forward flight.

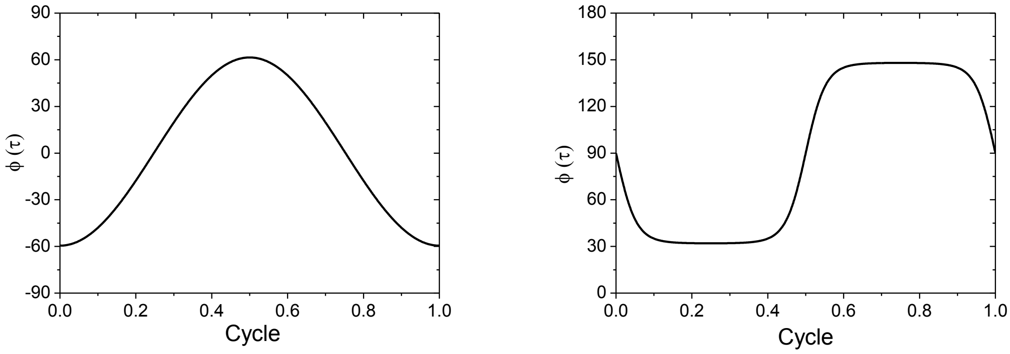

(a) Weaving angle, $\phi(t)$ (b) Pitching angle, $\eta(t)$

Figure 3-8 Variation of the weaving $\phi(t)$ and the pitching angle $\eta(t)$ throughout the cycle, similar to that being used by Sun & Du[200] (i.e. hawk moth).

For hover flight, the same kinematics have been used as Sun & Du[200], Figure 3-8. As indicated in Table 3-6, the results of the present model are comparable.

Table 3-6 Comparison between the computed thrust and power ratios, as well as the mean lift and drag coefficients of Sun & Du[200] and the model of Berman & Wang[17] with the present results for hawk moth. With a weaving amplitude of $\phi_m = 60.5°$, the pitching amplitude of $\eta_m = 32.0°$, and the frequency of $f = 26.3$Hz.

	Sun & Du[200]	**Berman & Wang[17]**	**Present Result**
L/W	1.00	1.10	1.03
P/W (W/kg)	46.00	48.51	47.44
$\bar{C}_L$	1.50	1.68	1.57
$\bar{C}_D$	0.88	0.91	0.87

As for the forward flight, the wing motions are based on the pure-plunge motions of Ol *et al.*[212]. Here, the same weaving amplitude of 0.5 of chord length, relative pitch angle of 8 degrees with respect to the free-stream flow, reduced frequency $k = 0.25$, Reynolds number $Re = 6 \times 10^4$, and Strouhal number $St = 0.08$ are used.

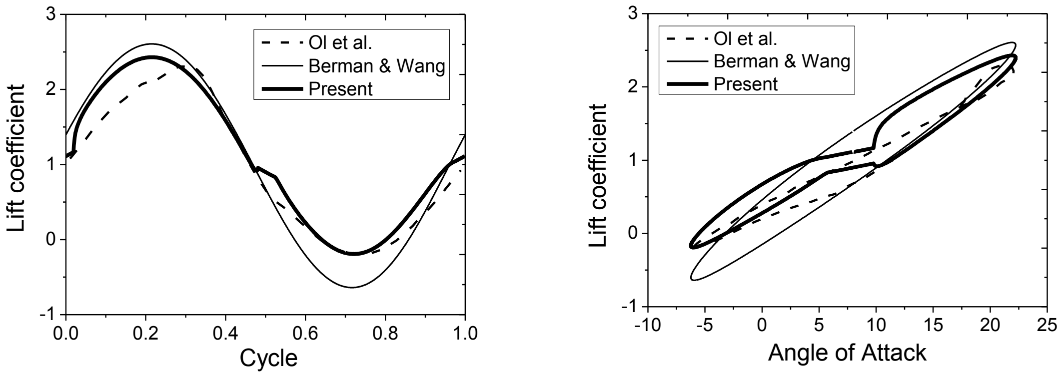

(a) (b)

Figure 3-9 Comparison of the lift of the present model, the experimental results of Ol *et al.*[212], and the quasi-steady model of Berman & Wang[17] for pure–plunge motion with time over a cycle, and with angle of attack (note that the plot for the results of Ol *et al.*[212] are corresponding to the geometrical angle of attack).

Figure 3-9 shows that the calculated lift over the cycle of the model is comparable to the experimental results by Ol *et al.*[212]. Therefore, the model presented can account for the induced flow, and eliminates the dependency on the empirical translation lift coefficient.

Following Glauert[134], those wing whose experienced rapid changes of motion (e.g. sudden descent, rapid perpendicular motion with respect to the direction of the airflow) will experienced what known as vortex ring states. In which, the wing tends to descent into its own downwash; the strength and size of the vortices is increased. The aerodynamic efficiency of the wing is reduced because the drag is increased and the lift is reduced. This may be the reason on why the changes of the lift characteristic (Figure 3-9) at the start and at the end of the stroke. However, it is considered as a special case, since on this validation the wing does only have flapping (up and down, perpendicular with the direction of the airflow) with pitching. For most real cases of insect wing kinematics, the wing do have weaving motion (in the direction of the airflow); that could eradicates such situation of vortex ring states.

Figure 3-10 illustrates the changes of relative velocity and angle of attack for cases with and without induced flow effect over a full cycle. This highlights of how the induced flow effect influences w_{rel} and α, and consequently the lift characteristic (Figure 3-9) during the flapping motion. During the down-stroke, w_{rel} is increased by ~7% (~0.35 m/s) and α is reduced by ~6% (~1 degree). However, during the up-stroke, both w_{rel} and α is reduced by ~2% (~0.1 m/s) and ~14% (~3 degrees), respectively; those percentages are calculated relative to the peak value, without induced flow. Although there is an increase of w_{rel} during the down-stroke, the reduction of α has shown to give greater impact on the lift.

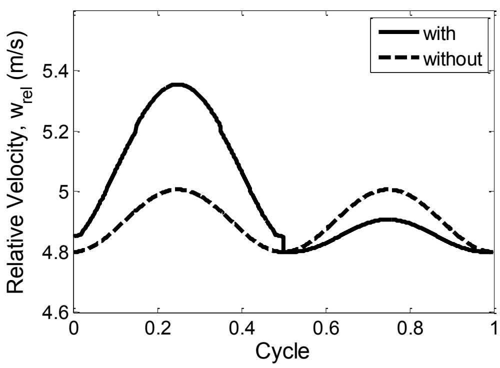

(a)

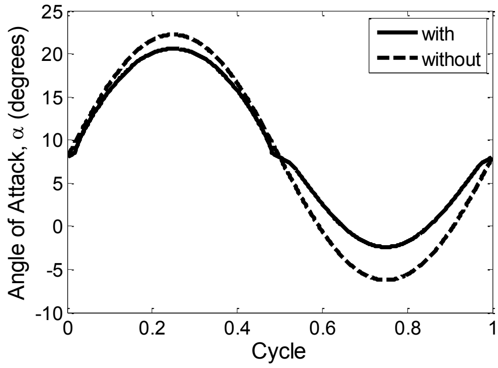

(b)

Figure 3-10 Comparison of relative velocity w_{rel} and angle of attack α for cases with (solid line) and without (dotted line) induced flow effect over a full cycle

3.4 OPTIMISATION

A systematic iterative process-population-based stochastic algorithm called Particle Swarming Optimisation (PSO), developed by Kennedy[15], is used to obtain estimates for optimal wing kinematics. Compared to classical optimisation techniques such as gradient descent and quasi-newton methods, this PSO is simple, efficient and has become one of the most popular optimisation techniques for solving continuous optimisation problems[166]. Moreover, this method does not require assumptions about the problem being optimized, and does not require that optimisation problem to be differentiable, which is advantageous for optimisation problems with very large spaces of candidate solutions that are partially irregular, noisy, and time dependant[167]. A highlight on the mathematical optimisation studies of flapping insect aerodynamic models is given in Section 2.5.

Crucially, an optimisation procedure is needed for replicating the wing motion of an insect in flight, which involves complex three-dimensional motion. This process has proved to be useful in assisting in the search for an optimal realistic wing kinematic motion[17,129], which is subjected with several constraints for stable flight. Therefore, before examining the flight performance of an insect flight, the wing kinematic is optimised. Here, the specified ranges for the optimisation of the kinematic variables are defined following the observational wing kinematics data from experiments on real insects; this will give limits to all kinematic parameters and prevent any physically-unrealistic solutions of the wing motion.

3.4.1 Cost Function & Constraints

The cost function of the optimisation is the propulsive efficiency; with constraints on the flight stability, muscular power ratio, flight muscle ratio, and wing kinematics. This optimisation process is carried out iteratively, with a stopping criterion of up to $1{,}000$ iterations and 10^{-4} tolerance - whichever comes first. The specified range for the optimal model parameters are shown in Table 3-7 and Table 3-8, for hawk moth and dragonfly, respectively.

Table 3-7 Range (or constraint) for the optimal model parameters of hawk moth[142].

Parameter	$V_\infty = 0.00\ m/s$	$V_\infty = 3.00\ m/s$	$V_\infty = 4.00\ m/s$	$V_\infty = 5.00\ m/s$
f	$26.30\ Hz$	$25.00\ Hz$	$22.90\ Hz$	$24.80\ Hz$
β_m	$13.20^0 \rightarrow 17.90^0$	$41.40^0 \rightarrow 43.50^0$	$51.30^0 \rightarrow 52.30^0$	$49.20^0 \rightarrow 53.20^0$
ϕ_m	$59.40^0 \rightarrow 61.80^0$	$51.25^0 \rightarrow 55.15^0$	$49.70^0 \rightarrow 51.75^0$	$49.40^0 \rightarrow 50.45^0$
θ_m	$1.0^0 \rightarrow 20.0^0$	$1.0^0 \rightarrow 20.0^0$	$1.0^0 \rightarrow 20.0^0$	$1.0^0 \rightarrow 20.0^0$
η_m	$1.0^0 \rightarrow 90.0^0$	$1.0^0 \rightarrow 90.0^0$	$1.0^0 \rightarrow 90.0^0$	$1.0^0 \rightarrow 90.0^0$
ϕ_0	$-30.0^0 \rightarrow 30.0^0$	$-30.0^0 \rightarrow 30.0^0$	$-30.0^0 \rightarrow 30.0^0$	$-30.0^0 \rightarrow 30.0^0$
θ_0	$-30.0^0 \rightarrow 30.0^0$	$-30.0^0 \rightarrow 30.0^0$	$-30.0^0 \rightarrow 30.0^0$	$-30.0^0 \rightarrow 30.0^0$
η_0	$-90.0^0 \rightarrow 90.0^0$	$-90.0^0 \rightarrow 90.0^0$	$-90.0^0 \rightarrow 90.0^0$	$-90.0^0 \rightarrow 90.0^0$
Φ_ϕ	90.0^0	90.0^0	90.0^0	90.0^0
Φ_θ	$-180.0^0 \rightarrow 180.0^0$	$-180.0^0 \rightarrow 180.0^0$	$-180.0^0 \rightarrow 180.0^0$	$-180.0^0 \rightarrow 180.0^0$
Φ_η	$-180.0^0 \rightarrow 180.0^0$	$-180.0^0 \rightarrow 180.0^0$	$-180.0^0 \rightarrow 180.0^0$	$-180.0^0 \rightarrow 180.0^0$
K	$0.01 \rightarrow 1.00$	$0.01 \rightarrow 1.00$	$0.01 \rightarrow 1.00$	$0.01 \rightarrow 1.00$
N	$1\ or\ 2$	$1\ or\ 2$	$1\ or\ 2$	$1\ or\ 2$
C_η	$0.01 \rightarrow 5.00$	$0.01 \rightarrow 5.00$	$0.01 \rightarrow 5.00$	$0.01 \rightarrow 5.00$

Table 3-8 Range (or constraint) for the optimal model parameters of dragonfly[196].

Parameter	Forewing	Hindwing
f	$30.0 \rightarrow 45.0\ Hz$	$30.0 \rightarrow 45.0\ Hz$
β_m	$5.0^0 \rightarrow 30.0^0$	$5.0^0 \rightarrow 30.0^0$
ϕ_m	$30.0^0 \rightarrow 60.0^0$	$30.0^0 \rightarrow 60.0^0$
θ_m	$1.0^0 \rightarrow 20.0^0$	$1.0^0 \rightarrow 20.0^0$
η_m	$1.0^0 \rightarrow 90.0^0$	$1.0^0 \rightarrow 90.0^0$
ϕ_0	$-30.0^0 \rightarrow 30.0^0$	$-30.0^0 \rightarrow 30.0^0$
θ_0	$5.0^0 \rightarrow 30.0^0$	$-30.0^0 \rightarrow -5.0^0$
η_0	$-90.0^0 \rightarrow 90.0^0$	$-90.0^0 \rightarrow 90.0^0$
Φ_ϕ	$-180.0^0 \rightarrow 180.0^0$	$-180.0^0 \rightarrow 180.0^0$
Φ_θ	$-180.0^0 \rightarrow 180.0^0$	$-180.0^0 \rightarrow 180.0^0$
Φ_η	$-180.0^0 \rightarrow 180.0^0$	$-180.0^0 \rightarrow 180.0^0$
K	$0.01 \rightarrow 1.00$	$0.01 \rightarrow 1.00$
N	$1\ or\ 2$	$1\ or\ 2$
C_η	$0.01 \rightarrow 5.00$	$0.01 \rightarrow 5.00$

The upper bound value of C_η is set to be at a maximum of 5 (Ref.[214]). This value is based on some studies of the real insects' flight[200,215,216], and is used here to avoid an unrealistically-high rate of wing rotation. Additionally, to comply with the physical power of the real insect, the available power must be limited[103]. Following Ref.[135,136,217,218], the maximum flight muscle ratio m_{muscle}/m_{insect} and the available muscular power ratio P/m_{muscle} can be assumed to be equal to 60% and $150\ W/kg$, respectively. Hence, by equating these two values, the available power P/m_{insect} is estimated to be a maximum of $90\ W/kg$.

3.4.2 Working Procedure

In the optimisation process, a group of particles is selected (10 particles for each optimized parameter), with the particles searching or swarming towards the desired solution simultaneously within a constrained-solution space. Each of the individual particles has a bidirectional link with its neighbours, and is assigned to communicate along the process.

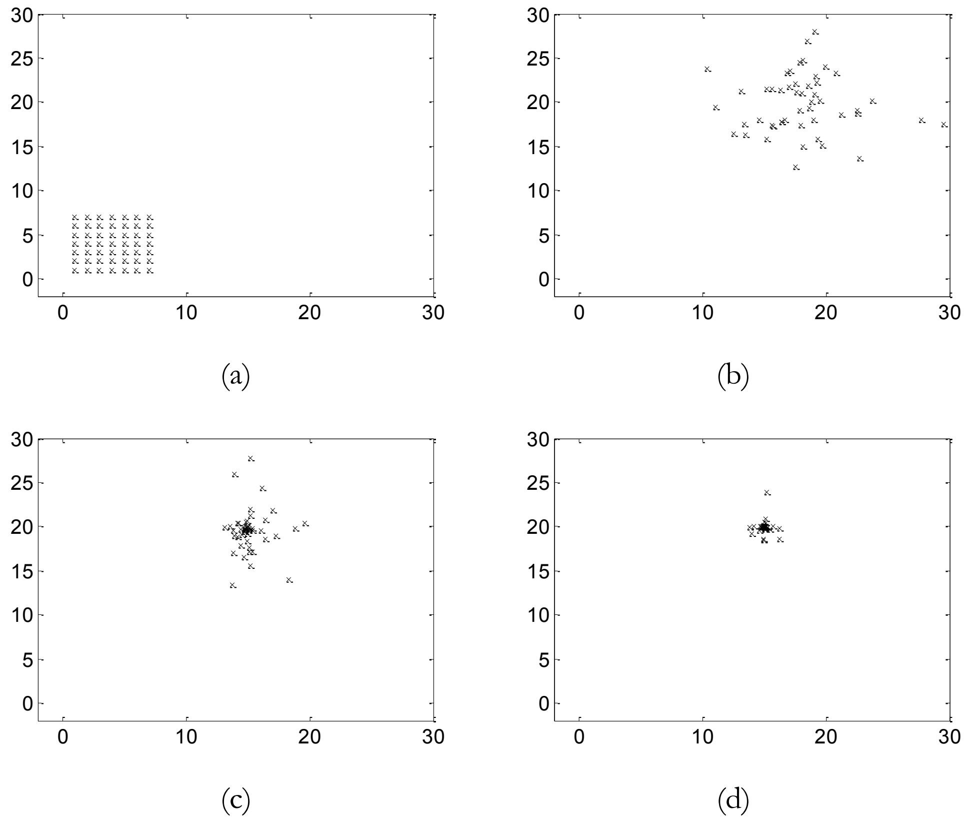

Figure 3-11 Sample of particle swarming movement distribution from PSO analysis; (a) at 1^{st} iteration; (b) at 5^{th} iterations; (c) at 10^{th} iterations; (d) at 20^{th} iterations.

The communication and interactions take place in a way that individual particles will reconfigure their current position (Eqn. 3-46) at each time step, by adding their velocity (Eqn. 3-45) to their previous position. The procedure can be represented by

$$v_{jd}^{(t+1)} \leftarrow \alpha_{pso} v_{jd}^{(t)} + U(0, \beta_{pso})\left(p_{jd} - x_{jd}^{(t)}\right) + U(0, \beta_{pso})\left(p_{qd} - x_{jd}^{(t)}\right) \qquad 3\text{-}45$$

$$x_{jd}^{(t+1)} \leftarrow x_{jd}^{(t)} + v_{jd}^{(t+1)} \qquad 3\text{-}46$$

Where: j is the target particle's index; d is the dimension; x_j is the particle's position; v_j is the velocity; p_j is the best position found so far by j; q is the index of j's best neighbour;

$U(0, \beta_{pso})$ is a uniform random number generator; $\alpha_{pso} = 0.7298$ is the inertia weight or constriction coefficient; and $\beta_{pso} = \psi_{pso}/2$ (where $\psi_{pso} = 2.9922$) is the acceleration constant[219].

The program systematically evaluates each single parameter vector of particle j in the functions ($x_{jd}^{(t+1)}$ and $v_{jd}^{(t+1)}$), and compares the result to the best result obtained by j thus far. Each particle cycles around a region centred on the centroid of the previous best particle's position, and with the best neighbours. If the current result is the best so far, the best position is updated with the current position, and the previous best function result is updated with the current result. As these variables are updated, each particle trajectory shifts to a new region, closer to the optima of the search space, until the desired results from the improved function are obtained (as shown in Figure 3-11). In Figure 3-12, it is shown that the P/W decreases to a minimum as the L/W converges to the constraint unit value.

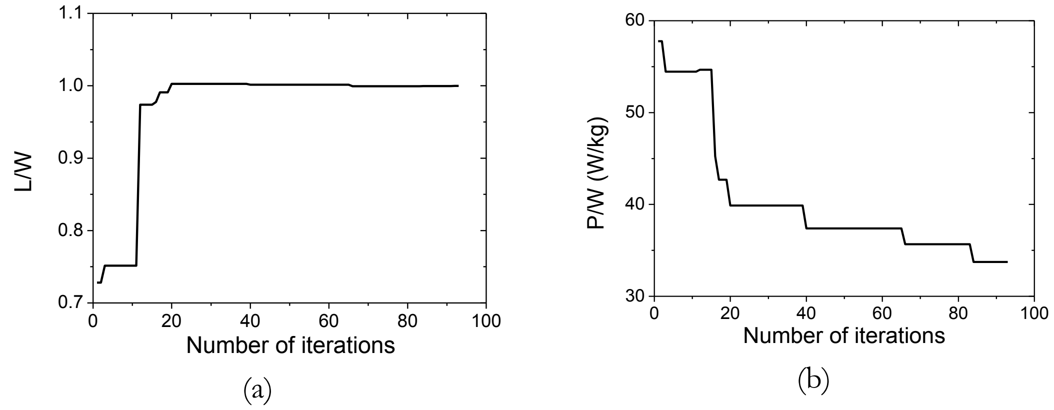

Figure 3-12 Example of L/W and P/W for stroke optimisation.

3.4.3 Sensitivity Analysis

Sensitivity analysis is a systematic reviewing process to assess the uncertainty of a model. Here, two sensitivity analyses are conducted via partial sensitivity analysis, or one-at–a-time[220]. Firstly, the sensitiveness of the aerodynamic model input parameters on the results (total force F and power P) is assessed. Secondly, having determined the sensitive model input parameters, the variations in optimised kinematics are assessed; each of the analyses is performed by changing the value of one parameter from its baseline values (Table 3-9) while maintaining the others as a constant, and evaluating its effect on the results at that time. This approach allows the gauging of the dependability of the solution output on each input parameter, and helps in determining the key parameters that most significantly affect the results. In addition, it would be useful in indicating the consistency of the optimised output kinematics upon the changes of the determined sensitive model input parameters.

Table 3-9 Model input parameters for sensitivity analysis

Wing length	Wing mean chord	Wing mass
R	$\bar{c}$	m_{wing}
$51.9mm$	$18.26mm$	$47mg$
Translational lift coefficient	Drag coefficient at $\alpha = 0^0$	Drag coefficient at $\alpha = 90^0$
C_t	$C_D(0)$	$C_D(\pi/2)$
1.631	0.07	3.06
Rotational lift coefficient	Non-dimensional viscous torque	Non-dimensional viscous torque
C_r	μ_1	μ_2
π	0.2	0.2

The sensitivity analysis of the model input parameters on the results is performed using defined wing kinematics for optimum level flight of the hawk moth at $V = 5\ m/s$ (the wing kinematics are given in Table 4-1). As shown in Figure 3-13, the result indicates that the changes of wing length and wing translational lift coefficient have the greatest influence on both the total force F and power P. This result is logical, since these are the key drivers allied with the total area of the wing aerodynamic surface (R), and the aerodynamic efficiency (C_t) of the wing. A larger wing area (or translational lift coefficient) will translate into generating a greater amount of force, and hence increasing the power required ($P = FV$).

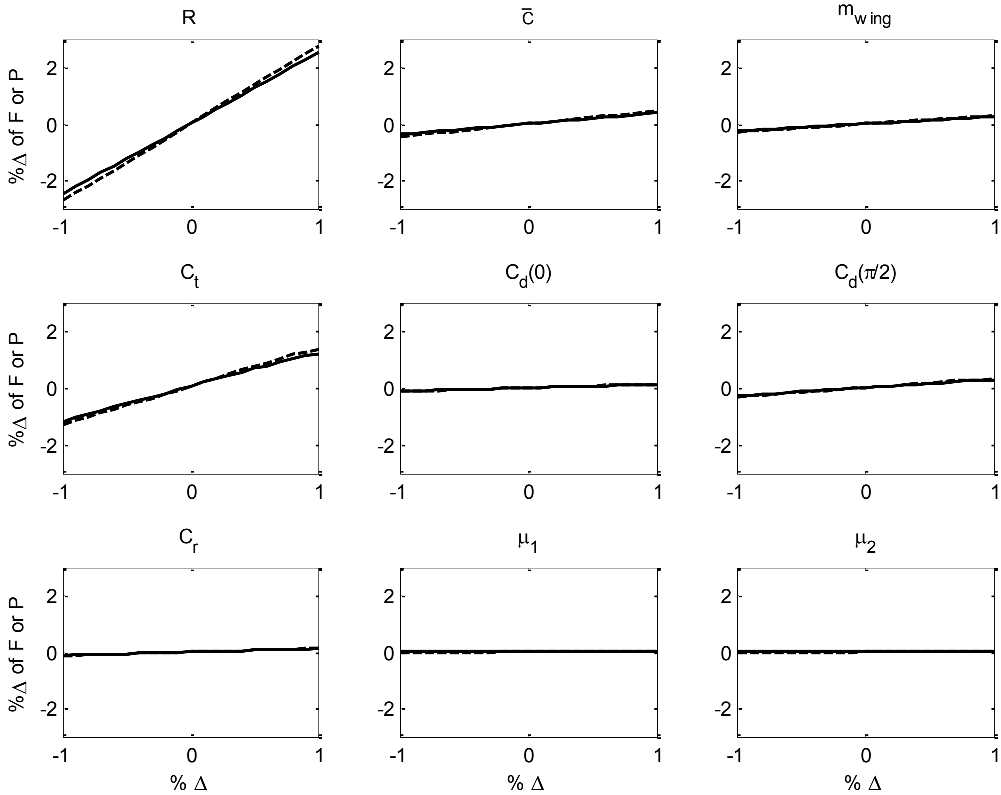

Figure 3-13 Sensitivity screening analysis, showing the variation in total force F (solid line) and power P (dashed line). Force and power are shown as percentages of the baseline values from Table 3-9.

From the sensitivity screening analysis of the model input parameters, it is shown that the wing length and the wing translational lift coefficient are the most sensitive among other inputs. For the next part, the variations in optimised kinematics are measured by performing another sensitivity analysis, following the changes in screened model input parameters (R, C_t). This analysis is intended to measure how the model input parameters will affect the optimised kinematics. In this analysis, the model parameters are increased (or decreased) by 5% and 10% from the base value as given in Table 3-9; this provides an ample range for measuring the variations in the optimised kinematics.

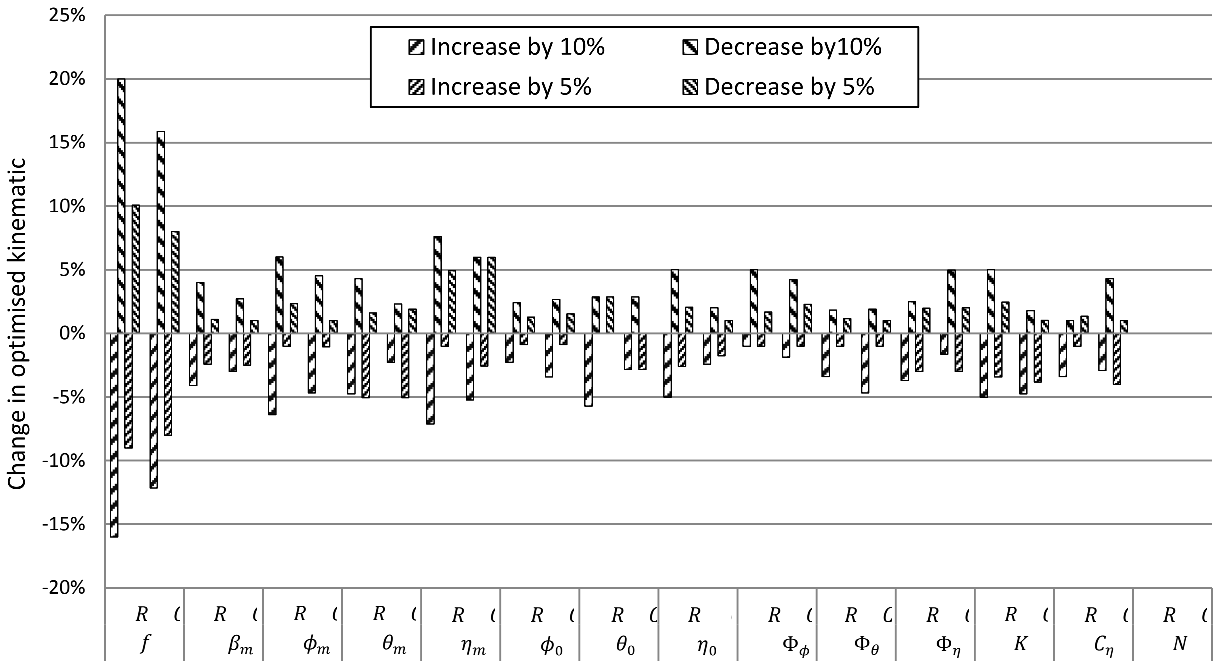

Figure 3-14 Variations in optimised kinematics following the changes in each of the screened model input parameter (R, C_t). Changes in optimised kinematics are shown as percentages of the baseline values from level flight of the hawk moth at $V = 5\ m/s$.

Figure 3-14 shows that an increase in model input parameter (R, C_t) reduces the changes in optimised kinematics, and vice-versa. Overall, the changes in the wing length delivered a greater impact on the optimised model input parameters than the wing translational lift coefficient. The changes in the model input parameters had a noticeable influence on the optimised frequency of the wing. Increasing the value of the model input parameters reducing the power required by up to $\sim 30\%$. This is because an increase in wing size produces wings with a bigger aerodynamic surface area that will benefit from lower flapping frequencies and hence reducing the required power for a specified flight mode[129]. Generally, the results of the two sensitivity analyses (the variations in optimised kinematics and the model input parameters as shown in Figure 3-14 and Figure 3-13, respectively) are screened to be consistent.

3.5 FLIGHT PERFORMANCE

The level flight efficiency η_{level} can be determined from the relationship between the amount of thrust T and power P required,

$$\eta_{level} = \frac{TV}{P} \tag{3-47}$$

where the calculation of thrust and power are described in Section 3.1.4.

In order to simulate vertically accelerating flight, the sum of the vertical force produced from both wings (fore- and hindwing) must be greater than the weight of the insect. Similarly, the horizontal component of the thrust must be greater than the drag in order to accelerate the insect horizontally. The excess vertical and horizontal forces, F_v and F_h, respectively, can be computed from

$$F_v = \left(L_f + L_h\right) - W \tag{3-48}$$

$$F_h = T_f + T_h \tag{3-49}$$

where L_f , L_h and T_f, T_h are the lift and drag forces generated by the fore- and hindwing, respectively. For convenience, the acceleration is presented in terms of g force. The non-dimensional vertical and horizontal specific excess forces are:

$$\bar{F}_v = \frac{F_v}{W} \tag{3-50}$$

$$\bar{F}_h = \frac{F_h}{W} \tag{3-51}$$

Finally, the attainable specific excess forces $\bar{F}_a$ produced can be formulated as

$$\bar{F}_a{}^2 = \bar{F}_v{}^2 + \bar{F}_h{}^2 \tag{3-52}$$

CHAPTER 4. RESULTS & DISCUSSION

Previous chapters dealt with the development of the aerodynamic model of flapping wing insect flight. This chapter provides the results and discussions following the analyses of two insects with having differences in their wing configurations; i.e. hawk moth for single wing and dragonfly for tandem wing. Examining the aerodynamic characteristic of hawk moth in hovering and level flight, and followed by the analysis of dragonfly propulsive characteristics in level and accelerating flight.

4.1 ANALYSIS OF AERODYNAMIC CHARACTERISTICS OF HAWK MOTH FLIGHT

4.1.1 Induced Flow Effect

In generating the forces required to sustain flight, there is a possibility for the wing to be modelled with an unrealistic or impractical motion. Therefore, before examining the induced flow effect, the wing kinematics are optimised. For this, a population-based stochastic algorithm[15] is used to obtain estimates of the optimum kinematic parameters for the wing motion. A set of constraints corresponding to the real insect kinematics as given by Willmott & Ellington[142] is used. This can then allow a comparison between the results of the present model with those in Ref.[135].

Table 4-1 Optimized kinematic parameters for hawk moth.

Parameter	$V = 0.00\ m/s$	$V = 3.00\ m/s$	$V = 4.00\ m/s$	$V = 5.00\ m/s$
f	$26.30\ Hz$	$25.00\ Hz$	$22.90\ Hz$	$24.80\ Hz$
β_m	14.13^0	41.59^0	52.19^0	49.62^0
ϕ_m	61.02^0	52.69^0	50.53^0	49.78^0
θ_m	2.23^0	3.42^0	10.00^0	7.46^0
η_m	57.20^0	43.37^0	21.76^0	14.65^0
ϕ_0	-23.59^0	7.40^0	19.25^0	4.53^0
θ_0	18.41^0	-6.53^0	-17.77^0	0.20^0
η_0	90.00^0	57.35^0	69.77^0	65.56^0
Φ_ϕ	90.00^0	90.00^0	90.00^0	90.00^0
Φ_θ	70.36^0	179.62^0	124.87^0	-106.60^0
Φ_η	180.00^0	-81.98^0	-122.94^0	-147.28^0
K	0.78	0.35	0.39	0.20
N	2	2	2	2
C_η	2.15	0.35	0.36	0.73

As indicated in Table 4-1, the optimized values for the wing kinematics are well within the observed range of those previously measured by Willmott & Ellington[142]. The total power distributions over a cycle, as well as its corresponding components, is presented in Figure 4-2. In Figure 4-1, the plots of the wingtip paths relative to the wing base at four flight speeds are shown.

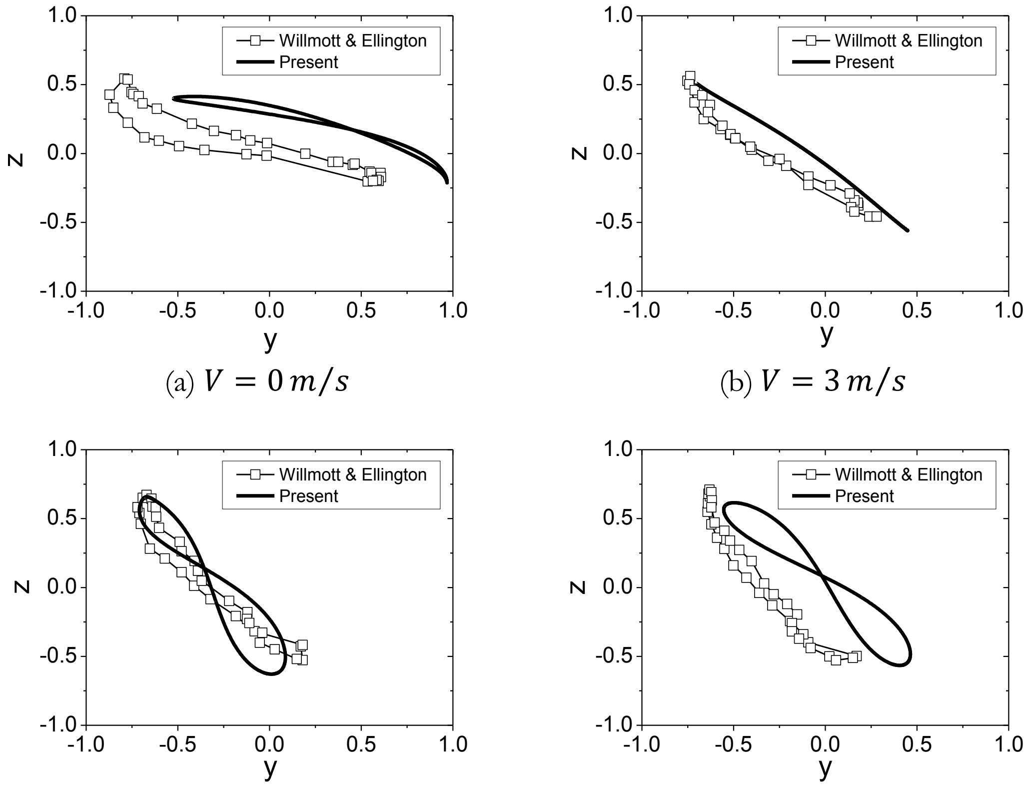

(a) $V = 0\,m/s$ (b) $V = 3\,m/s$

(c) $V = 4\,m/s$ (d) $V = 5\,m/s$

Figure 4-1 Wingtip paths relative to the wing base at four speeds. The square markers are the data from Willmott & Ellington[142]. The axes are normalised to wing length; the stroke plane is inclined at the correct angle to the horizontal.

The results obtained from the present model are compared with the results of Willmott & Ellington[135] - as indicated in Table 4-2, some differences have been observed. It should be noted that some of the critical assumptions and parameters of the two models are different, including the following:

1. Willmott & Ellington[135] assumed that the induced velocity was a constant value and acting vertically (axial) following Stepniewski & Keys[143] for helicopters in forward flight. In the present model the induced velocity is represented by two components of induction factors, as detailed in Section 3.2.1.
2. The lift coefficients were inferred from a dead insect[135], unlike on the present model which is determined via the Extended Lifting Line Theory .
3. As presented by Willmott & Ellington[135], the wing kinematics are determined by fitting to the raw data of the wing positional angles using Fourier series approximations. In this instance, a set of three sinusoidal functions to approximate and replicate the wing motion is used.

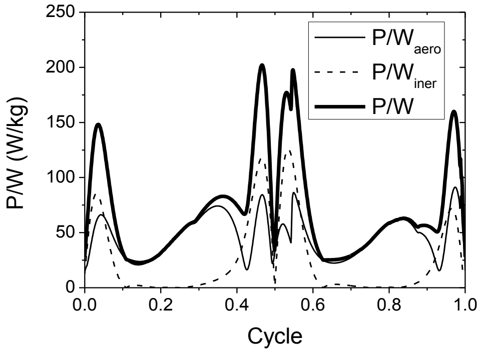

(a) $V = 0\,m/s$

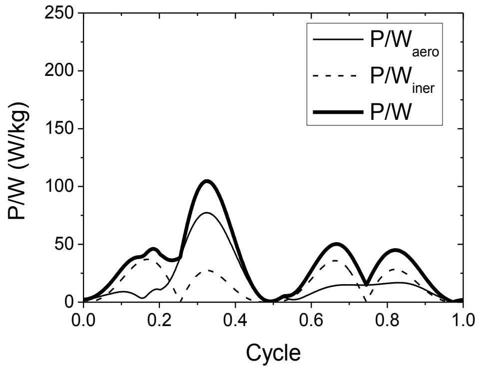

(b) $V = 3\,m/s$

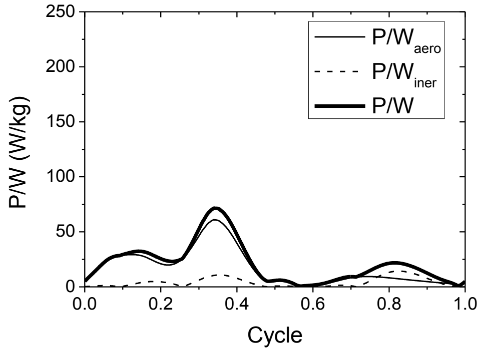

(c) $V = 4\,m/s$

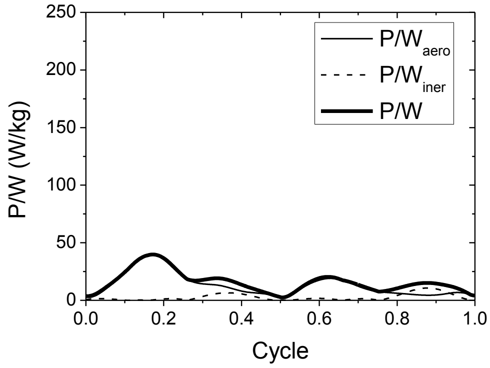

(d) $V = 5\,m/s$

Figure 4-2 Hawk moth: Inertia, aerodynamic, and total power distributions for a complete cycle

Table 4-2 Comparison between computed specific power of Willmott & Ellington[135] and present results

V (m/s)	**Specific Power** (W/kg)	**Willmott & Ellington** [135]	**Present Result**
0.00	P_{iner}/W	37.38	25.34
	P_{aero}/W	17.96	46.69
	P/W	55.34	72.03
3.00	P_{iner}/W	23.16	15.53
	P_{aero}/W	12.52	18.21
	P/W	35.68	33.74
4.00	P_{iner}/W	17.27	4.14
	P_{aero}/W	13.30	16.97
	P/W	30.57	21.11
5.00	P_{iner}/W	20.80	2.70
	P_{aero}/W	20.53	13.15
	P/W	41.33	15.85

Through the inclusion of flow unsteadiness in the induced flow model, the present aerodynamic model offers a better approximation of the insect's flapping wings. Using the same wing kinematics as presented in Table 4-1, an analysis is carried out to investigate these effects on the lift-to-weight ratio $\mathrm{L/W}$ and the power-to-weight ratio $\mathrm{P/W}$; in hovering and level flight.

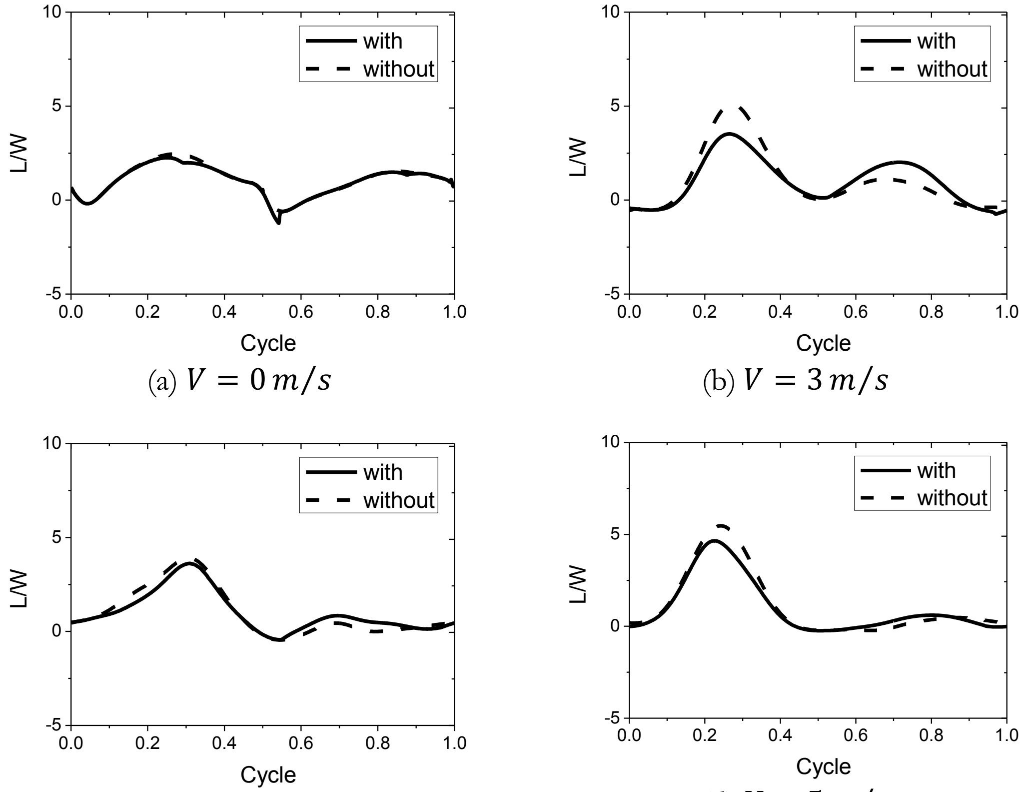

(a) $V = 0\,m/s$ (b) $V = 3\,m/s$

(c) $V = 4\,m/s$ (d) $V = 5\,m/s$

Figure 4-3 Hawk moth: Comparison of lift to weight ratio L/W for cases with (solid line) and without (dotted line) induced flow effect over a full cycle

In Figure 4-3 & Figure 4-4, it is shown that the induced flow effect influences the L/W and the P/W, particularly in the middle of the stroke. For the case of hover (i.e. Figure 4-3(a)), the generated lifting force is almost equal during the up- and down-stroke, even with the presence of an inclined stroke plane. On each of the up- and down-stroke, L/W increases as the wing reaches to the mid point of the stroke.

At the middle stroke point, the wings move at their maximum speed, so they are able to gain the greatest benefit from the airflow to generate the lift force. The lift is proportional to the speed of the relative velocity acting on the wing, thus more lift could be generated if the wings were able to move much faster on each stroke.

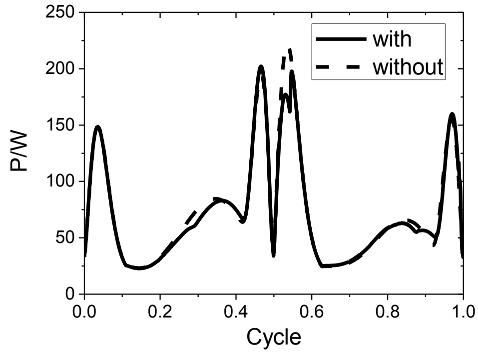

(a) $V = 0\,m/s$

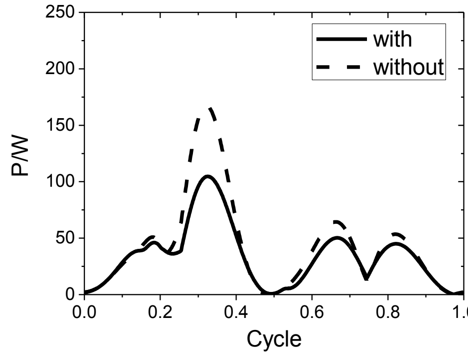

(b) $V = 3\,m/s$

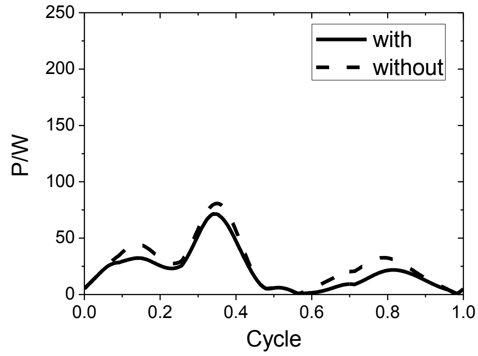

(c) $V = 4\,m/s$

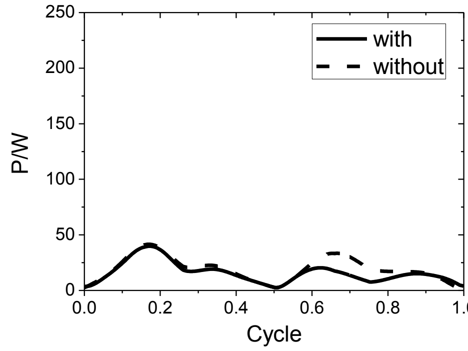

(d) $V = 5\,m/s$

Figure 4-4 Hawk moth: Comparison of power to weight ratio P/W for cases with (solid line) and without (dotted line) induced flow effect over a full cycle

Referring to the cases of forward flight in Figure 4-3, the L/W is found to be higher during the down-stroke than the up-stroke. This is because during the down-stroke, the wing and body are moving in the direction of flight. The oncoming airflow resulting from the body movement is added to the relative velocity acting on the wings. During the up-stroke, the wings move away from the oncoming airflow, thus the relative velocity during the up-stroke that is acting on the wings is lower than the down-stroke flapping motion. Accordingly, this clearly demonstrates that most of the lifting force in insect flapping flight is generated during the down-stroke, which is consistent with the flight of a bird[221]. As in the hover case, the L/W peaks are found to be higher at the mid-point of the stroke.

As shown in Figure 4-4(a) for hover flight, the power P/W is almost the same on each stroke, and peaks are higher at the start and end on each stroke; this is because the amount of inertial power P_{iner}/W needed to move and to stop the wing is highest at this point (see also Figure 4-2(a)). However, in forward flight (Figure 4-4(b-d)) the P/W is higher during the down-stroke, due to the large amount of lift generated during the down-stroke; most of this power is the aerodynamic power P_{aero}/W, as illustrated in Figure 4-2(b-d).

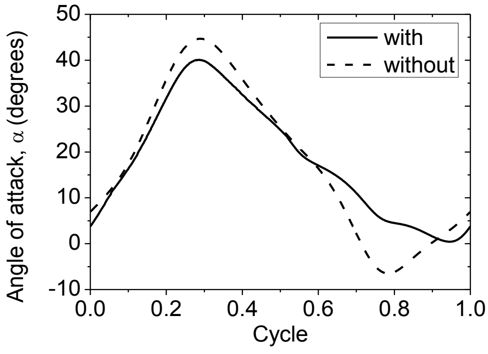

(a)

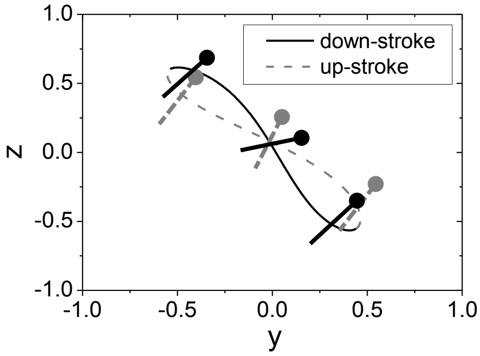

(b)

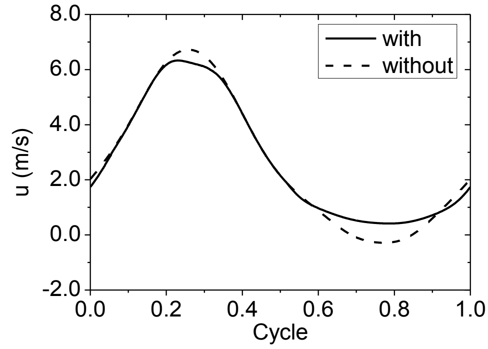

(c)

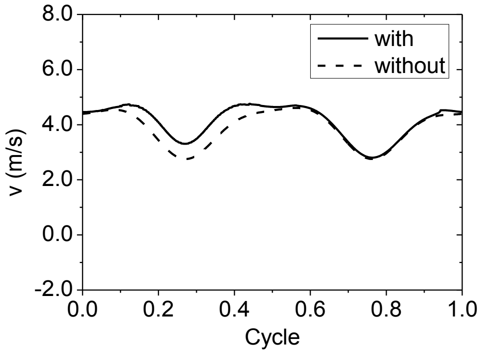

(d)

Figure 4-5 Hawk moth: Angle of attack (a), wingtip path (b), and wing relative velocity component in y-axis (c) and z-axis (d) for case of level forward flight at $V = 5\,m/s$

Figure 4-5 illustrates the changes of the angle of attack, wingtip path for down- and up-stroke, and the velocity components of the wing for level forward flight at $V = 5\,m/s$. This permits scrutiny of how the induced flow effect influences the aerodynamic performance characteristics in flight. As shown in Figure 4-5(c) and Figure 4-5(d), with the presence of the induced flow effect, the relative airflow (velocity component or velocity vector) will be altered - u is reduced (Figure 4-5(c)), while v is increased (Figure 4-5(d)), by ~10% and ~8%, respectively; these average values are calculated relative to case without induced flow. Following these changes, the inflow angle ψ will be present, hence the angle of attack α is reduced[134] (by ~12% on average). As a result, the overall performance characteristics of an insect's flight will be affected, due to the alterations of the prescribed airflow (changes of the velocity component on the wing[16]) resulting from the axial and radial induced flow effects.

Table 4-3 Comparison of the L/W and P/W (W/kg) for cases with and without induced flow effect

V (m/s)	**Induced Flow Effect**	L/W	P_{iner}/W (W/kg)	P_{aero}/W (W/kg)	$\mathbf{P}/W$ (W/kg)
0.00	Without	1.05	25.34	48.27	73.61
	With	1.00	25.34	46.69	72.03
3.00	Without	1.05	15.53	27.91	43.44
	With	1.00	15.53	18.21	33.74
4.00	Without	1.02	4.14	22.57	26.71
	With	1.00	4.14	16.97	21.11
5.00	Without	1.14	2.70	16.72	19.42
	With	1.00	2.70	13.15	15.85

As indicated in Table 4-3, neglecting the presence of the induced flow effect could lead to an over-estimate of the actual lift force L/W and the total power P/W (i.e. aerodynamic power P_{aero}/W). If the induced flow effect is not taken into account, the L/W can be over-estimated by $\sim5\%$ for the case of hover, and by $\sim14\%$ for the case of forward flight. Likewise, the P/W can be over estimated by $\sim2\%$ for the hover case, and by up to $\sim29\%$ for the forward flight case ($V = 3\,\mathrm{m}/s$). In conclusion, this shows that the induced flow effect is important in the modelling of insect flapping flight.

4.1.2 Analysis of Wing Shape

Based on the kinematic parameters of Table 4-1, an investigation on the effect of different wing shapes was carried out to understand how the real insect wing (Figure 3-1) influences the flight performance. The wing shape was approximately drawn using the set of polynomials given by Eq. 3-2 and Table 3-2.

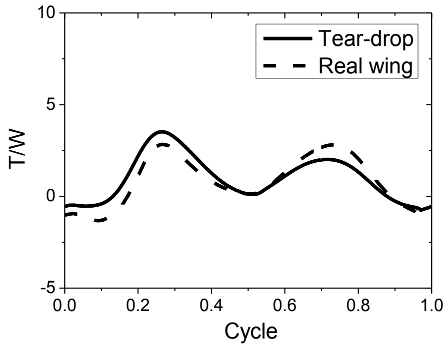

(a) $V = 3\,m/s$

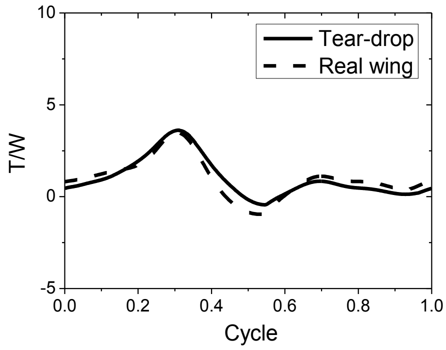

(b) $V = 4\,m/s$

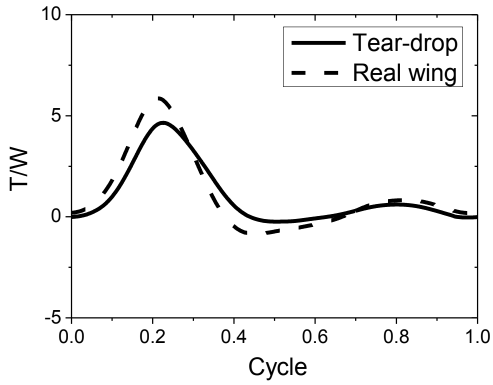

(c) $V = 5\,m/s$

Figure 4-6 Hawk moth: Thrust ratio for cases with tear-drop- (solid line) and real wing shape (dotted line)

In Figure 4-6, it is shown that the real wing produces a higher peak L/W than the tear-drop shape at the middle of stroke, during the up-stroke flapping motion. On the down-stroke, the peak L/W of the real wing increases with the flight speed.

The inertial power P_{iner}/W is not affected by wing shape, as shown in Figure 4-7. There are two peaks of P_{iner}/W on each stroke; the first and the second are responsible for accelerating and decelerating the wing, respectively. The aerodynamic power P_{aero}/W of the two wings is shown in Figure 4-8.

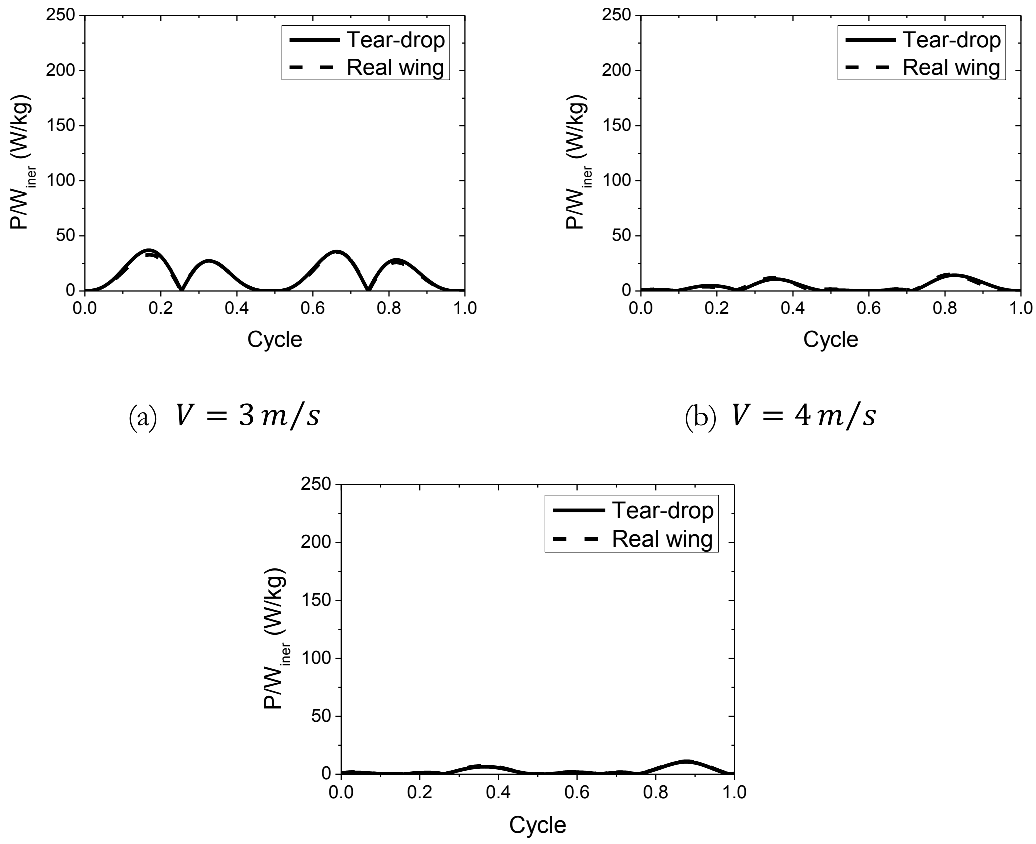

(a) $V = 3\,m/s$

(b) $V = 4\,m/s$

(c) $V = 5\,m/s$

Figure 4-7 Hawk moth: Inertia power for cases with tear-drop- (solid line) and real wing shape (dotted line)

The summary of data - shown in Table 4-4 - indicates that the thrust L/W produced by the real wing is lower than for the tear-drop wing, except for the case at $V = 5\ m/s$, in which the lift force produced by the real wing is $\sim 8\%$ higher. The differences in the P_{iner}/W ratio are up to 11% at $V = 5\ m/s$. The aerodynamic power ratio P_{aero}/W of the real wing is higher in all cases; at $V = 5\ m/s$ the aerodynamic power of the real wing is $\sim 34\%$ higher.

Table 4-4 Hawk moth: Magnitude of L/W, P_{iner}/W and P_{aero}/W, as shown in Figure 4-6, Figure 4-7, and Figure 4-8, respectively

V (m/s)	**Wing Shape**	$\boldsymbol{L/W}$	$\boldsymbol{P_{iner}/W}$ (W/kg)	$\boldsymbol{P_{aero}/W}$ (W/kg)	P/$\boldsymbol{W}$ (W/kg)
3.00	Tear – drop	1.00	15.53	18.21	33.74
	Real wing	0.82	14.63	20.18	34.81
4.00	Tear – drop	1.00	4.14	16.97	21.11
	Real wing	0.98	4.16	17.70	21.86
5.00	Tear – drop	1.00	2.70	13.15	15.85
	Real wing	1.08	2.99	17.57	20.56

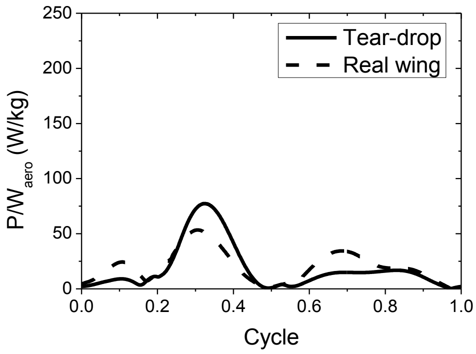

(a) $V = 3\,m/s$

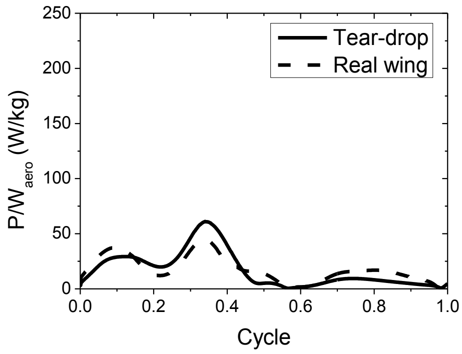

(b) $V = 4\,m/s$

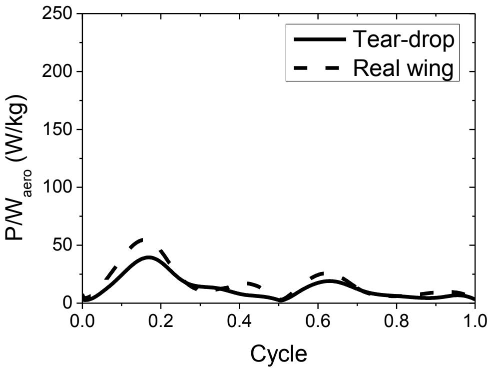

(c) $V = 5\,m/s$

Figure 4-8 Hawk moth: Aerodynamic power for cases with tear-drop- (solid line) and real wing shape (dotted line)

4.2 ANALYSIS OF PROPULSIVE CHARACTERISTICS OF DRAGONFLY FLIGHT

4.2.1 Analysis of Level Flight

The flight speed range is based on the speed of dragonflies observed by Wakeling & Ellington[196], ranging from 0.25 up to $2\ m/s$, with an increment of $0.25\ m/s$.

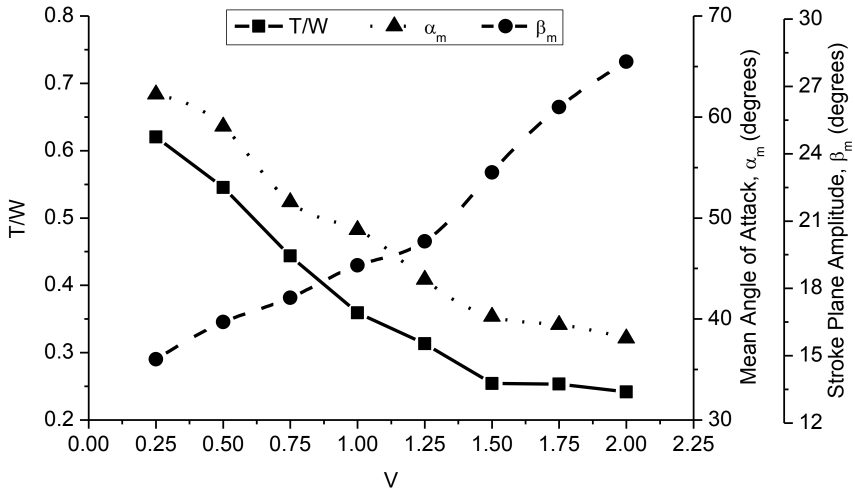

Figure 4-9 Dragonfly: Thrust ratio, mean angle of attack, and stroke plane angle of dragonfly in level flight mode

Figure 4-9 shows the thrust ratio, mean angle of attack and stroke plane angle of dragonfly in level flight mode (the optimisation is applied at each value of V). The mean angle of attack is calculated based on the average value of both wings over a full flapping period. From this figure, it shows that the wing stroke plane angle increases with the flight speed, whilst the thrust and the wing mean angle of attack are reduced; this reduction in thrust is as that indicated by Mazaheri & Ebrahimi[118]. The changes in wing angles are consistent with those measured by Azuma & Watanabe[194] and Wakeling & Ellington[196]. With a lower angle of attack, the amount of thrust required to overcome the drag would be lower.

From Figure 4-10, the power is reduced to a minimum when the flight speed is 1.5 m/s. This is similar to the results presented by May[222] and Azuma & Watanabe[194], who predicted that the minimum power lies at a speed between 1 and 2 m/s. The relationship between the power and the kinematics of the wing could give the best logical correlation in describing the changes in power over the range of flight speeds. The results indicate that the frequency f and the weaving angle ϕ_m at each speed follow the trend of the predicted power.

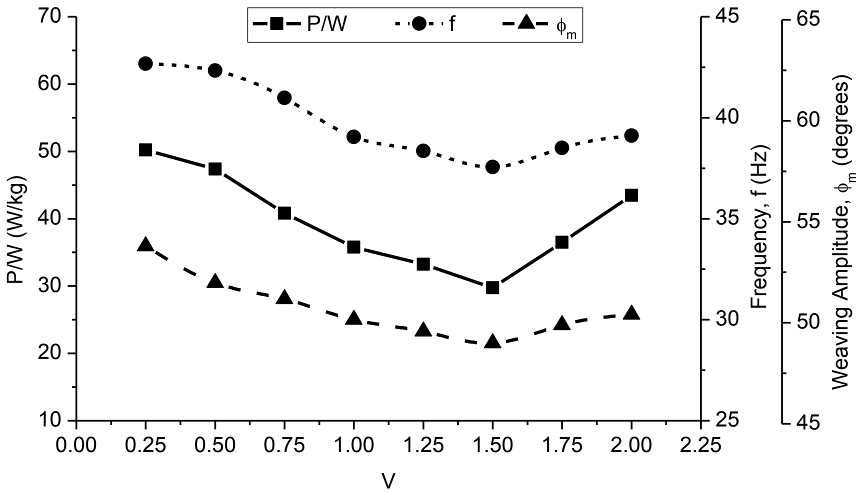

Figure 4-10 Dragonfly: Power ratio, frequency, and weaving angle of dragonfly in level flight mode

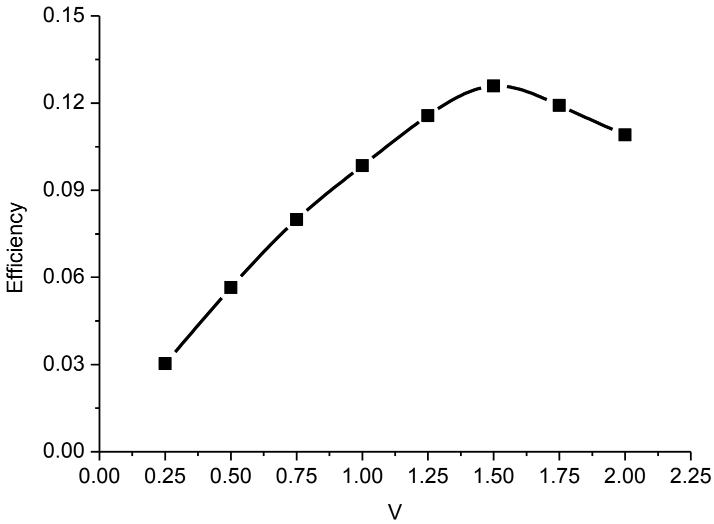

Figure 4-11 Dragonfly: Flight efficiency of dragonfly in level flight mode

As shown in Figure 4-11, the maximum flight efficiency in level flight is predicted to reach 12.7% at $V = 1.5\ m/s$. This is in agreement with the flight muscle efficiency measured by Wakeling & Ellington[136]; these authors provided estimates of $\sim 13\%$ based on measurements of the thoracic temperature elevation and the thermal conductance of the thorax.

4.2.2 Analysis of Accelerating Flight

In this section, an analysis is conducted to predict the dragonfly's maximum acceleration. This is to assess claims (Ref.[195,222,223]) that the dragonfly is able to generate an enormous amount of force that can be used for accelerating in high-speed flight manoeuvres such as take-off or escape. The dragonfly can routinely accelerate with a $3g$ rate to a speed of $10\ m/s$ using its own body muscles[195,222], and is capable of generating instantaneous lift five times greater than its bodyweight[223]. Each of the dragonfly's wings can be actuated independently[192,195]; this allows greater manoeuvrability at a fraction of the energy required by other insects of comparable mass[194]. Marden[217] recorded that the flight-muscle growth of the dragonfly is approximately double its body mass during adult maturation.

It is known that the size of the flight muscle is relative to the size, maturation, and species of the insect[217,224]. Here we simulate the maximum acceleration with flight muscle ranging from 30% to 60%; this equates to a power-to-weight ratio of between $50\ W/k$g and $90\ W/kg$.

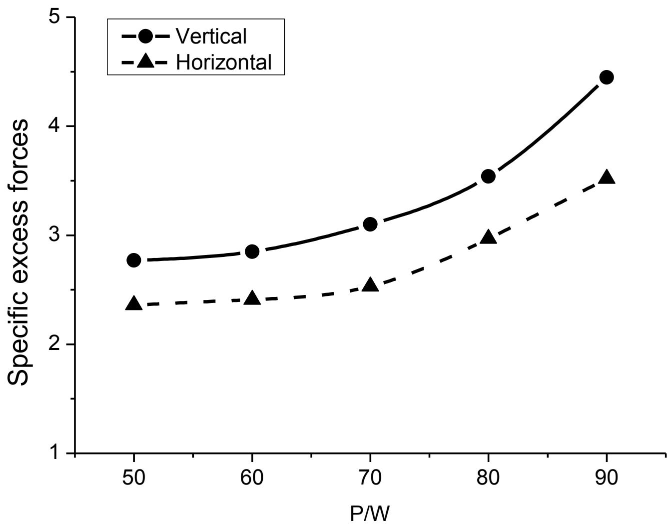

Figure 4-12 Dragonfly: Vertical and horizontal specific excess forces corresponding to available power

Figure 4-12 shows a logical correlation that the vertical and horizontal specific excess forces are increasing with the amount of available power. The vertical specific excess force is 10 to 20% higher than the horizontal specific excess force for a given power-to-weight ratio. The lowest vertical and horizontal specific excess forces are at $P/W = 50\ W/kg$ with F_v~2.7 and F_h~2.4, and reaching the highest value at $P/W = 90\ W/kg$ with F_v~4.4 and F_h~3.5.

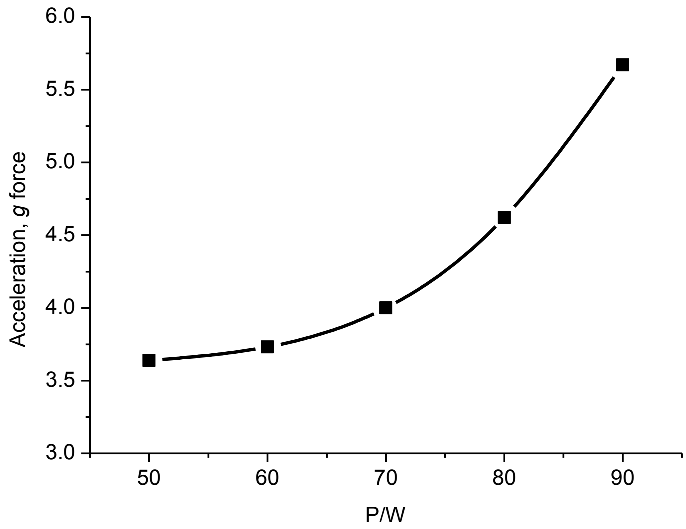

Figure 4-13 Dragonfly: Maximum attainable acceleration corresponding to amount of available power

Figure 4-13 shows that the maximum attainable acceleration increases with the amount of prescribed available power. The predicted g force has a minimum of ~ 3.6 and maximum of ~ 5.6 at $P/W = 50\ W/kg$ and $P/W = 90\ W/kg$, respectively. These values are comparable with measurements reported in the literature[223].

4.2.3 Analysis of Wing Kinematics

An analysis of the wing kinematics for level and accelerating flight modes is shown to validate the model with real insect wing kinematics[192,195,196]. The fore- and hindwing tip paths relative to the wing base for level and accelerating flights are presented in Figure 4-14 and Figure 4-15, respectively.

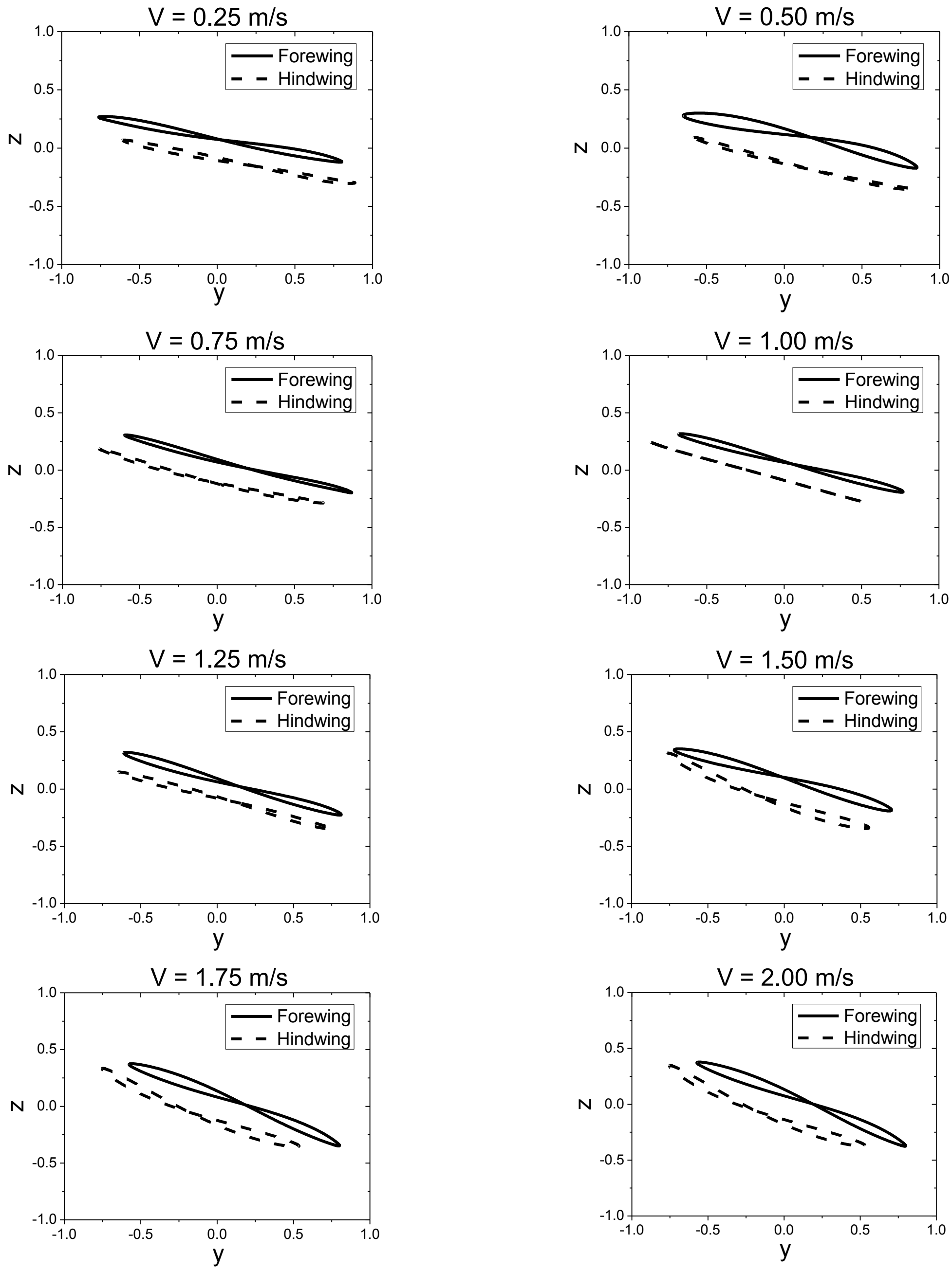

Figure 4-14 Dragonfly: Simulated wingtip paths relative to the wing base for level flight, axes normalized to wing length

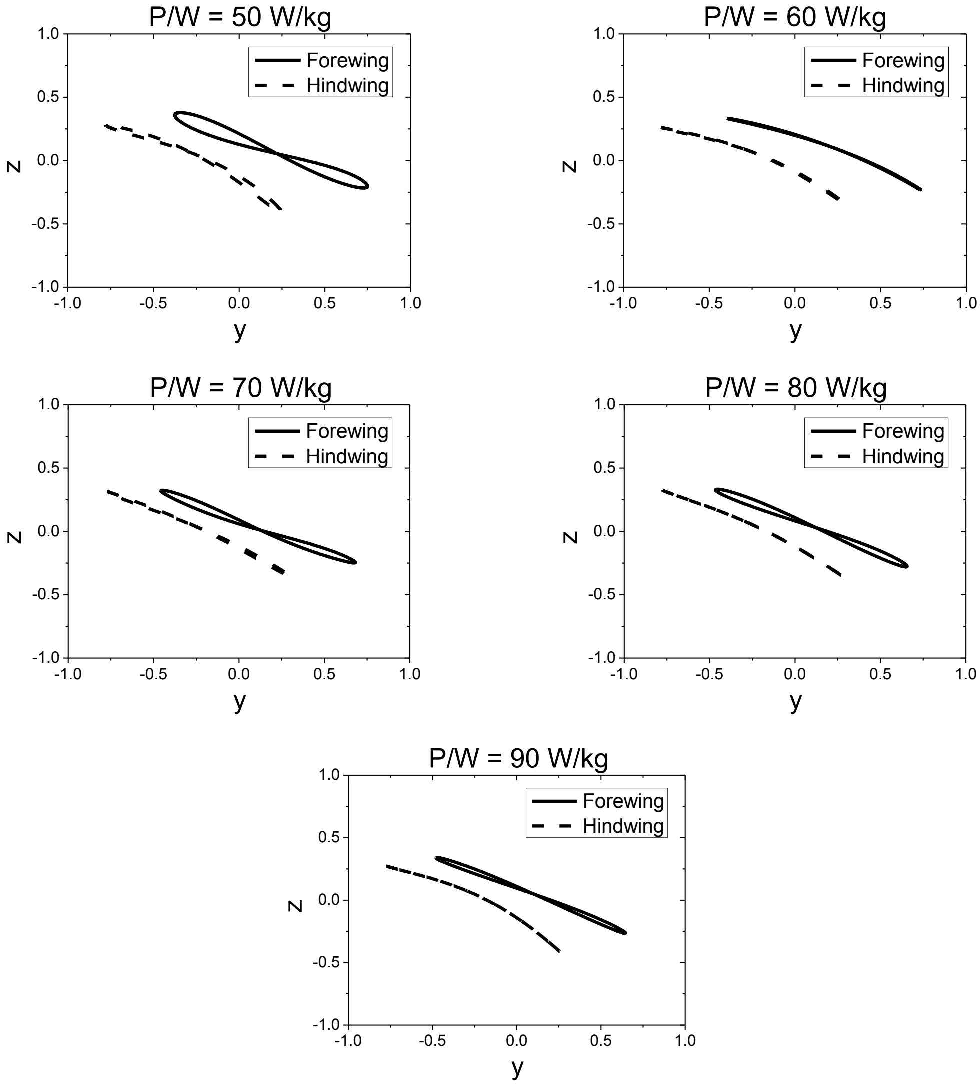

Figure 4-15 Dragonfly: Simulated wingtip paths relative to the wing base for accelerating flight, axes normalized to wing length

Figure 4-16 and Figure 4-17 show the wing kinematics for the two flight modes. In this analysis, the wing kinematics were selected at $V = 1.25\,m/s$ for the level flight and at $P/W = 60\,W/kg$ accelerating flight.

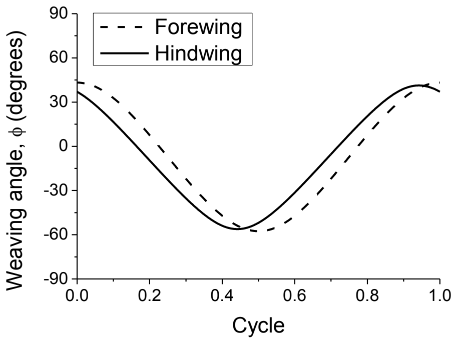

(a) Level flight, $V = 1.25\, m/s$

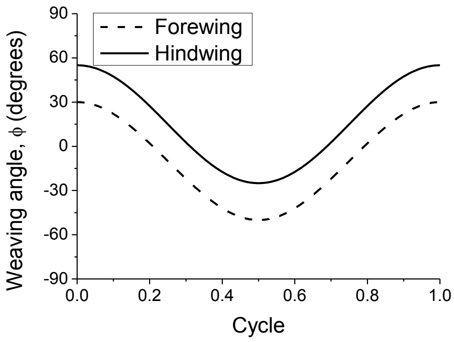

(b) Accelerating flight, $P/W = 60\, W/kg$

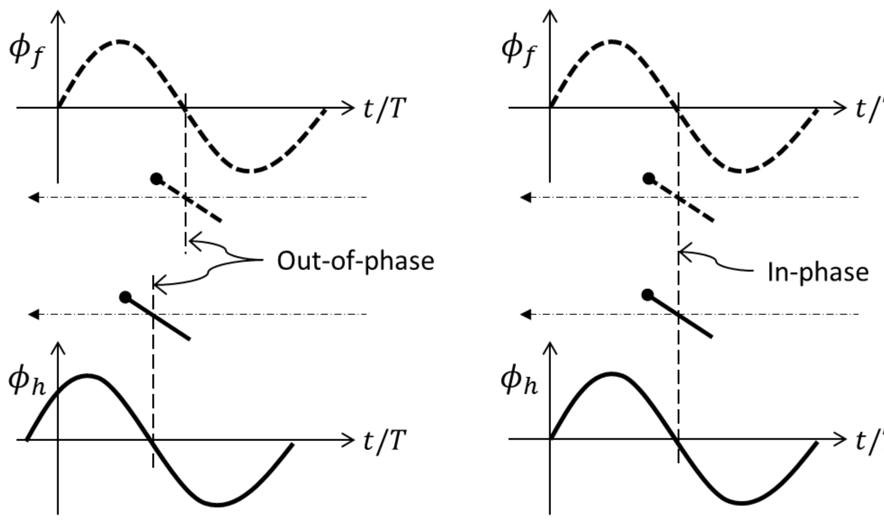

(c) Illustration on the changes of phase pattern. Level flight (left) and accelerating flight (right).

Figure 4-16 Dragonfly: Simulated weaving angle of fore- and hindwing in two flight modes

Figure 4-16(a) indicates that the fore- and hindwing flap out-of-phase in level flight. The largest phase difference is measured at $V = 2\, m/s$, at which point the hindwing leads the forewing by ~ 30 degrees. However, as shown in Figure 4-16(b) for accelerating flight, the wings flap in-phase.

Figure 4-16(c) illustrates the changes in phase for level and accelerating flight modes. These results are in agreement with observations made by Ruppell[195] and Alexander[192], who reported that the dragonfly flaps its wings in-phase to generate higher propulsive forces. Tandem flapping wings have optimal phase patterns, depending on the flight condition, which is also in agreement with the results as presented by Diana[225].

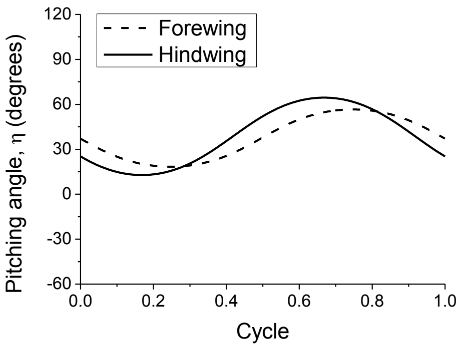

(a) Level flight, $V = 1.25\, m/s$

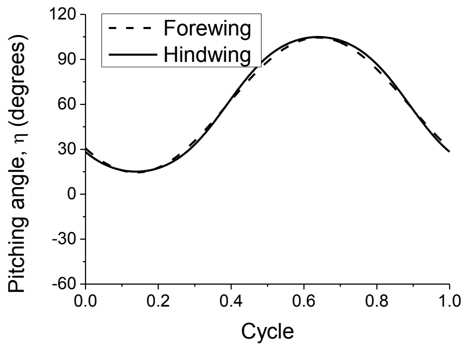

(b) Accelerating flight, $P/W = 60\, W/kg$

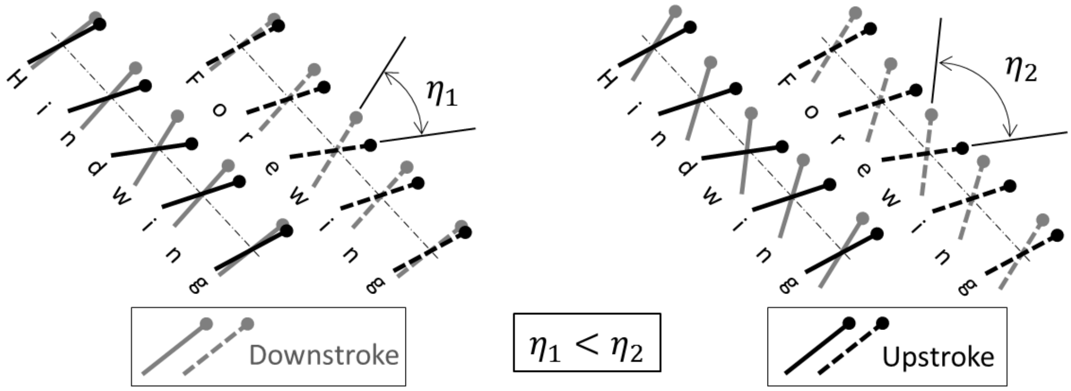

(c) Illustration on the changes of pitching amplitude. Level flight (left) and accelerating flight (right)

Figure 4-17 Dragonfly: Simulated pitching angle of fore- and hindwing in two flight modes

The pitching angles of the fore- and hindwings in the two flight modes are illustrated in Figure 4-17. This figure shows that the magnitude of the pitching angles are different for these two modes, with lower pitching amplitude in level flight (η_1) than in accelerating flight (η_2), as illustrated in Figure 4-17(c). However, the changes of the pitch angle η on each stroke for both flight modes are found to be the same; both start with lower η during the first half-stroke (or down-stroke), $0 < cycle < 0.5$. This is because, during the down-stroke, the wing moves in the direction of the flight and provides higher lift, whereas during the upstroke, the inflow is reduced. In this instance, a larger pitch angle is required to compensate for the reduction of the relative inflow. The changes in angle of attack and the relative velocity during down-stroke and upstroke are illustrated in Figure 4-18. The changes in the wing kinematics (ϕ and η) are in-line with experimental studies[226–228].

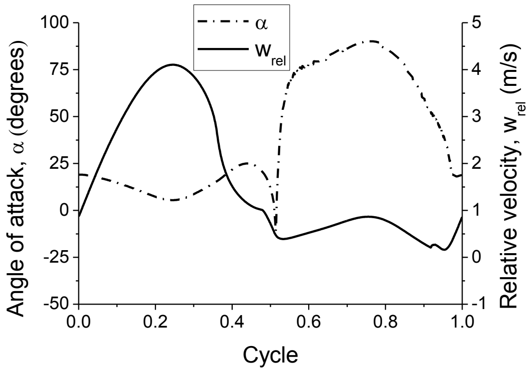

(a) Forewing

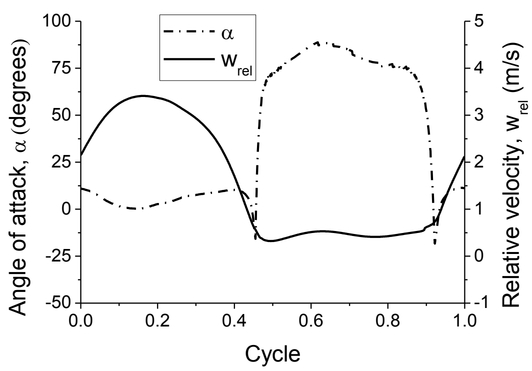

(b) Hindwing

Figure 4-18 Dragonfly: Changes in angle of attack and relative velocity (level flight)

4.2.4 Analysis of Wing Shape

Furthering from the analysis of the tear-drop wing shape, a comparison of flight performance in level and accelerating flight between the tear-drop and real wing of dragonfly is presented; the wings have equal area and wing span. The kinematics of both wings are optimized for maximum propulsive efficiency in level flight, and maximum acceleration for accelerating flight. The tear-drop and real wing shapes are illustrated in Figure 4-19.

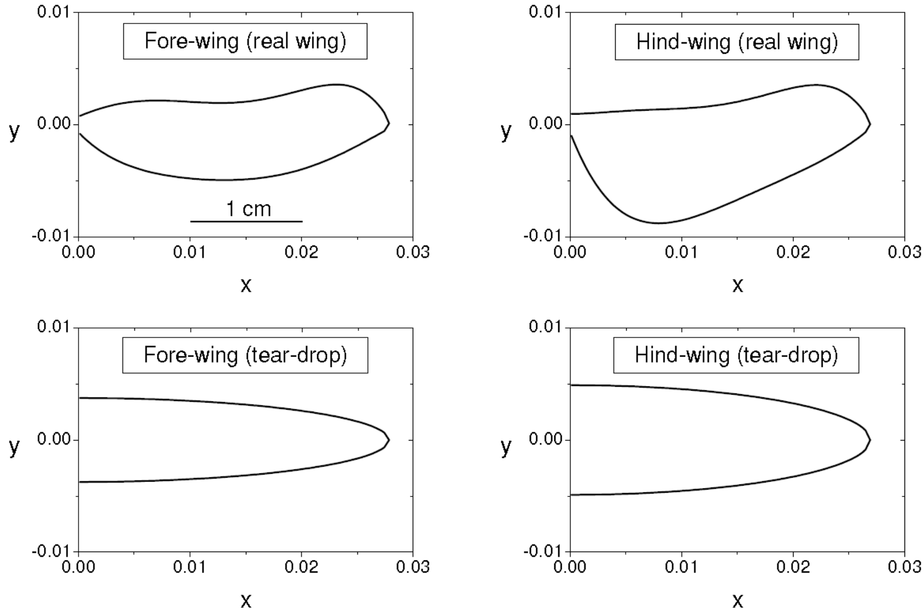

Figure 4-19 Dragonfly: The tear-drop and real wing shapes

Figure 4-20 shows that the level flight efficiency of the real wing shape is higher than the tear-drop wing shape over the range of speeds, with the upper limit increased by up to $\sim 12\%$ at $2.0\ m/s$. The efficiency of the real and the tear-drop wings reaches a peak value at $V = 1.50\ m/s$. The magnitude of acceleration with the real wing is slightly higher than that of the tear-drop wing over the range of available power (Figure 4-21); this is attributed to a larger chord on the mid-section, Figure 4-19.

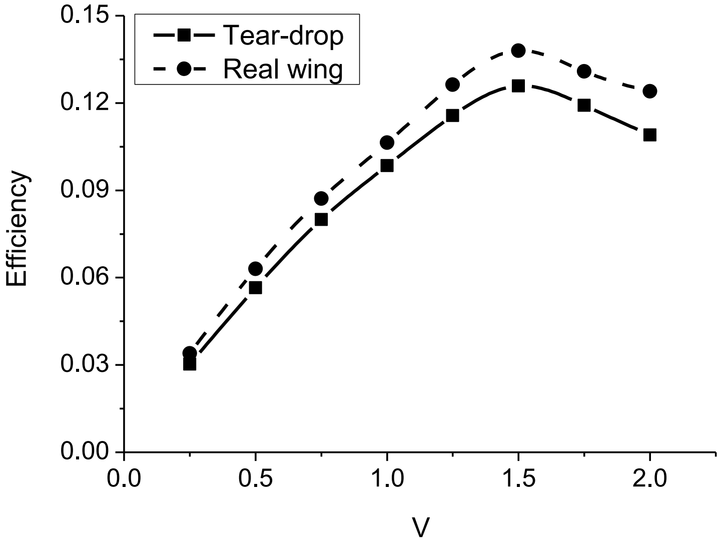

Figure 4-20 Dragonfly: Flight efficiency with two wing shapes.

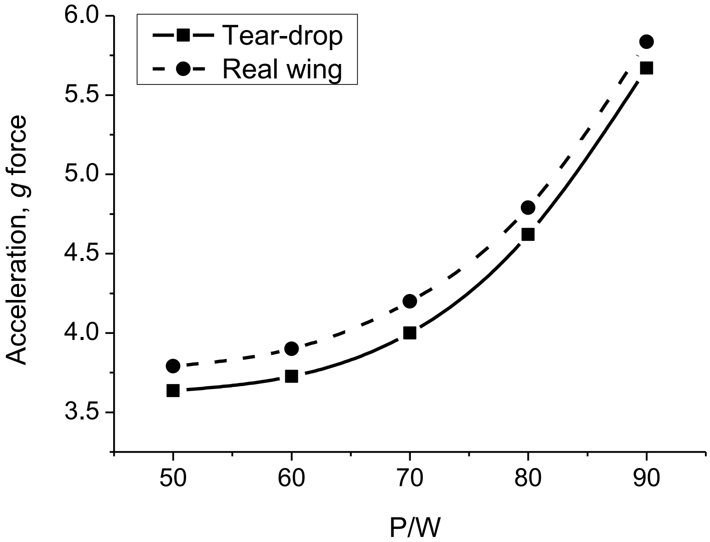

Figure 4-21 Dragonfly: Maximum attainable acceleration with tear-drop and real wing shapes

CHAPTER 5. CONCLUSIONS & RECOMMENDATIONS

This chapter is divided into two main sections. The first section summarises the major findings from the present work. The second section gives directions for future research.

5.1 CONCLUSIONS

This research work presents the development of two aerodynamic models of insect flight. The aerodynamic propulsion models have been developed for single and tandem flapping wings. The work is intended to advance the state of the theoretical tools, making it possible to widen the perspective of nature-inspired flight research methods, allowing the study of the flight performance of an insect-sized vehicle.

The model proposed has been validated against numerical and experimental results for hover and forward flight, respectively. It accounts for the axial- and radial-induced flow effects of the wing; this includes the flow interference between fore- and hind wings for a tandem wing configuration (i.e. dragonfly). Inflow corrections have been introduced in the direction normal to the stroke plane, to account for the fluid flow interaction of mutual wing interference. In addition, the model eliminates the dependency on the empirical translation lift coefficient.

Each of the aerodynamic models is coupled with an independent numerical optimisation capable of handling multiple parameters in disjoint search spaces. Stroke optimisations are demonstrated in cases with 14 and 28 independent parameters for the analyses of single and tandem wings, respectively. Optimisation of the flight parameters is shown to improve the flapping kinematics, and to reduce power consumption in all flight conditions.

For the sake of clarity, the conclusions are presented as a series of statements, which each include a brief discussion to highlight the supporting evidence. Major findings from the present work and the main implications of the results are listed and discussed below:

1. **Aerodynamic power is found to be higher than the inertial power.**
   From the analysis of the hawk moth in hover and level forward flight, the aerodynamic power is found to be higher than the inertial power; this is because the insect is operating at a high angle of attack in order to provide enough force to sustain flight. Flying at a high angle of attack imposes a greater amount of drag on the wing (local wing drag, in the direction of the relative velocity), thus a larger amount of power is required. The inertial power, on the other hand, is not affected by this factor (the high angle of attack); it depends on the mass and kinematics of the wing (frequency and amplitude of all angles involved).

2. **The induced velocity effect is strongest in the middle of the stroke.**
   Formerly, in the modelling of insect flight, the induced flow effect has been assumed to be a constant value, and only acting vertically (axially) on the stroke plane; it enables the prediction of how much the induced flow effect would cost for each prescribed flight. This approach is limited, in that it is unable to justify the actual physics of the flow, since it does not consider the momentum loses due to the radial flow, and is unable to produce comprehensive histories due to the rapid changes of the induced flow during flapping.

   Regarding the issues discussed above, the present model is designed to consider and assess the instantaneous changes of the induced flow effect on each local wing element (the axial and radial flow components). The result has shown that this effect is strongest in the middle of the stroke, and all these effects have significant influence on the thrust and the power. By neglecting the presence of the induced flow effect, the net force and propulsive power may be overestimated. At this point, the magnitude of the velocity component that contributes to intensify the induced flow angle is higher (see mathematical formulation in Section 3.2 for further details).

3. **The changes in thrust and power at each flight speed can be correlated with the changes of the wing kinematics.**
   In the present work, the changes in thrust and power are coherent with the changes of the wing kinematics. As the flight speed is increased (level flight), the amount of thrust is reduced; this is due to the reduction in the angle of attack, which minimises the amount of drag (or thrust required) to be encountered by the wing.

   For power, the trend follows the changes of the wing kinematics; it has indicated that the power reaches its lowest level when the frequency and weaving amplitude is its minimum value (i.e. level flight at 1.5 m/s). These two kinematic parameters are the main drivers in determining the wing speed and the size of the area covered by the wing during flapping motion. Faster wing speeds require more power, due to the fact that power is a product of the angular velocity of the wing (as given in Eq. 3-26). Similarly, for a larger area covered by the wing, more power is required than for the lesser area.

   This can be seen through comparison at two different wing speeds (frequency). For wing frequency of ~37 Hz the power required is around 30 W/kg. Whereas for higher wing speed (frequency of ~39 Hz), the power required is higher, which is above 40 W/kg,

4. **Maximum attainable acceleration is found to increase with the size of the flight muscle.**
Insects used their flight muscles to drive the wing mechanism, powering the kinematic motion of the wing for flying. For conventional aerodynamic machines such as fixed- and rotary wing aircraft, the flight performance can be measured based on the power-to-weight ratio. This is similar to the case of an insect, in which the size of the flight muscle is one of the key elements in determining its ability to perform the high-performance flight.

   Following the analysis of dragonfly flight, the results have indicated that the changes in power at each flight speed can be correlated with the changes of the wing kinematics. The predicted level flight efficiency is in agreement with the experimental results of flight muscle efficiency. The maximum attainable acceleration is found to increase with the size of the flight muscle (or power available); this is primarily due to the accessibility of the power available to propel the wing. Therefore, the size of the flight muscle will reflect the biomechanical limitations on the available power for an insect to achieve a high rate of acceleration in flight.

   A comparison between insects with different size of flight muscle can clearly shows the differences. For instance, insect with 60% of flight muscle is able to accelerate 50% much faster than the insect with 30% of flight muscle.

5. **Wings will flap out-of-phase to fly efficiently in level flight, and flap in-phase to obtain maximum forces in accelerating flight.**
Through the analysis of the wing kinematics of the dragonfly, it is shown that the wings will flap out-of-phase to fly efficiently in level flight. However, to obtain maximum acceleration, the wings flap in-phase. In level flight, the forward motion of the insect helps to increase the velocity vector acting on the wing, which consequently reduces the induced flow effect (the value of ψ is reduced when $u \gg v$). This helps the insect to fly efficiently, minimising the power required while acquiring enough forces to sustain its own weight and to overcome the drag due to the forward movement of the insect.

   In accelerating flight, the in-phase motion of both wings creates a single wing with a larger aerodynamic surface area. This enables them to generate much greater force compared to working as two independent separate single wings, as commonly found in level flight. In-phase motion permits both wings to move together, avoiding them moving in opposite directions (counter-stroking for some period during the flapping cycle), which causes the force produced by the wings to oppose each other. This result is in agreement with observations of dragonflies in nature.

6. **Real wing shape has better propulsive efficiency and acceleration than the tear-drop wing.**
The proportion of the wing area between the tear-drop and real wing shape is different (as illustrated in Figure 4-19). For tear-drop shape, the wing has a larger surface area much closer to the root, which gets narrower towards the end or the tip of the wing. For a real wing shape, the majority of the wing area concentrated in the middle or inner part of the wing; it has less surface area on the outer part (closer to the root and tip) of the wing.

   In flight, the wing is flapping and the distribution of velocity acting on each local wing element is varied. The variation of velocity is dependent on the distance of the wing element, measured from the root of the wing. Wing elements closer to the wing tip will have a much higher velocity; this is because, for the same angular velocity, the outer part of the wing will travel a much greater distance compared to its inner part. On the inner part of the wing (closer to the wing root), the velocity is very small.

   The force generated by the flapping wing depends on the size of the local wing element (chord length) and velocity acting the wing. Therefore, by looking at these two factors, it is clearly demonstrated why the real wing shape is superior to the tear-drop wing. The proportion of wing area plays a big role in optimal flight, producing wings with better propulsive efficiency and acceleration.

7. **Real wing demands more aerodynamic power than the tear-drop wing.**
The analysis with two different wing shapes shows that the wing shape can influence the performance of insect flight. It is found that the real wing demands more aerodynamic power than the tear-drop wing.

   Note that, despite the fact that the real wing is superior to the tear-drop wing, it also requires more power (i.e. analysis of different wing shape with the same wing kinematics, Section 4.1.2). This is because its shape is more concentrated in the middle section of the wing, where the larger wing area will be exposed to a much higher relative wind velocity. Thus, more aerodynamic power is required ($P \propto V$), unlike the tear-drop shape, which has a much smaller (and tapered) area towards the tip of the wing.

5.2 RECOMMENDATIONS

For future advancement of the model, the following recommendations are being made for future work:

1. **Investigate experimentally the aerodynamic forces that associated with the insect body in flight.**
   The present analysis only based on the modelling of wing, whereas during flight there is some amount of aerodynamic forces that contributed by the body of the insect. Therefore, in order to include this element into the present model, a detailed analysis of measuring the instantaneous body forces is necessary.

2. **Modelling the dynamic of wing-body interaction.**
   The linkage or interaction between wing and the whole body of the insect are important for future development of the model. This will assist towards some other important aspect, such as when dealing with the controllability of the model. Thus, enable to predict the amount of power required for control, corresponding to the prescribe flight mode.

3. **Unsteady aerodynamic theory to accommodate the flexibility of the wing.**
   The flexibility of the wing could potentially provide favourable condition in enhancing the performance of flapping wing flight. This could offer a much complete model (BEMT) to represent the aero-structure of the flapping wing; enable to take account of the instantaneous changes of the shape, density and thickness of the wing that could be constant or vary along the chord and span.

APPENDICES

A. Insect Morphological Data

Table 5-1 The morphological data of hawk moth; data from Ref.[135]

Parameters	Quantity
$M_{insect}(mg)$	1648.00
$M_{wing}(mg)$	47.00
$R(mm)$	51.90
$\bar{c}(mm)$	18.26

Table 5-2 The morphological data of dragonfly; data from Ref.[136,229]

Parameters	Quantity
$M_{insect}(mg)$	121.90
$M_{forewing}(mg)$	$0.01\mathrm{M}_{\mathrm{insect}}$
$M_{hindwing}(mg)$	$0.01\mathrm{M}_{\mathrm{insect}}$
$R_f(mm)$	27.85
$\bar{c}_f(mm)$	5.88
$R_h(mm)$	26.90
$\bar{c}_h(mm)$	7.68

B. Program Structure

In order to give a better understanding of the present model, two main bodies of the program code that represent the present analyses of the flapping wing insect model are presented. These are referred to as 'Aero' for the aerodynamic model (calculates the wing position, velocity, force, and power) and 'Optimiser' for the optimisation (based on PSO), as shown in Figure 3-5 and Figure 3-6 respectively.

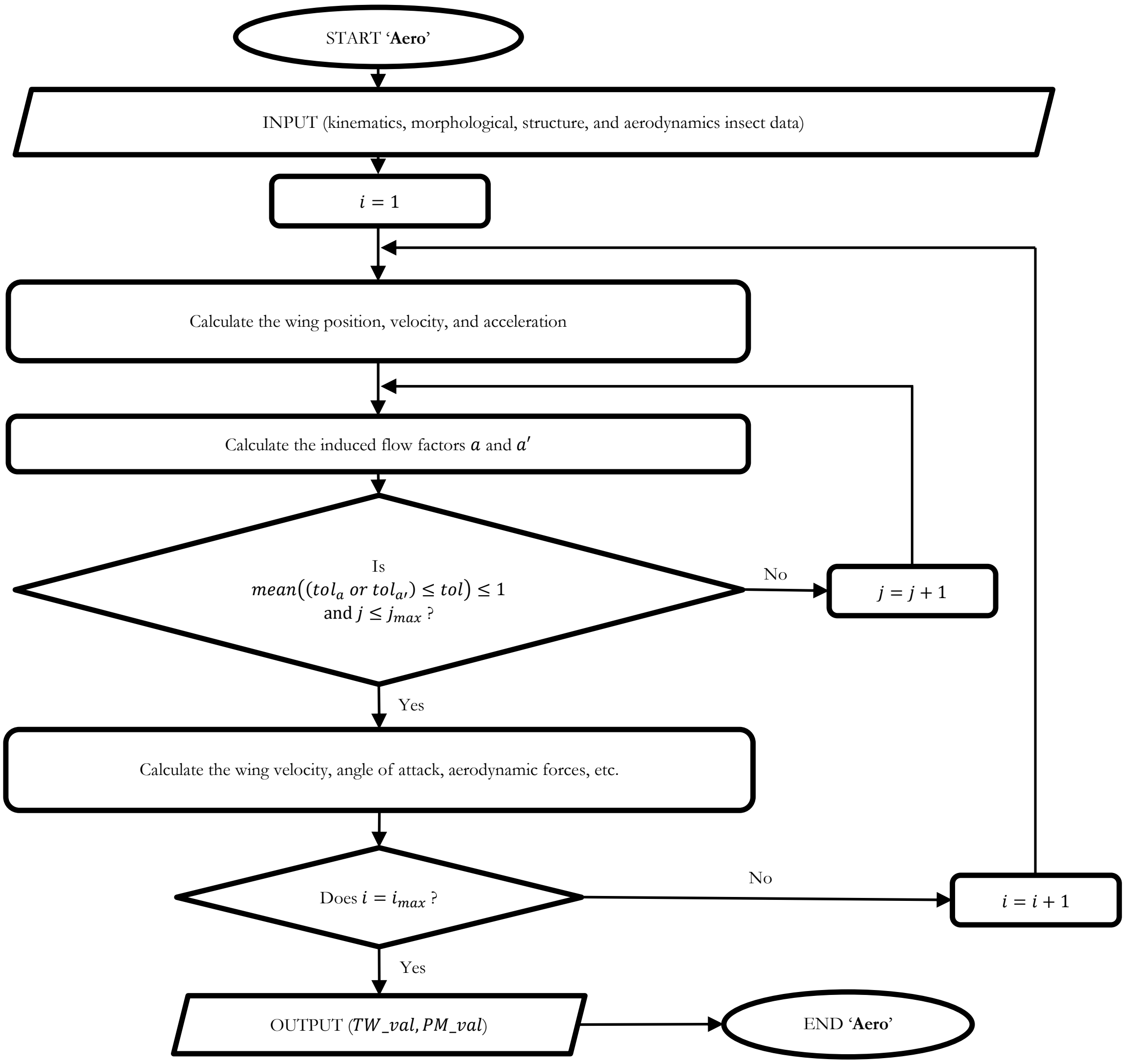

Figure 5-1 Flow structure for the function 'Aero'

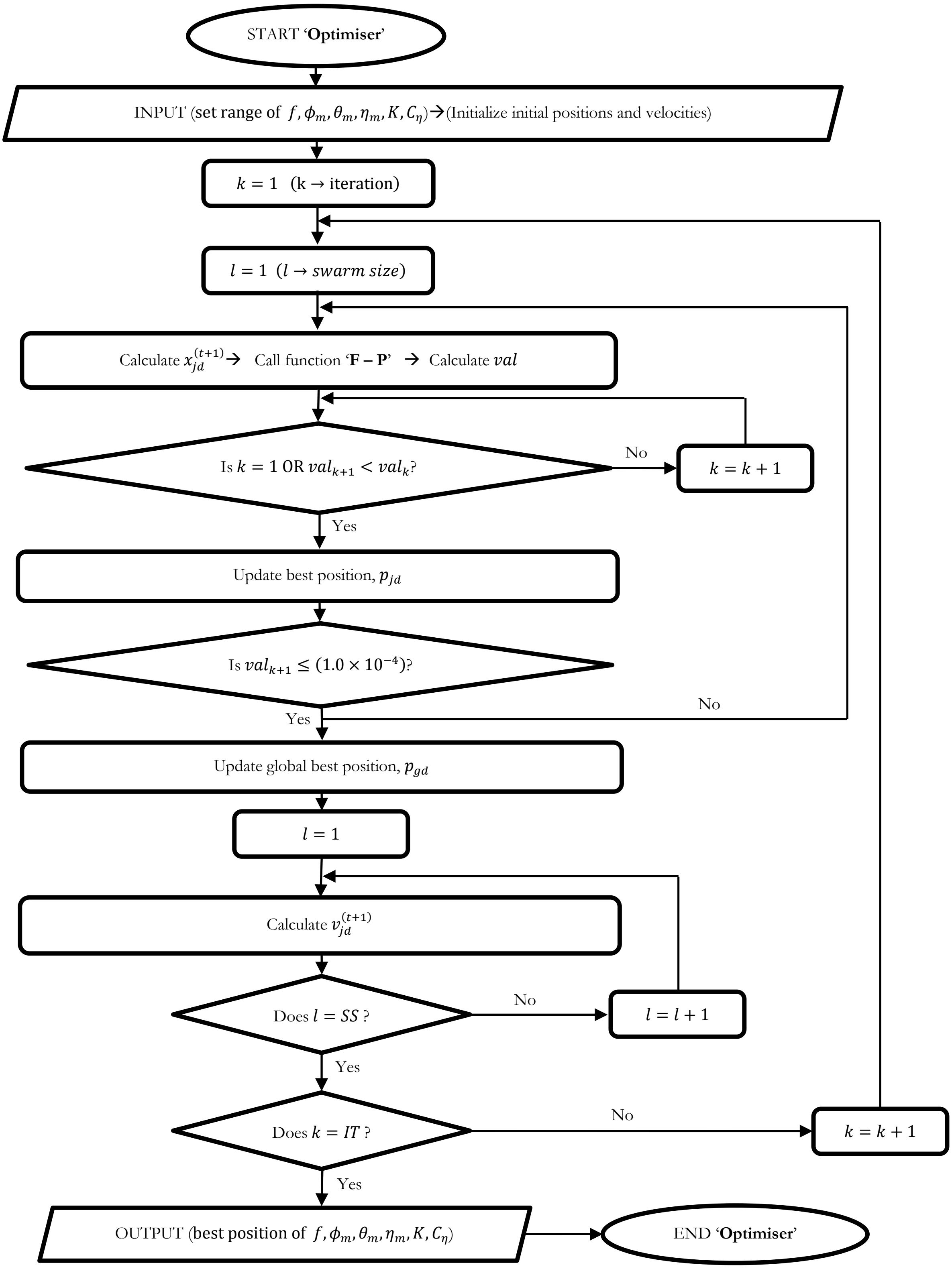

Figure 5-2 Flow structure for the optimisation program 'Optimiser'

C. Aerodynamics of Propeller Blades

A propeller is a mechanical device that converts rotary motion to generate thrust or propulsive force. It is are made up of a series of rotating airfoils that is stacked together side by side, forming a continuous long section, similar to the shape of an aircraft wing. In general, a propeller would have two or three blades depending on their specified purposes. When the propeller rotates, some amount of thrust will be created. Since the propeller blades are made of a series of airfoils, intrinsically the thrust that came from the propeller are forms of both components of lift and drag.

The propeller theory is known to be the most reliable method and has been used routinely by industry for over 100 years. This method is able to provide a quick estimation on the performances of the propeller blades. Principally, this theory is form by two theories; the momentum theory and the blade element theory. That each of them can be used in analysing the propeller performance.

In momentum theory, the whole propeller is mathematically modelled as an actuator disc. It is simple to be implemented and would give a very quick estimation on the propeller performance. This theory also comes with a number of advantages along with a few simplifications and limitations. For instance, the airfoil sections or the actual propeller blade shapes are deserting.

On the other hand, unlike the momentum theory, the blade element theory is able to take into account the actual propeller blade shapes. Using this theory, the propeller blade will be divided into smaller airfoil sections, in which each section are analysed individually. Then, integration takes place to sum up all of the force on each individual of the propeller blade sections. Since this theory uses and dependent on the shapes of an airfoil, this theory is demanding the use of tabulated airfoil data.

When both of these theories are combined, a more exact quantification of the forces acting on the propeller can be made. Furthermore, this combination will eventually allowing the propeller designers to include the induced flow effect and have a more complete solution on the propeller performance with known local geometrical size and shape of each section of the propeller blades.

Momentum Theory

The momentum theory dates back to the pioneer work of WJM Rankine in 1865 and was further advanced by RE Froude[134]. Principally, this method replaces the propeller with an actuator disc with zero thickness in free stream flow domain; by assuming the flow is inviscid, incompressible, irrotational, and uniform. The main attention of the theory was focused on the motion of the fluid; by simplifying the slipstream of the fluid through the rotating propeller blades to be acting as an airscrew disc.

Since then, the theory has been further enriched to include the effects of the rotational motion of the slipstream, the frictional drag of the propeller blades, and the interference of the body on which the airflow is directed. The momentum theory in itself, however, was unable to indicate the shape of the propeller blades. Nevertheless, an important feature of this theory, it has concluded that the axial velocity of the slipstream behind the propeller is higher than the speed of the slipstream with which the propeller is advancing.

The Axial Momentum Theory

In axial momentum theory, the entire propeller is modelled with an actuator disc. The flow comes from far upstream at the inlet domain with velocity V_{∞}, and exit through the outlet domain with velocity V_e. As the flow is drawn into the actuator disc, it acquires a velocity V_1, and this velocity will remain the same through the actuator disc. For the pressure, however, it will have a sudden increase from P_1 to P_2 as it is crossing through the actuator disc.

Following this theory, there are several assumptions that needs to be comply with,

1. The propeller is to be replaced by a very small thickness actuator disc with a projected frontal area of A, acting as a flow actuator or a flow energizer.
2. The fluid is a perfect incompressible, and the flow is irrotational in front of and behind the disc.
3. The body is purely porous, so there is no resistance such as drag onto the flow passing through the actuator disc.
4. The axial velocity as it approaches or comes near the disc is uniform and smooth, with no abrupt or jump change as it passes through the actuator disc.

5. The pressure just behind the actuator disc is higher than the pressure just before the actuator disc, and it is uniformly distributed across the entire disc surface. This differential pressure occurs as some work (or energy) is given to the disc in actuating the flow.
6. The static pressure far upstream and far downstream are both equal to the atmospheric pressure. The corresponding velocities, however, will have its own independent value on both upstream and downstream, which have to be determined separately.

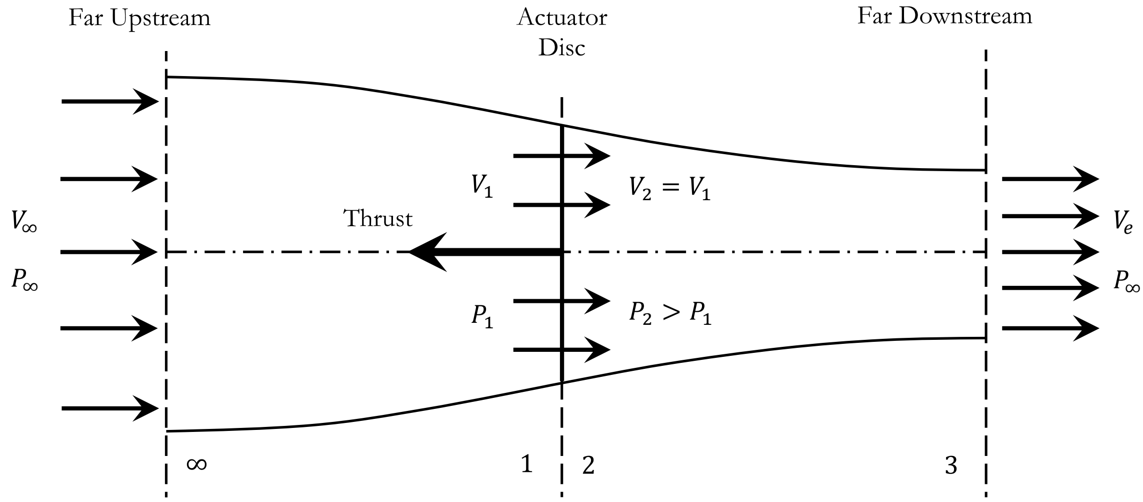

Figure 5-3 Actuator disc model

From the conservation of mass, the mass flow through the disk, given as

$$\dot{m} = \rho A V \tag{5-1}$$

The thrust produced by the disk from Newton's second and third laws (change in momentum in air) resulting in reaction force, thrust.

$$T = \dot{m}\partial V = \rho A V (V_e - V_\infty) \tag{5-2}$$

From simple fluid statics, thrust is produced by the differential static pressure on either side of the disk, multiplied by its surface area (swept area)

$$T = A(P_2 - P_1) \tag{5-3}$$

Applying Bernoulli's equation on either side of the disk, but not through it, gives

$$P_\infty + \frac{1}{2}\rho {V_\infty}^2 = P_1 + \frac{1}{2}\rho {V_1}^2$$
$$P_2 + \frac{1}{2}\rho {V_2}^2 = P_\infty + \frac{1}{2}\rho {V_e}^2 \quad 5\text{-}4$$

Since $V_2 = V_1$,

$$P_2 - P_1 = \frac{1}{2}\rho\left({V_e}^2 - {V_\infty}^2\right) \quad 5\text{-}5$$

Hence,

$$V_1 = \frac{1}{2}(V_e + V_\infty) \quad 5\text{-}6$$

This simple analysis shows that the airflow velocity through the actuator disk is the mean of the velocities upstream and downstream of the propeller. This simple conclusion drawn out of the simplified flow model permits design, analysis, and even experimental verification of the propeller performance rather quickly. Thus, thrust

$$T = \frac{1}{2}\rho\left({V_e}^2 - {V_\infty}^2\right)A \quad 5\text{-}7$$

The velocity at the disk comes out to be the free stream axial velocity, V_∞ plus induced (axial) velocity v, whereas, the far downstream velocity is equal to the free stream velocity plus two times the induced velocity, v.

$$V_1 = V_\infty + v \quad and \quad V_e = V_\infty + 2v \quad 5\text{-}8$$

The General Momentum Theory

Following the axial momentum theory, it was assumed that there was no rotational motion in the slipstream, no change to the fluid flow velocity, and the propeller was replaced by a pressure jump represented by an actuator disk. This assumption, however, is only valid for infinite propeller blades because the theory unable to justify the actual physics of the flow as it leaves the actuator disk[230]. Since, in reality, the rotational motion of the blades will impart some form of rotational motion to the fluid that eventually will imply a further loss of energy. Therefore, by assuming that the blades can also impart a rotational component to the fluid velocity while the axial and radial components remain unchanged, this theory was extended to modify the qualities of the actuator disk[134].

The formulation of this theory can be represented with an analysis of a rotating annular stream tube, as given in Figure 5-4. The mathematical relation between the upstream fluid flow and the corresponding wake velocities at the downstream for the annular element taken on the rotor plane can be expressed as

$$u_w r_w \, dr_w = ur \, dr \tag{5-9}$$

For circular motion $u_w = w_w r_w$ and $u = wr$, the conservation of the angular momentum on upstream and the wake region of the flow domain gives

$$w_w {r_w}^2 = wr^2 \tag{5-10}$$

By applying the angular momentum balance on the differential annular element, the torque can be obtained using

$$dQ = \rho uwr^2 \, dA \tag{5-11}$$

where $dA = 2\pi r \, dr$.

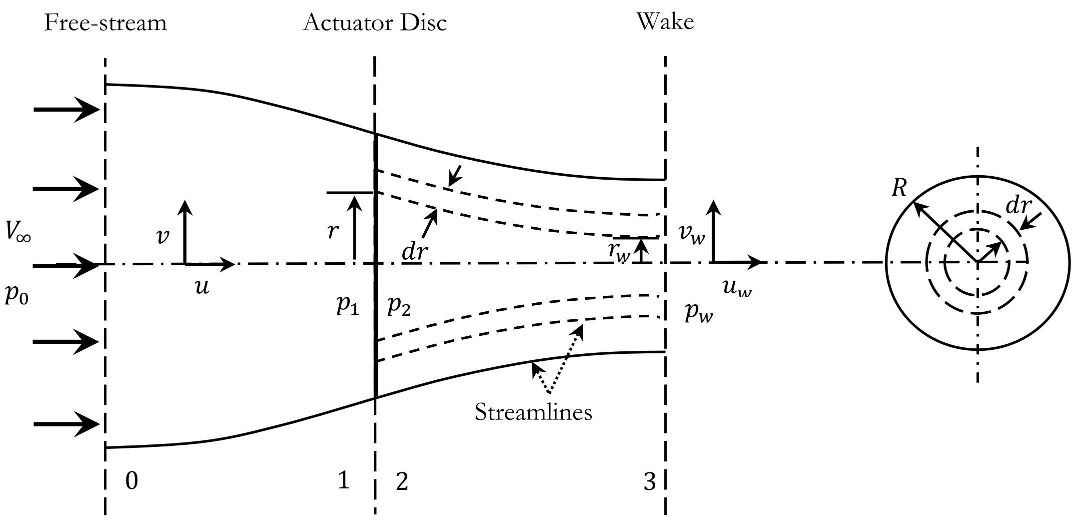

Figure 5-4 Rotating annular stream tube analysis

By applying the Bernoulli equation between station 0 and 1 then between 2 and 3 gives

$$H_0 = p_0 + \frac{1}{2}\rho V_\infty{}^2 = p_1 + \frac{1}{2}\rho(u^2 + v^2) \tag{5-12}$$

$$H_1 = p_2 + \frac{1}{2}\rho(u^2 + v^2 + w^2 r^2) = p_w + \frac{1}{2}\rho(u_w{}^2 + w_w{}^2 r_w{}^2) \tag{5-13}$$

Then, with $p_2 = p_1 + p'$, taking the difference between these constants gives

$$H_1 - H_0 = p' + \frac{1}{2}\rho(w^2 r^2) \tag{5-14}$$

This means the kinetic energy of the rotational motion given to the fluid by the torque of the blade is equal to $(1/2)\rho(w^2 r^2)$. Thus, the total pressure head between both sides of the rotor becomes

$$\begin{aligned} p_0 - p_w &= \frac{1}{2}\rho\left(u_w{}^2 - V_\infty{}^2\right) + \frac{1}{2}\rho w_w{}^2 r_w{}^2 - (H_1 - H_0) \\ &= \frac{1}{2}\rho\left(u_w{}^2 - V_\infty{}^2\right) + \frac{1}{2}\rho(w_w{}^2 r_w{}^2 - w^2 r^2) - p' \end{aligned} \tag{5-15}$$

Applying the Bernoulli's equation between station 2 and 3 gives the pressure increase as

$$p' = \frac{1}{2}\rho[\Omega^2 - (\Omega - w)^2]r^2 = \rho\left(\Omega - \frac{1}{2}w\right)wr^2 \tag{5-16}$$

Substituting this result into the Eqn. 5-15 gives

$$p_0 - p_w = \frac{1}{2}\rho\left(u_w{}^2 - V_\infty{}^2\right) - \rho\left(\Omega - \frac{1}{2}w\right)w_w r_w{}^2 \tag{5-17}$$

In station 3, the pressure gradient in the wake balances the centrifugal force on the fluid and can be written as

$$\frac{dp_w}{dr_w} = \rho w_w{}^2 r_w \tag{5-18}$$

Differentiating Eqn. 5-17 relative to r_w and equating to Eqn. 5-18 gives the connection between the axial and rotational velocities in the wake

$$\frac{1}{2}\frac{d}{dr_w}\left({u_w}^2 - {V_\infty}^2\right) = (\Omega - w_w)\frac{d}{dr_w} w_w {r_w}^2 \tag{5-19}$$

The equation of axial momentum for the given annular blade element in differential form can be written as

$$dT = \rho u_w (u_w - V_\infty) dA_w - (p_0 - p_w) dA_w \tag{5-20}$$

Since $dT = p' dA$, Eqn. 5-20 can be written as

$$dT = \rho\left(\Omega - \frac{1}{2}w\right) w r^2 \, dA \tag{5-21}$$

Thus, combining Eqn. 5-9, 5-15, 5-20, and 5-21 gives

$$\frac{1}{2}(u_w - V_\infty)^2 = \left[\frac{\Omega - \frac{1}{2}w}{u} - \frac{\Omega - \frac{1}{2}w_w}{u_w}\right] u_w {r_w}^2 w_w \tag{5-22}$$

An exact solution of the stream-tube equations can be obtained when the flow in the slipstream is irrotational except along the axis. This condition implies that the rotational momentum wr^2 has the same value for all radial elements. Defining the axial velocities upstream of the disk and downstream at the wake as $u = V_\infty(1 + a)$ and $u_w = V_\infty(1 + b)$, respectively, gives

$$a = \frac{1}{2} b \left[1 + \frac{\lambda^2 (1 + a) b^2}{4(b - a)}\right] \tag{5-23}$$

Similarly, the thrust on the differential element is equal to

$$dT = 2\rho u (u - V_\infty) dA = 4\pi\rho {V_\infty}^2 (1 + a) a r \, dr \tag{5-24}$$

Using Eqn. 5-16, Eqn. 5-24 can be rewritten as

$$dT = p' dA = 2\pi\rho\left(\Omega - \frac{1}{2}w\right) w r^3 \, dr \tag{5-25}$$

If the angular induction factor is defined as $w = 2a'\Omega$, then alternatively dT becomes

$$dT = 4\pi\rho\Omega^2 (1 - a') a' r^3 \, dr = 4\pi\rho {V_\infty}^2 (1 + a) a r \, dr \tag{5-26}$$

To obtain a relationship between axial induction factor and angular induction factor, Eqn. 5-25 and 5-26 can be equated which gives

$$V_\infty{}^2(1+a)a = \Omega^2 r^2 (1-a')a' \tag{5-27}$$

Finally, using Eqn. 5-11, the torque on the differential element can be calculated as

$$d\tau = 4\pi\rho V_\infty \Omega(1+a)a' r^3\, dr = 4\pi\rho V_\infty \Omega(1+a)a' r^3\, dr \tag{5-28}$$

Blade Element Theory

The blade element theory (BET) assumes that the blade can be analysed as a number of independent elements in the span-wise direction. In the design of an aircraft wing, these independent elements are to be made up by a series of airfoil shapes with known lift L and drag D characteristics. The characteristic of these forces can be determined from the empirical experimental data, numerical simulation, or using the aerodynamic theory.

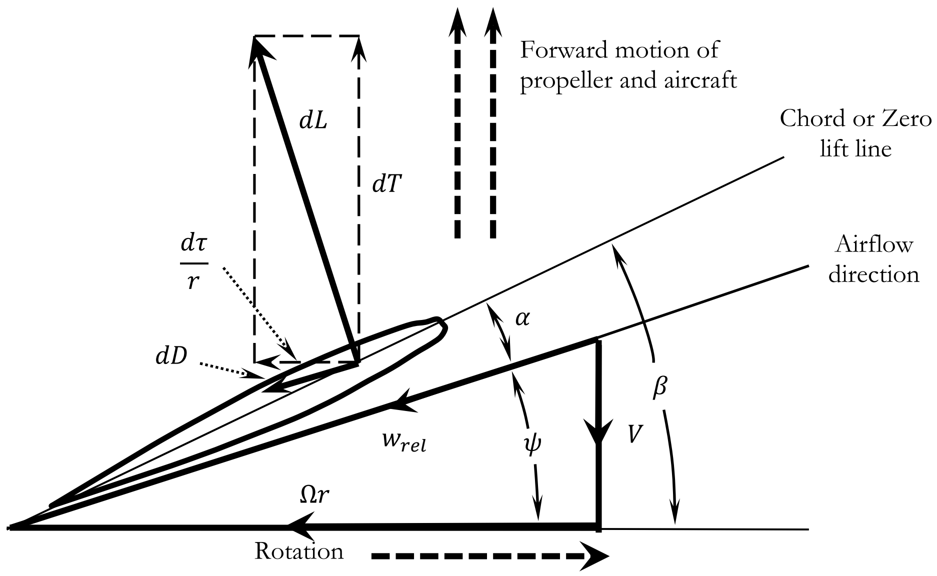

Figure 5-5 Flow geometry for blade element at radial station r

Using the blade elemental lift and drag characteristics, the thrust and the torque on each element of the propeller blade can be expressed as,

$$dT = dL\cos\psi - dD\sin\psi = \frac{1}{2}\rho {w_{rel}}^2\,(C_l\cos\psi - C_d\sin\psi)c(r)\;dr \qquad 5\text{-}29$$

$$d\tau = dL\sin\psi + dD\cos\psi = \frac{1}{2}\rho {w_{rel}}^2\,(C_l\sin\psi + C_d\cos\psi)c(r)\;r\;dr \qquad 5\text{-}30$$

Substituting for resultant inflow velocity incident and aligned to the blade element,

$$w_{rel} = \frac{V}{\sin\psi} \qquad 5\text{-}31$$

and for incoming flow dynamic head based on forward velocity of the element,

$$q = \frac{1}{2}\rho V^2 \tag{5-32}$$

Hence, the thrust and the torque,

$$dT = \frac{q\, c(r)\, dr}{\sin^2 \psi}\ (C_l \cos\psi - C_d \sin\psi) \tag{5-33}$$

$$d\tau = \frac{q\, c(r)\, r\, dr}{\sin^2 \psi}\ (C_l \sin\psi + C_d \cos\psi) \tag{5-34}$$

Finally, the thrust and the torque per unit radius on the wing elements are given as

$$dT = \frac{1}{2}\ \rho\, \mathrm{w}_{rel}{}^2\ c(r)\ C_z\ dr \tag{5-35}$$

$$d\tau = \frac{1}{2}\ \rho\, \mathrm{w}_{rel}{}^2\ c(r)\ C_y\ r\ dr \tag{5-36}$$

where $\mathrm{w}_{rel} = v/\sin\psi = (1+a)\ v_z/\sin\psi$, and the horizontal C_y and vertical C_z wing-segment force coefficients are expressed as

$$\begin{cases} C_y = C_l \sin\psi + C_d \cos\psi \\ C_z = C_l \cos\psi - C_d \sin\psi \end{cases} \tag{5-37}$$

Prandtl Momentum Tip-Loss Factor

The original blade element theory does not consider the three-dimensional flow effects due to the influence of vortices shed from the blade tips into the slipstream on the induced velocity field. This effect is an important factor in calculating the performance of the propeller blade, as it will tend to give significant over predicted results if ignored [231].

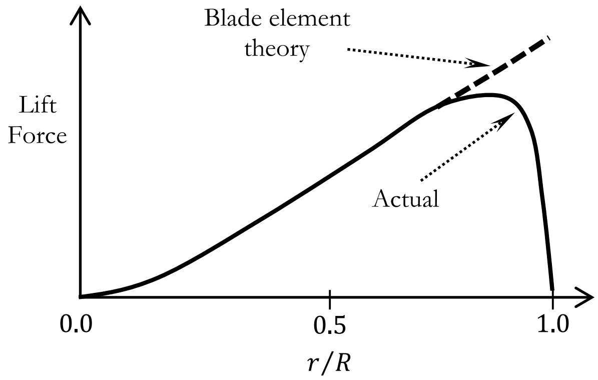

Figure 5-6 Typical actual lift force loading distributions on the propeller blade as compared to the original blade element theory; showing the loss of lift at the tip.

An example of such typical comparison on the lift force loading distributions of a propeller blade between the actual and those predicted via the original blade element theory is illustrated in Figure 5-6. It has shown that this momentum tip-loss effect was found to be most pronounced near the outer portion of the propeller blade tip. In which, the air tends to flow over the tip from the lower surface of the blade, effectively altering the pressure acting on the blade. Consequently, this will prominently tend to decrease the lift force near the tip of the wing.

To account for this deficiency, a tip-loss factor (or momentum correction factor), F_m, originally developed by Prandtl is used [134]. This theory is summarized by a correction to the induced velocity field and can be expressed simply by the following:

$$F_m = \frac{2}{\pi} \arccos \left\{ \exp \left[-\frac{N_{wing}}{2} \frac{(1 - r/R)}{\sin \psi_t} \right] \right\} \qquad 5\text{-}38$$

where $\psi_t = \arctan \left(\frac{r}{R} \tan \psi \right)$ is the flow angle at the tip.

Now, to relate this momentum tip-loss with the induced flow effect as introduced in the general momentum theory (Section 0) on the propeller blade thrust and torque, the Eqn. 5-26 & 5-28 is modified by introducing the correction factor F_m from Eqn. 5-38,

$$dT = 4\pi\rho V^2(1+a)arF_m\,dr \tag{5-39}$$

$$d\tau = 4\pi\rho V\Omega(1+a)a'r^3F_m\,dr \tag{5-40}$$

Blade Element Momentum Theory

The blade element momentum theory (BEMT) refers to the conclusion of the axial and radial induced flow factors that will influence the performance of the propeller blade. It is a hybrid method that was proposed for calculating the helicopter performance, and is formulated by merging the general momentum theory and the blade element theory. This combination allows the estimation of the local inflow distribution of the respective velocities and the corresponding angles along the blade.

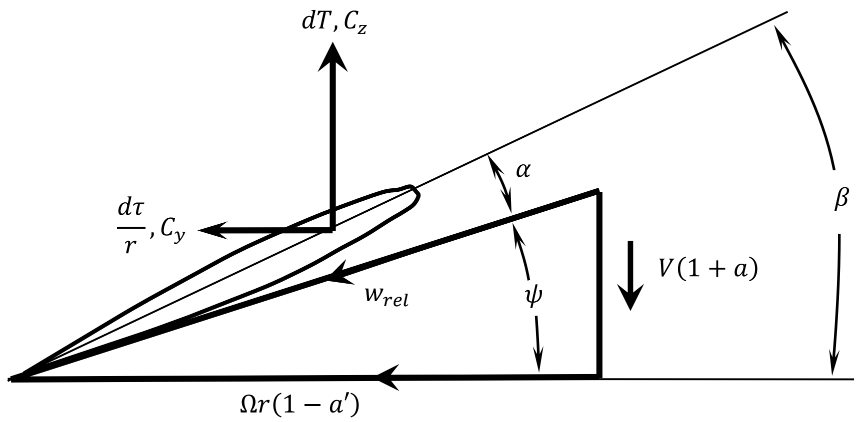

Figure 5-7 Flow geometry with axial and radial induced flow factors for blade element at radial station r

From the general momentum theory and with the insertion of the momentum tip-loss factor, the thrust and torque per unit radius on the wing elements can be obtained as,

$$dT = 4\pi\rho V^2(1+a)arF_m\, dr \tag{5-41}$$

$$d\tau = 4\pi\rho V\Omega(1+a)a'r^3F_m\, dr \tag{5-42}$$

On similar expression, from the blade element theory, the thrust and torque per unit radius on the wing elements can be expressed as,

$$dT = \frac{1}{2}\,\rho\, \mathrm{w}_{rel}{}^2\; c(r)\; C_z\; dr \tag{5-43}$$

$$d\tau = \frac{1}{2}\,\rho\, w_{rel}{}^2\; c(r)\; C_y\; r\; dr \tag{5-44}$$

Equating Eq. 5-41 with Eq. 5-43, and Eq. 5-42 with Eq. 5-44, the axial and radial induction factors (as shown in Figure 2-16) can be simplified as,

$$a = \frac{\sigma K_a}{F_m - \sigma K_a} \quad \text{and} \quad a' = \frac{\sigma K_{a'}}{F_m + \sigma K_{a'}} \tag{5-45}$$

where the axial K_a and radial $K_{a'}$ Goldstein momentum loss factors [16], and the local solidity σ that represents the ratio of the lifting area of the wing to the area of the disk,

$$K_a = \frac{C_z}{4\sin^2\psi} \quad \text{and} \quad K_{a'} = \frac{C_y}{4\cos\psi\sin\psi} \tag{5-46}$$

$$\sigma = \frac{N_{wing}c(r)}{2\pi r} \tag{5-47}$$

D. Conference Presentation

The conference presentation given by the time of thesis submission:

- Induced flow effects in Flapping Wing Flight, 9th International Conference on Advanced Computational Engineering and Experimenting (ACE-X2015), Munich, 29th June – 2nd July 2015.

REFERENCES

1. Zheng, L., Hedrick, T. & Mittal, R. A comparative study of the hovering efficiency of flapping and revolving wings. *Bioinspiration & Biomimetics Journal* **8,** 36001 (2013).
2. Taha, H. E., Hajj, M. R. & Nayfeh, A. H. Wing kinematics optimization for hovering micro air vehicles using calculus of variation. *Journal of Aircraft* **50,** 610–614 (2013).
3. Salehipour, H. & Willis, D. J. A coupled kinematics–energetics model for predicting energy efficient flapping flight. *Journal of Theoretical Biology* **318,** 173–196 (2013).
4. Ma, K. Y., Chirarattananon, P., Fuller, S. B. & Wood, R. J. Controlled flight of a biologically inspired, insect-scale robot. *Science* **340,** 603–607 (2013).
5. Lee, J. S. & Lee, S. H. Fluid–structure interaction for the propulsive velocity of a flapping flexible plate at low Reynolds number. *Computers & Fluids* **71,** 348–374 (2013).
6. Pesavento, U. & Wang, Z. J. Flapping wing flight can save aerodynamic power compared to steady flight. *Physical review letters* **103,** 118102 (2009).
7. Fenelon, M. A. A. & Furukawa, T. Design of an active flapping wing mechanism and a micro aerial vehicle using a rotary actuator. *Mechanism and Machine Theory* **45,** 137–146 (2010).
8. Ellington, C. P. The novel aerodynamics of insect flight: applications to micro-air vehicles. *Journal of Experimental Biology* **202,** 3439–3448 (1999).
9. Madangopal, R., Khan, Z. A. & Agrawal, S. K. Energetics-based design of small flapping-wing micro air vehicles. *IEEE/ASME Transactions on Mechatronics* **11,** 433–438 (2006).
10. Rakotomamonjy, T., Ouladsine, M. & Moing, T. L. Modelization and kinematics optimization for a flapping-wing micro air Vehicle. *Journal of Aircraft* **44,** 217–231 (2007).
11. George T. Yates. Optimum pitching axes in flapping wing propulsion. *Journal of Theoretical Biology* **120,** 255–276 (1986).
12. Ansari, S. A., Żbikowski, R. & Knowles, K. Aerodynamic modelling of insect-like flapping flight for micro air vehicles. *Progress in Aerospace Sciences* **42,** 129–172 (2006).
13. Nagai, H. & Isogai, K. Effects of flapping wing kinematics on hovering and forward flight aerodynamics. *AIAA Journal* **49,** (2011).
14. Minami, K., Suzuki, K. & Inamuro, T. Free flight simulations of a dragonfly-like flapping wing-body model using the immersed boundary-lattice Boltzmann method. *The Japan Society of Fluid Mechanics* **47,** 1–17 (2015).
15. Kennedy, J. Particle swarm optimization. *Encyclopedia of Machine Learning* 760–766 (2010).
16. Adkins, C. N. & Liebeck, R. H. Design of optimum propellers. *Journal of Propulsion and Power* **10,** 676–682 (1994).

17. Berman, G. J. & Wang, Z. J. Energy-minimizing kinematics in hovering insect flight. *Journal of Fluid Mechanics* **582,** 153–168 (2007).

18. Taha, H. E., Hajj, M. R. & Beran, P. S. State-space representation of the unsteady aerodynamics of flapping flight. *Journal of Aerospace Science and Technology* **34,** 1–11 (2014).

19. Wang, Z. J., Birch, J. M. & Dickinson, M. H. Unsteady forces and flows in low Reynolds number hovering flight: two-dimensional computations vs robotic wing experiments. *J Exp Biol* **207,** 449–460 (2004).

20. Kornushenko, A. V., Shustov, A. V., Lyapunov, S. V. & Serokhvostov, S. V. Numerical, experimental and flight investigation of MAV aerodynamics. *3rd US-European Competition and Workshop on Micro Air Vehicle Systems (MAV07) & European Micro Air Vehicle Conference and Flight Competition* (2007).

21. Kroo, I. & Kunz, P. *Development of the Mesicopter: A Miniature Autonomous Rotorcraft*. (Stanford University, 2000).

22. Bouabdallah, S., Murrieri, P. & Siegwart, R. Towards autonomous indoor micro VTOL. *Journal of Autonomous Robot* **18,** 171–183 (2005).

23. Thipyopas, C., Sun, A. B., Bernard, E. & Moschetta, J. M. Application of Electro-Active Materials to a Coaxial-Rotor NAV. in *Proceedings of the International Micro Air Vehicles conference 2011 summer edition* (Delft University of Technology and Thales, 2011).

24. Chung, H.-C. *et al.* Development of piezoelectric fans for flapping wing application. *Sensors and Actuators A: Physical* **149,** 136–142 (2009).

25. Djojodihardjo, H., Ramli, A. S. S. & Wiriadidjaja, S. Kinematic and aerodynamic modelling of flapping wing ornithopter. *Procedia Engineering* **50,** 848–863 (2012).

26. Bos, F. M., Lentink, D., Oudheusden, B. W. van & Bijl, H. Influence of wing kinematics on aerodynamic performance in hovering insect flight. *Journal of Fluid Mechanics* **594,** 341–368 (2008).

27. Lee, J.-S., Kim, J.-H. & Kim, C. Numerical study on the unsteady-force-generation mechanism of insect flapping motion. *AIAA Journal* **46,** 1835–1848 (2008).

28. Hylton, T., Martin, C., Tun, R. & Castelli, V. The DARPA nano air vehicle program. *50th AIAA Aerospace Sciences Meeting Including the New Horizons Forum and Aerospace Exposition* (2012).

29. Zdunich, P., Bilyk, D., MacMaster, M. & Loewen, D. Development and testing of the mentor flapping-wing micro air vehicle. *Journal of Aircraft* **44,** 1701–1711 (2007).

30. Stanford, B. & Beran, P. Conceptual design of compliant mechanisms for flapping wings with topology optimization. *AIAA Journal* **49,** (2011).

31. Grasmeyer, J. M. & Keennon, M. T. Development of the Black Widow micro air vehicle. *AIAA Journal* (2001).

32. Datta, A. *et al.* Design of a martian autonomous rotary-wing vehicle. *Journal of Aircraft* **40,** 461–472 (2003).

33. Wood, R. J. *et al.* An autonomous palm-sized gliding micro air vehicle: design, Fabrication, and results of a fully integrated centimeter-scale MAV. *IEEE Robotics and Automation Magazine* **14,** 82–91 (2007).

34. Petricca, L., Ohlckers, P. & Grinde, C. Micro- and nano-air vehicles: state of the art. *International Journal of Aerospace Engineering* (2011). doi:10.1155/2011/214549

35. Galinski, C., Mieloszyk, J. & Piechna, J. Progress in the gust resistant MAV programme. *27th international Congress of the Aeronautical Sciences* (2010).

36. Wu, H., Sun, D. & Zhou, Z. Micro air vehicle: configuration, analysis, fabrication, and test. *IEEE/ASME Transactions on Mechatronics* **9,** 108–117 (2004).

37. Zhang, F. *et al.* A novel micro air vehicle with flexible wing integrated with on-board electronic devices. *Conference on Robotics, Automation and Mechatronics, 2008 IEEE*. 252–257 (2008).

38. Pereira, J. L. Hover and wind-tunnel testing of shrouded rotors for improved micro air vehicle design. (University of Maryland, 2008).

39. Madangopal, R., Khan, Z. & Agrawal, S. Biologically inspired design of small flapping wing air vehicles using four-bar mechanisms and quasi-steady aerodynamics. *Journal of Mechanical Design* **127,** 809–816 (2005).

40. Wood, R. J. The first take-off of a biologically inspired at-scale robotic insect. *IEEE Transactions on Robotics* **24,** 341–347 (2008).

41. Jones, K., Bradshaw, C., Papadopoulos, J. & Platzer, M. Improved performance and control of flapping-wing propelled micro air vehicles. *AIAA, Aerospace Sciences Meeting, 42nd, Reno, NV* (2004).

42. Whitney, J. P. Design and performance of insect-scale flapping-wing vehicles. (Harvard University, 2012).

43. Breugel, F. van, Teoh, Z. E. & Lipson, H. in *Flying insects and robots* 171–184 (Springer Berlin Heidelberg, 2010).

44. Finio, B. M., Perez-Arancibia, N. O. & Wood, R. J. System identification and linear time-invariant modelling of an insect-sized flapping-wing micro air vehicle. *2011 IEEE/RSJ International Conference on Intelligent Robots and Systems (IROS)* 1107–1114 (2011).

45. Bueno, S. S. *et al.* Project AURORA: Towards an autonomous robotic airship. *Proceedings of the Workshop WS6 Aerial Robotics* 43–54 (2002).

46. Yearbook, U. *UAS: The global perspective*. **164,** (UAS Yearbook, 2009).

47. Pines, D. J. & Bohorquez, F. Challenges facing future micro-air-vehicle development. *Journal of Aircraft* **43,** 290–305 (2006).

48. Wood, R. J. *et al.* Progress on 'pico' air vehicles. *The International Journal of Robotics Research* **31,** (2012).

49. Shyy, W. *et al.* Recent progress in flapping wing aerodynamics and aeroelasticity. *Progress in Aerospace Sciences* **46,** 284–327 (2010).

50. David Webster. Aerial footage shows 200-year-old pub destroyed as River Irwell floods. *The Telegraph* (2015).

51. Ramezani, A., Shi, X., Chung, S.-J. & Hutchinson, S. Nonlinear flight controller synthesis of a bat-inspired micro aerial vehicle. *AIAA Guidance, Navigation, and Control Conference, San Diego, California, USA* (2016).

52. Khan, Z. A. & Agrawal, S. K. Optimal hovering kinematics of flapping wings for micro air vehicles. *AIAA Journal* **49,** 257–268 (2011).

53. Orlowski, C. T. & Girard, A. R. Dynamics, stability, and control analyses of flapping wing micro-air vehicles. *Progress in Aerospace Sciences* **51,** 18–30 (2012).

54. Pourtakdoust, S. H. & Aliabadi, S. K. Evaluation of flapping wing propulsion based on a new experimentally validated aeroelastic model. *Scientia Iranica* **19,** 472–482 (2012).

55. Bachmann, R. J., Boria, F. J., Vaidyanathan, R., Ifju, P. G. & Quinn, R. D. A biologically inspired micro-vehicle capable of aerial and terrestrial locomotion. *Journal of Mechanism and Machine Theory* **44,** 513–526 (2009).

56. McMichael, J. M. & Francis, C. M. S. Micro Air Vehicles - Toward a New Dimension in Flight. (1997). Available at: http://www.fas.org/irp/program/collect/docs/mav_auvsi.htm. (Accessed: 26th June 2013)

57. Strohm, K. M., Schmuckle, F. J., Schauwecker, B. & Luy, J. F. Silicon micromachined RF MEMS resonators. *Microwave Symposium Digest, 2002 IEEE MTT-S International Seattle, WA, USA* **2,** 1209–1212 (2002).

58. Kim, B., Candler, R. N., Hopcroft, M. & Agarwal, M. Frequency stability of wafer-scale encapsulated MEMS resonators. *Tech. Dig., Int. Conf. Solid-State Sensors, Actuators, Microsyst. (Transducers'05) Seoul, Korea* **2,** 1965–1968 (2005).

59. Santhanakrishnan, A. & Jacob, J. D. Effect of regular surface perturbations on flow over an airfoil. *35th AIAA Fluid Dynamics Conference, Toronto, Canada* (2005).

60. Bhave, S. A., Gao, D., Maboudian, R. & Howe, R. T. Fully-differential poly-SiC Lame mode resonator and checkerboard filter. in 223–226 (2005).

61. Spinella, I., Mammano, G. S. & Dragoni, E. Conceptual design and simulation of a compact shape memory actuator for rotary motion. *Journal of Materials Engineering and Performance* **18,** 638–648 (2009).

62. Serokhvostov, S. V. Ways and technologies required for MAV miniaturization. *Proceedings of the European Micro Air Vehicle Conference (EMAV '08)* (2008).

63. Mueller, T. J. Aerodynamic measurements at low Reynolds numbers for fixed wing micro-air vehicles. *Presented at the "Development and Operation of UAVs for Military and Civil Applications" course held at the von Karman Institute for Fluid Dynamics, Belgium* (1999).

64. Shyy, W., Lian, Y., Tang, J., Viiero, D. & Liu, H. *Aerodynamics of low Reynolds number flyers*. (Cambridge University Press, 2008).

65. Al-Bahi, I. M. A.-Q. A. A. M. Micro aerial vehicles design challenges: state of the art review. *Proceedings of the SAS UAV Scientific Meeting & Exhibition* (2006).

66. Yuan, W. & Khalid, M. Simulation of insect-sized flapping-wing aerodynamics. *48th AIAA Aerospace Sciences Meeting Including the New Horizons Forum and Aerospace Exposition, Orlando, FL* (2010).

67. Hu, H., Clemons, L. & Igarashi, H. An experimental study of the unsteady vortex structures in the wake of a root-fixed flapping wing. *Experiments in Fluids* **51,** 347–359 (2011).

68. Dudley, R. *The biomechanics of insect flight: form, function, evolution*. (Princeton Univ. Press, 2002).

69. Gullan, P. J. & Cranston, P. S. *The insects: an outline of entomology*. (Chapman & Hall, 1994).

70. Grodnitsky, D. L. & Morozov, P. P. Vortex formation during tethered flight of functionally and morphologically two-winged insects, including evolutionary considerations on insect flight. *Journal of experimental biology* **182,** 11–40 (1993).

71. Bomphrey, R. J., Lawson, N. J., Harding, N. J., Taylor, G. K. & Thomas, A. L. R. The aerodynamics of Manduca sexta: digital particle image velocimetry analysis of the leading-edge vortex. *Journal of Experimental Biology* **208,** 1079–1094 (2005).

72. Birch, J. M. & Dickinson, M. H. Spanwise flow and the attachment of the leading-edge vortex on insect wings. *Nature* **412,** 729–733 (2001).

73. Chinery, M. *Insects of Britain and Western Europe*. (1986).

74. Maxworthy, T. Experiments on the Weis-Fogh mechanism of lift generation by insects in hovering flight. Part 1. Dynamics of the 'fling'. *J. Fluid Mech* **93,** 47–63 (1979).

75. Savage, S. B., Newman, B. G. & Wong, D. T.-M. The role of vortices and unsteady effects during the hovering flight of dragonflies. *The Journal of Experimental Biology* **83,** 59–77 (1979).

76. Wang, Z. J., Birch, J. M. & Dickinson, M. H. Unsteady forces and flows in low Reynolds number hovering flight: two-dimensional computations vs robotic wing experiments. *Journal of Experimental Biology* **207,** 449–460 (2004).

77. Van Den Berg, C. & Ellington, C. P. The three-dimensional leading-edge vortex of a'hovering'model hawkmoth. *Philosophical Transactions of the Royal Society B: Biological Sciences* **352,** 329 (1997).

78. Wang, Z. J. & Russell, D. Effect of forewing and hindwing interactions on aerodynamic forces and power in hovering dragonfly flight. *Physical review letters* **99,** 148101 (2007).

79. Le, T. Q. *et al.* Numerical investigation of the aerodynamic characteristics of a hovering Coleopteran insect. *Journal of Theoretical Biology* **266,** 485–495 (2010).

80. Ren, H., Wu, Y. & Huang, P. G. Visualization and characterization of near-wake flow fields of a flapping-wing micro air vehicle using PIV. *Journal of Visualization* **16,** 75–83 (2013).

81. Yin, B. & Luo, H. Effect of wing inertia on hovering performance of flexible flapping wings. *Physics of Fluids* **22,** 111902 (2010).

82. Tuncer, I. H. & Kaya, M. Optimization of flapping airfoils for maximum thrust and propulsive efficiency. *AIAA journal* **43,** 2329–2336 (2005).

83. Liu, H., Ellington, C. & Kawachi, K. A computational fluid dynamic study of hawk moth hovering. *Journal of Experimental Biology* **201,** 461–477 (1998).

84. Sun, M. & Tang, J. Lift and power requirements of hovering flight in Drosophila virilis. *Journal of experimental biology* **205,** 2413–2427 (2002).

85. Wang, Z. J. The role of drag in insect hovering. *Journal of experimental biology* **207,** 4147–4155 (2004).

86. Ramamurti, R. & Sandberg, W. C. A computational investigation of the three-dimensional unsteady aerodynamics of Drosophila hovering and maneuvering. *Journal of Experimental Biology* **210,** 881–896 (2007).

87. Gopalakrishnan, P. & Tafti, D. K. A parallel boundary fitted dynamic mesh solver for applications to flapping flight. *Computers & Fluids* **38,** 1592–1607 (2009).

88. Gao, N., Aono, H. & Liu, H. Perturbation analysis of 6-DoF flight dynamics and passive dynamic stability of hovering fruit fly Drosophila melanogaster. *Journal of Theoretical Biology* **270,** 98–111 (2011).

89. Aono, H. & Liu, H. Flapping wing aerodynamics of a numerical biological flyer model in hovering flight. *Computers & Fluids* (2012).

90. Du, G. & Sun, M. Aerodynamic effects of corrugation and deformation in flapping wings of hovering hoverflies. *Journal of Theoretical Biology* **300,** 19–28 (2012).

91. Mou, X. & Sun, M. Dynamic flight stability of a model hoverfly in inclined-stroke-plane hovering. *Journal of Bionic Engineering* **9,** 294–303 (2012).

92. Nakata, T. & Liu, H. A fluid–structure interaction model of insect flight with flexible wings. *Journal of Computational Physics* **231,** 1822–1847 (2012).

93. Xu, N. & Sun, M. Lateral dynamic flight stability of a model bumblebee in hovering and forward flight. *Journal of Theoretical Biology* **319,** 102–115 (2013).

94. Stanford, B. K. & Beran, P. S. Analytical sensitivity analysis of an unsteady vortex-lattice method for flapping-wing optimization. *Journal of Aircraft* **47,** 647–662 (2010).

95. Sarkar, S., Chajjed, S. & Krishnan, A. Study of asymmetric hovering in flapping flight. *European Journal of Mechanics - B/Fluids* **37,** 72–89 (2013).

96. Weis-Fogh, T. Quick estimates of flight fitness in hovering animals, including novel mechanisms for lift production. *Journal of Experimental Biology* **59,** 169–230 (1973).

97. Delaurier, J. D. An aerodynamic model for flapping-wing flight. *Aeronautical Journal of the Royal Aeronautical Society* 125–130 (1993).

98. Weis-Fogh, T. Energetics of hovering flight in hummingbirds and in Drosophila. *Journal of Experimental Biology* **56,** 79–104 (1972).

99. Ellington, C. P. The aerodynamics of hovering insect flight. I. The quasi-steady analysis. *Philosophical Transactions of the Royal Society of London. B, Biological Sciences* **305,** 1–15 (1984).

100. Sane, S. P. & Dickinson, M. H. The aerodynamic effects of wing rotation and a revised quasi-steady model of flapping flight. *Journal of Experimental Biology* **205,** 1087–1096 (2002).

101. Faruque, I. & Humbert, J. S. Dipteran insect flight dynamics. Part 1 Longitudinal motion about hover. *Journal of Theoretical Biology* **264,** 538–552 (2010).

102. Faruque, I. & Humbert, J. S. Dipteran insect flight dynamics. Part 2: Lateral–directional motion about hover. *Journal of Theoretical Biology* **265,** 306–313 (2010).

103. Stanford, B., Kurdi, M., Beran, P. & McClung, A. Shape, structure, and kinematic parameterization of a power-optimal hovering wing. *Journal of Aircraft* **49,** 1687–1699 (2012).

104. Zheng, L., Hedrick, T. & Mittal, R. A multi-fidelity modelling approach for evaluation and optimization of wing stroke aerodynamics in flapping flight. *Journal of Fluid Mechanics* **721,** 118–154 (2013).

105. Mahjoubi, H. & Byl, K. Modeling Synchronous Muscle Function in Insect Flight: a Bio-Inspired Approach to Force Control in Flapping-Wing MAVs. *Journal of Intelligent & Robot Systems* **70,** 181–202 (2012).

106. Fearing, R. S. *et al.* Wing transmission for a micromechanical flying insect. *Robotics and Automation, IEEE International Conference ICRA'00.* **2,** 1509–1516 (2000).

107. Lentink, D., Jongerius, S. R. & Bradshaw, N. L. in *Flying Insects and Robots* (eds. Floreano, D., Zufferey, J.-C., Srinivasan, M. V. & Ellington, C.) 185–205 (Springer Berlin Heidelberg, 2010).

108. P´erez-Arancibia, N. O., Ma, K. Y., Galloway, K. C., Greenberg, J. D. & Wood, R. J. First controlled vertical flight of a biologically inspired microrobot. *Bioinspiration & Biomimetics Journal* **6,** (2011).

109. Whitney, J. P. & Wood, R. J. Conceptual design of flapping-wing micro air vehicles. *Science* **7,** (2012).

110. Norberg, R. A. Hovering flight of the dragonfly Aeschna juncea L., kinematics and aerodynamics. *Swimming and flying in nature* **2,** 763–781 (1975).

111. Van Den Berg, C. & Ellington, C. P. The vortex wake of a hovering model hawk moth. *Philosophical Transactions of the Royal Society B: Biological Sciences* **352,** 317 (1997).

112. Willmott, A. P., Ellington, C. P. & Thomas, A. L. Flow visualization and unsteady aerodynamics in the flight of the hawkmoth, Manduca sexta. *Philosophical Transactions of the Royal Society B: Biological Sciences* **352,** 303–316 (1997).

113. Dickinson, M. H., Lehmann, F.-O. & Sane, S. P. Wing rotation and the aerodynamic basis of insect flight. *Science* **284,** 1954–1960 (1999).

114. Dickinson, M. H., Lehmann, F.-O. & Gotz, K. G. The active control of wing rotation by Drosophila. *Journal of experimental biology* **182,** 173–189 (1993).

115. Lee, J. S., Shin, J. H. & Lee, S. H. Fluid–structure interaction of a flapping flexible plate in quiescent fluid. *Computers & Fluids* **57,** 124–137 (2012).

116. Ramamurti, R. & Sandberg, W. C. A three-dimensional computational study of the aerodynamic mechanisms of insect flight. *Journal of experimental biology* **205,** 1507–1518 (2002).

117. Sun, M. & Tang, J. Unsteady aerodynamic force generation by a model fruit fly wing in flapping motion. *Journal of Experimental Biology* **205,** 55–70 (2002).

118. Mazaheri, K. & Ebrahimi, A. Experimental investigation on aerodynamic performance of a flapping wing vehicle in forward flight. *Journal of Fluids and Structures* **27,** 586–595 (2011).

119. Kim, H. J. & Shim, D. H. A flight control system for aerial robots: algorithms and experiments. *Control Engineering Practice* **11,** 1389–1400 (2003).

120. Jones, K. D., Bradshaw, C. J., Papadopoulos, J. & Platzer, M. F. Bio-inspired design of flapping-wing micro air vehicles. *Aeronautical Journal of the Royal Aeronautical Society* **109,** 385–393 (2005).

121. Croon, G. C. H. E. de, Clercq, K. M. E. de, Ruijsink, R., Remes, B. & Wagter, C. de. Design, aerodynamics, and vision-based control of the DelFly. *International Journal of Micro Air Vehicles* **1,** 71–97 (2009).

122. Ratti, J. & Vachtsevanos, G. A Biologically-inspired micro aerial vehicle sensing, modelling and control Strategies. *Journal of Intelligent & Robotic Systems* **60,** 153–178 (2010).

123. Phan, H. V. *et al.* Stable vertical take-off of an insect-mimicking flapping-wing system without guide implementing inherent pitching stability. *Journal of Bionic Engineering* **9,** 391–401 (2012).

124. Fearing, R. S. & Wood, R. J. in *Flying Insects and Robots* (eds. Floreano, D., Zufferey, J.-C., Srinivasan, M. V. & Ellington, C.) 219–229 (Springer Berlin Heidelberg, 2010).

125. Nabawy, M. R. A. Design of insect-scale flapping wing vehicles. (University of Manchester, 2015).

126. Sun, M. & Du, G. Lift and power requirements of hovering insect flight. *Acta Mechanica Sinica* **19,** 458–469 (2003).

127. Ghommem, M. *et al.* Global optimization of actively morphing flapping wings. *Journal of Fluids and Structures* **33,** 210–228 (2012).

128. Simpson, R. J. S. & Palacios, R. Induced-Drag Calculations in the Unsteady Vortex Lattice Method. *AIAA Journal* (2013).

129. Parslew, B. Simulating avian wing beats and wakes. (University of Manchester, 2012).

130. Smith, M., Wilkin, P. & Williams, M. The advantages of an unsteady panel method in modelling the aerodynamic forces on rigid flapping wings. *Journal of Experimental Biology* **199,** 1073–1083 (1996).

131. Persson, P. O., Willis, D. J. & Peraire, J. Numerical simulation of flapping wings using a panel method and a high-order Navier–Stokes solver. *International Journal for Numerical Methods in Engineering* **89,** 1293–1316 (2012).

132. Leishman, J. G. *Principles of Helicopter Aerodynamics*. (Cambridge University Press, 2006).

133. Katz, J. & Plotkin, A. *Low-speed aerodynamics*. (Cambridge University Press, 2001).

134. Glauert, H. *Aerodynamic Theory: Airplane Propellers*. **5, Div. L,** (1976).

135. Willmott, A. P. & Ellington, C. P. The mechanics of flight in the hawk moth Manduca sexta. II. Aerodynamic consequences of kinematic and morphological variation. *Journal of Experimental Biology* **200,** 2723–2745 (1997).

136. Wakeling, J. M. & Ellington, C. P. Dragonfly Flight III: Lift and power requirements. *The Journal of Experimental Biology* **200,** 583–600 (1997).

137. Truong, Q. T. *et al.* A modified blade element theory for estimation of forces generated by a beetle-mimicking flapping wing system. *Bioinspiration & Biomimetics* **6,** 36008 (2011).

138. Orlowski, C. T. & Girard, A. R. Modeling and simulation of nonlinear dynamics of flapping wing micro air vehicles. *AIAA journal* **49,** 969–981 (2011).

139. Stanford, B., Beran, P., Snyder, R. & Patil, M. Stability and power optimality in time-periodic flapping wing structures. *Journal of Fluids and Structures* **38,** 238–254 (2013).

140. Nabawy, M. R. A. & Crowther, W. J. On the quasi-steady aerodynamics of normal hovering flight part II: model implementation and evaluation. *J. R. Soc. Interface* **11,** 1–9 (2014).

141. Nakata, T., Liu, H. & Bomphrey, R. J. A CFD-informed quasi-steady model of flapping-wing aerodynamics. *Journal of Fluid Mechanics* **783,** 323–343 (2015).

142. Willmott, A. P. & Ellington, C. P. The mechanics of flight in the hawk moth Manduca sexta. I. Kinematics of hovering and forward flight. *The Journal of Experimental Biology* **200,** 2705–2722 (1997).

143. Stepniewski, W. & Keys, C. *Rotary-wing aerodynamics*. (New York, 1984).

144. Sedov, L. I. Two-dimensional problems in hydrodynamics and aerodynamics. *Interscience* 116–118 (1965).

145. Pesavento, U. & Wang, Z. J. Falling Paper: Navier-Stokes solutions, model of fluid Forces, and center of mass elevation. *Physical review letters* **93,** (2004).

146. Andersen, A., Pesavento, U. & Wang, Z. J. Unsteady aerodynamics of fluttering and tumbling plates. *Journal of Fluid Mechanics* **541,** 65–90 (2005).

147. Andersen, A., Pesavento, U. & Wang, Z. J. Analysis of transitions between fluttering, tumbling and steady descent of falling cards. *Journal of Fluid Mechanics* **541,** 91–104 (2005).

148. Usherwood, J. R. & Ellington, C. P. The aerodynamics of revolving wings I. Model hawk moth wings. *Journal of Experimental biology* **205,** 1547–1564 (2002).

149. Dudley, R. & Ellington, C. P. Mechanics of forward flight in bumblebees: I. Kinematics and morphology. *Journal of Experimental Biology* **148,** 19–52 (1990).

150. Milano, M. & Koumoutsakos, P. A clustering genetic algorithm for cylinder drag optimization. *Journal of Computational Physics* **175,** 79–107 (2002).

151. Sane, S. P. The aerodynamics of insect flight. *J Exp Biol* **206,** 4191–4208 (2003).

152. Ben Parslew. Simulating Avian Wingbeats and Wakes. (University of Manchester, 2012).

153. Nabawy, M. R. A. & Crowther, W. J. On the quasi-steady aerodynamics of normal hovering flight part I: the induced power factor. *J. R. Soc. Interface* **11,** (2014).

154. Willmott, A. P. & Ellington, C. P. The mechanics of flight in the hawk moth Manduca sexta. I. Kinematics of hovering and forward flight. *The Journal of Experimental Biology* **200,** 2705–2722 (1997).

155. Liu, H. Integrated modelling of insect flight: From morphology, kinematics to aerodynamics. *Journal of Computational Physics* **228,** 439–459 (2009).

156. in *Fixed and Flapping Wing Aerodynamics for Micro Air Vehicle Applications* 307–339 (American Institute of Aeronautics and Astronautics, 2001).

157. Wang, Z. J. Dissecting insect flight. *Annu. Rev. Fluid Mech.* **37,** 183–210 (2005).

158. Taha, H. E., Hajj, M. R. & Nayfeh, A. H. Flight dynamics and control of flapping-wing MAVs: a review. *Nonlinear Dynamics* **70,** 907–939 (2012).

159. Soueid, H., Guglielmini, L., Airiau, C. & Bottaro, A. Optimization of the motion of a flapping airfoil using sensitivity functions. *Computers & Fluids* **38,** 861–874 (2009).

160. Kaya, M., Tuncer, I. H., Jones, K. D. & Platzer, M. F. Optimization of flapping motion parameters for two airfoils in a biplane configuration. *Journal of Aircraft* **46,** 583–592 (2009).

161. Ghommem, M., Collier, N., Niemi, A. H. & Calo, V. M. On the shape optimization of flapping wings and their performance analysis. *Aerospace Science and Technology* **32,** 274–292 (2014).

162. Isogai, K. & Harino, Y. Optimum aeorelastic design of a flapping wing. *AIAA Journal* **44,** 2040–2048 (2007).

163. Stanford, B., Beran, P. & Patil, M. Optimal flapping-wing vehicle dynamics via Floquet multiplier sensitivities. *Journal of Guidance, Control, and Dynamics* **36,** 454–466 (2013).

164. Powell, M. J. D. *A new algorithm for unconstrained minimization*. (Academic Press, 1970).

165. Svanberg, K. The method of moving asymptotes—a new method for structural optimization. *International Journal for Numerical Methods in Engineering* **24,** 359–373 (1987).

166. Chen, W.-N. *et al.* A novel set-based particle swarm optimization method for discrete optimization problems. *IEEE Transactions on Evolutionary Computation* **14,** 278–300 (2010).

167. Pontani, M. & Conway, B. A. Particle swarm optimization applied to space trajectories. *Journal of Guidance, Control, and Dynamics* **33,** (2010).

168. Brodsky, A. K. Vortex formation in the tethered flight of the peacock butterfly Inachis io L. (Lepidoptera, Nymphalidae) and some aspects of insect flight evolution. *Journal of experimental biology* **161,** 77–95 (1991).

169. Ellington, C. P., van den Berg, C., Willmott, A. P. & Thomas, A. L. R. Leading-edge vortices in insect flight. *Nature* **384,** 626–630 (1996).

170. Nabawy, M. R. A. & Crowther, W. J. A quasi-steady lifting line theory for insect like hovering flight. *PLoS One* **10,** 1–18 (2015).

171. H, N., K, I. & T, H. Measurement of unsteady aerodynamic forces of 3D flapping wing in hovering to forward flight. *26th Congress of International Council of the Aeronautical Sciences and 8th AIAA Aviation Technology, Integration, and Operations (ATIO) Conference* (2008).

172. Phillips, N., Knowles, K. & Bomphrey, R. J. The effect of aspect ratio on the leading-edge vortex over an insect-like flapping wing. *Bioinspir. Biomim.* **10,** 1–18 (2015).

173. Wang, Z. J. Vortex shedding and frequency selection in flapping flight. *Journal of Fluid Mechanics* **410,** 323–341 (2000).

174. Hall, K. C., Pigott, S. A. & Hall, S. R. Power requirements for large-amplitude flapping flight. *AIAA Journal* **35,** 352–361 (1998).

175. Sane, S. P. & Dickinson, M. H. The control of flight force by a flapping wing: lift and drag production. *Journal of experimental biology* **204,** 2607–2626 (2001).

176. Dickinson, M. H., Lehmann, F.-O. & Sane, S. P. Wing rotation and the aerodynamic basis of insect flight. *Science* **284,** 1954–1960 (1999).

177. Dickinson, M. The effects of wing rotation on unsteady aerodynamic performance at low Reynolds numbers. *Journal of experimental biology* **192,** 179–206 (1994).

178. Shyy, W. *et al.* in *Flying Insects and Robots* (eds. Floreano, D., Zufferey, J.-C., Srinivasan, M. V. & Ellington, C.) 143–157 (Springer Berlin Heidelberg, 2010).

179. Wu, J. & Sun, M. The influence of the wake of a flapping wing on the production of aerodynamic forces. *Acta Mech Sinica* **21,** 411–418 (2005).

180. Horstmann, J. T., Henningsson, P., Thomas, A. L. R. & Bomphrey, R. J. Wake development behind paired wings with tip and root trailing vortices: consequences for animal flight force estimates. *PLoS One* **9,** e91040 (2014).

181. Bomphrey, R. J., Taylor, G. K. & Thomas, A. L. R. Smoke visualization of free-flying bumblebees indicates independent leading-edge vortices on each wing pair. *Exp. Fluids* **46,** 811–821 (2009).

182. Bomphrey, R. J., Henningsson, P., Michaelis, D. & Hollis, D. Tomographic particle image velocimetry of desert locust wakes: instantaneous volumes combine to reveal hidden vortex elements and rapid wake deformation. *J. R. Soc. Interface* **9,** 3378–3386 (2012).

183. Alben, S., Shelley, M. & Zhang, J. Drag reduction through self-similar bending of a flexible body. *Nature* **420,** 479–481 (2002).

184. Bushnel, D. M. & Moore, K. J. Drag reduction in nature. *Annual Review of Fluid Mechanics* **23,** 65–79 (1991).

185. Shelley, M. J. & Zhang, J. Flapping and bending bodies interacting with fluid flows. *Annual Review of Fluid Mechanics* **43,** 449–465 (2011).

186. Heathcote, S., Wang, Z. & Gursul, I. Effect of span wise flexibility on flapping wing propulsion. *Journal of Fluids and Structures* **24,** 183–199 (2008).

187. Nakata, T. Aerodynamic performance of flapping flexible wing in insect flight. *Comparative Biochemistry and Physiology Part A: Molecular & Integrative Physiology* **153,** S50–S52 (2009).

188. Pfeiffer, A. T., Lee, J.-S., Han, J.-H. & Baier, H. Ornithopter Flight simulation based on flexible multi-body dynamics. *Journal of Bionic Engineering* **7,** 102–111 (2010).

189. Percin, M., Hu, Y., Oudheusden, B. W. va., Remes, B. & Scarano, F. Wing flexibility effects in clap-and-fling. *International Journal of Micro Air Vehicles* **3,** 217–227 (2011).

190. Walker, W. P. Optimization of harmonically deforming thin airfoils and membrane wings for optimum thrust and efficiency. (Virginia Polytechnic Institute and State University, 2012).

191. Kang, C.-K., Aono, H., Cesnik, C. E. S. & Shyy, W. Effects of flexibility on the aerodynamic performance of flapping wings. *Journal of Fluid Mechanics* **689,** 32–74 (2011).

192. Alexander, D. E. Unusual phase relationships between the forewings and hindwings in flying dragonflies. *Journal of experimental biology* **109,** 379–383 (1984).

193. Osborne, M. F. M. Aerodynamics of flapping flight with application to insects. *Journal of Experimental Biology* **28,** 221–245 (1951).

194. Azuma, A. & Watanabe, T. Flight performance of a dragonfly. *Journal of experimental biology* **137,** 221–252 (1988).

195. Rüppell, G. Kinematic analysis of symmetrical flight manoeuvres of Odonata. *Journal of experimental Biology* **144,** 13–42 (1989).

196. Wakeling, J. M. & Ellington, C. P. Dragonfly Flight II: Velocities, accelerations and kinematics of flapping flight. *The Journal of Experimental Biology* **200,** 557–582 (1997).

197. Park, J. H. & Yoon, K.-J. Designing a biomimetic ornithopter Capable of Sustained and Controlled Flight. *Journal of Bionic Engineering* **5,** 39–47 (2008).

198. Young, J., Walker, S., Bomphrey, R., Taylor, G. & Thomas, A. Details of insect wing design and deformation enhance aerodynamic function and flight efficiency. *Science* **325,** 1549–1552 (2009).

199. Ray, R. P., Nakata, T., Henningsson, P. & Bomphrey, R. J. Enhanced flight performance by genetic manipulation of wing shape in Drosophila. *Nature Communication* **7,** 1–8 (2016).

200. Sun, M. & Du, G. Lift and power requirements of hovering insect flight. *Acta Mechanica Sinica* **19,** 458–469 (2003).

201. Usherwood, J. R. & Ellington, C. P. The aerodynamics of revolving wings II. Propeller force coefficients from mayfly to quail. *Journal of experimental biology* **205,** 1565–1576 (2002).

202. Schlichting, H. & Truckenbrodt, E. *Aerodynamics of the airplane*. (McGraw-Hill, 1979).

203. Hewes, D. *Development of a nonlinear switching function and its application to static lift characteristics of straight wings*. (NACA Technical Memorandum, 1978).

204. Ormiston, R. Induced power of the helicopter rotor. *American Helicopter Society 60th Annual Forum and Technology Display, 8-10 June Baltimore, MD*. 33–53 (2004).

205. Chattot, J. Analysis and design of wings and wing/winglet combinations at low speeds. *Proceedings of the 42nd AIAA Aerospace Sciences Meeting and Exhibit* (2004).

206. Ellington, C. P. The Aerodynamics of hovering insect flight. II. morphological parameters. *Philosophical Transactions of the Royal Society of London. Series B, Biological Sciences* **305,** 17–40 (1984).

207. Sant, T. Improving BEM-based aerodynamic models in wind turbine design codes. (University of Malta and Delft University of Technology, 2007).

208. Gravish, N., Peters, J. M., Combes, S. A. & Wood, R. J. Collective flow enhancement by tandem flapping wings. *Physical review letters* **115,** 1–5 (2015).

209. Filippone, A. *Advanced aircraft flight performance*. (Cambridge University Press, 2012).

210. AIAA. Editorial policy statement on numerical accuracy and experimental uncertainty. *AIAA Journal* **32,** (1994).

211. Roache, P. J., K. Ghia & F. White. Editorial policy statement on the control of numerical accuracy. *ASME Journal of Fluids Engineering* **108,** (1986).

212. Ol, M. V., Bernal, L., Kang, C.-K. & Shyy, W. in *Animal Locomotion* (Springer-Verlag Berlin Heidelberg, 2010).

213. AIAA. *Guide for the verification and validation of computational fluid dynamics simulations*. (1998).

214. Nabawy, M. R. & Crowther, W. J. Aero-optimum hovering kinematics. *Bioinspiration & Biomimetics Journal* **10,** 1–10 (2015).

215. Liu, Y. & Sun, M. Wing kinematics measurement and aerodynamics of hovering droneflies. *Journal of Experimental Biology* **211,** 2014–2025 (2008).

216. Altshuler, D. L., Dickson, W. B., Vance, J. T., Roberts, S. P. & Dickinson, M. H. Short-amplitude high-frequency wing strokes determine the aerodynamics of honeybee flight. *Proceedings of the National Academy of Sciences of the United States of America* **102,** 18213–18218 (2005).

217. Marden, J. H. Bodybuilding dragonflies: costs and benefits of maximizing flight muscle. *Physiological Zoology* **62,** 505–521 (1989).

218. Willmott, A. P. Mechanics of hawk moth flight. (Cambridge University, 2005).

219. Clerc, M. & Kennedy, J. The particle swarm-explosion, stability, and convergence in a multidimensional complex space. *IEEE Trans. on Evolutionary Computation* **6,** 58–73 (2002).

220. Saltelli, A., Chan, K. & Scott, E. M. *Sensitivity analysis*. (Wiley, 2000).

221. Parslew, B. & Crowther, W. J. Simulating avian wing beat kinematics. *Journal of Biomechanics* **43,** 3191–3198 (2010).

222. May, M. L. Dragonfly flight: power requirements at high speed and acceleration. *Journal of Experimental Biology* **158,** 325–342 (1991).

223. Reavis, M. & Luttges, M. W. Aerodynamic forces produced by a dragonfly. in *AIAA, Aerospace Sciences Meeting, 26 th, Reno, NV* 1988 (1988).

224. Ellington, C. Power and efficiency of insect flight muscle. *Journal of Experimental Biology* **115,** 293–304 (1985).

225. Diana, R. G., Jain, P., Centero, M., weinreb, A. & Thiria, B. in *Selected Topics of Computational and Experimental Fluid Mechanics, Environmental Science and Engineering* 147–158 (Springer International Publishing Switzerland, 2015).

226. Hu, Z. & Deng, X.-Y. Aerodynamic interaction between forewing and hindwing of a hovering dragonfly. *Acta Mechanica Sinica* **30,** 787–799 (2014).

227. Seshadri, P., Benedict, M. & Chopra, I. Understanding micro air vehicle flapping-wing aerodynamics using force and flow field measurements. *Journal of Aircraft* (2013).

228. Razak, N. A. & Dimitriadis, G. Experimental study of wings undergoing active root flapping and pitching. *Journal of Fluids and Structures* **49,** 687–704 (2014).

229. Ellington, C. P. The aerodynamics of hovering insect flight. II. morphological parameters. *Phil. Trans. of the Royal Society of London. Series B, Biological Sciences* **305,** 17–40 (1984).

230. Sørensen, J. N. *General Momentum Theory for Horizontal Axis Wind Turbines*. (Springer International Publishing Switzerland, 2015).

231. Johnson, W. *Helicopter Theory*. (Dover Publications inc., New York, 1980).